Investigations in vortex molecule dynamics and ring current generation in Bose-Einstein condensates

A dissertation presented in partial fulfillment of the
requirements for the degree of

Doctor of Philosophy
in
Physics

at
Massey University, Albany
New Zealand

by
Sarthak Choudhury

2022

Abstract

Topological excitations are a special type of long-lived excitation that are impervious to small perturbations in cold atom systems. This thesis aims to investigate properties of two different topological excitations in two-dimensional condensates using the Gross-Pitaevskii equations (GPE).

The majority of this thesis investigates the dynamics of a vortex molecule in coherently coupled Bose-Einstein condensates in different trap geometries. A vortex molecule consists of two vortices in separate condensates bound together by a Josephson vortex (also called a domain wall). We aim to shed light on vortex molecule dynamics using a simple point-vortex framework. Firstly, we extend the point vortex framework to account for the domain wall using a parametrized interaction energy. The interaction energy is parametrized in special boundary conditions that emulate an infinite plane. We then use this extended point vortex model to investigate the phase space and the dynamics of a vortex molecule in a flat-bottomed channel trap. Our extended model captures all the essential features of the phase space and agrees with GPE simulations of a vortex molecule in a trap. We then expand the point vortex framework further to account for the effect of the boundaries on the Josephson vortex by using a distributed vorticity model. We use this continuous vorticity model to investigate the precession frequency of a vortex molecule in an isotropic disc and find support for our model.

Additionally, we investigate a protocol to create persistent supercurrents in a ring shaped single condensate. Though this protocol has been showed to adiabatically create ring currents in ideal one-dimensional rings by Fialko *et.al.* [Phys. Rev. Lett. 108, 250402 (2012)], we use this protocol for two-dimensional rings and find the emergence of ring currents non-adiabatically.

Acknowledgements

A PhD seems to be a pretty long journey but never enough to fully discover all the interesting physics that one comes across. Finishing one in times of a once-in-a-century pandemic of Covid-19 seems particularly short with all the other events which keep on happening. I would like to thank first and foremost my supervisor Joachim Brand who has always helped me with constant support and inspiration. His constant enthusiasm and prodding questions made my PhD enjoyable and productive even during lockdown. It was a pleasure and privilege to work with him on the extremely cool physics of vortices.

Many thanks to my former and current Brand group members Ulrich, Peter, Steven, Jan and Matija who provided many stimulating discussions both about and beyond physics. Special thanks to Chris Bradly for proofreading and giving me feedback about my thesis. I would also like to thank Ashton Bradley for the discussions on vortex motion and the tools in `VortexDistributions.jl` which I have used extensively to track vortices.

Coming to New Zealand was an epic adventure. I would like to thank all the people in CTCP Vesna, Keyvan, Cong, Odile and others for helping me settle in and providing a fun and comfortable working environment. I think friends make life more enjoyable and especially so in a lockdown. To Morten, Ray, Antony and Debac I am indebted for the company, hot pots and board games we enjoyed together. I would like to express my gratitude to all my friends in India, including Ayush, Harsh, Jui, Nilotpal, Ajay, Sudarshan, and others, for their companionship through phone and text.

I am and will always be eternally grateful to my parents. They have always been supportive of whatever I decided to do. Their warmth and kindness have always been a constant throughout my life and helped me to remain sane in these tumultuous times.

I am extremely grateful to my partner Abhishikta. Thank you for the countless hours of constant company that you provided even though we were geographically so far away. Thank you for making my life fun and exciting and always inspiring me to push my boundaries even in my bleak days.

Lastly, I am thankful to Dida who is and will always be a part of my heart. She taught me that true strength always lies in humility and compassion.

Contents

Chapter 1

Introduction

Albert Einstein, inspired by the work of Satyendra Nath Bose on photons [1], first predicted in 1925 the phase transition of non-interacting atoms below a critical temperature to a new state of matter which, we now call Bose-Einstein condensate [2]. This phase transition is a consequence of quantum statistical effects arising from the behavior of a type of particle with integer spin called bosons (named after Bose). Unlike fermions (the other class of fundamental particles which obey a different set of rules), a large number of bosons can condense into the lowest energy state under appropriate conditions.

The discovery of superfluid helium in 1938 [3, 4] renewed interest in atoms at very low temperatures or ultracold atoms. When ^{4}He is cooled below 2.1 K it becomes a superfluid (no viscosity) with remarkable properties like the ability to cross obstacles that lie at a higher level (also called the Onnes effect) and the presence of quantised vortices. This interest would fuel further experimental investigation of ultracold atom systems using more sophisticated methods such as dilution refrigeration [5], Doppler cooling [6] and magneto optical traps [7].

From the first experimental realization of Bose-Einstein condensates (BEC) at JILA [8] in June 1995, the field of ultracold atoms has been extensively used as an ideal testing ground for various phenomena. From creating synthetic gauge fields [9, 10], to quantum mass acquisition [11], to gravitational wave simulation [12], to expanding universe simulations [13], to even vacuum decay in cosmology [14, 15], a host of different phenomena from different branches of physics have been investigated using BECs. Cold atom systems as the name suggests are studied at extremely low temperatures in the order of microkelvins where quantum behavior is enhanced due to the absence of thermal fluctuations. At such small energy scales, the associated parameters can be tuned in experiments to give a high degree of control of the quantum states. This makes BECs an ideal system in which physicists can study extremely exotic and minute quantum phenomenon like bright solitons [16–19], and quantum droplets [20, 21] while controlling the surrounding environment.

One of the more interesting class of excitations in cold atoms are called topological excitations. Topological excitations are excitations which cannot be removed or continuously deformed in an infinite condensate. In mathematical terms they are said to belong to separate homotopy classes. Solutions of a partial differential equation are said to be homotopic if one solution can be continuously deformed into another. BECs show a rich variety of topological excitations which are in different homotopy classes i.e. they cannot be deformed to one another or to the ground state solution. A brief list which is in no way exhaustive contains dark solitons [22], monopoles [23], 2d and 3d skyrmions [24, 25], vortons [26], and knots [27]. The interest in topological excitations mainly lies in the fact that they are very stable against small perturbations and do not decay in time. A more complete review of the theory of topological excitations relevant to physicists can be found in [28].

Among the many topological excitations found in cold atoms we are mainly interested in vortices, domain walls or Josephson vortices and vortex molecules. Vortices in a BEC are similar to those in fluids with the difference being that vortices are quantised i.e. their circulation is always a multiple of $2\pi\hbar/m$ where $\hbar$ is the reduced Planck's constant and m is the mass of the constituent atoms. The first experimental observation of BEC vortices in 1999 was made using two condensates of ^{87}Rb in two different spin states [29]. Using a circularly moving laser which coherently coupled the two condensates, a vortex was created in one condensate using atoms from the other. Hence, the study of coupled condensates has for long intersected with the study of vortices.

Though vortices are only observed in two or more dimensional condensates, even in quasi one-dimensional condensates coherently coupled together, a host of interesting phenomenon are observed [30–33]. One such phenomenon has a close analogy with the Josephson effect. In superconducting electronic systems the Josephson effect is a macroscopic quantum phenomenon. It occurs when two superconducting materials are coupled by a weak non-conducting link [34]. Even though there is a non-conductor in between, the current flows in between the two superconductors and is dependent on the phase difference between the two superconductors. If we now imagine a longer version of this where the junction between the superconductors is extended in one direction Josephson vortices can occur. Conceptually it is a vortex, situated between two superconductors which due to its rotation causes the supercurrent to flow in opposite directions in the adjoining superconductors. This can be emulated in cold atom systems since this system of a long Josephson junction can be directly mapped to a system of two coherently coupled BECs [35].

Things become more interesting when these two phenomenon of vortices and Josephson vortex are combined. In a pair of coherently coupled condensates, vortices in each condensate bound by a Josephson vortex in between together form a vortex molecule. Vortex molecules are interesting because of the similarities to quark confinement in quantum chromodynamics [36]. Quark confinement is a problem where if

we pull apart a quark-antiquark pair, the strong force between them is linearly proportional to the separation. This is exactly the same for vortex molecules with the cost of stretching the Josephson vortex in between linearly dependent on the separation. Moreover, recently Josephson vortices and vortex molecules have been theorized to exist inside neutron stars in deep space [37, 38].

The Schrödinger equation is usually the starting point of studying any non-relativistic quantum phenomenon [39]. But the complexity of this partial differential equation exponentially increases with the number of particles described. Even with the symmetrization property of bosons one needs sophisticated numerical techniques to probe such systems [40]. A simpler approach is to assume that a single order parameter describes the whole condensate. This is especially fitting for Bose-Einstein condensates since the majority of atoms in this state occupy the same ground state energy level. We only take into account the particles which are condensed and in the superfluid state. This leads us to the Gross-Pitaevskii equation(GPE) also known as the non-linear Schrödinger equation. We use the GPE as the main theoretical framework for study in this thesis.

In this thesis we try to understand the behaviour of a vortex molecule in different geometries and try to reduce the complex dynamics into a simple point vortex model. Point vortex models assume that the superfluid is incompressible and greatly simplify the dynamics into ordinary differential equations instead of solving the complex partial differential equations of the GPE. We explore the dynamics of the vortex molecule in a flat-bottomed channel trap and the resulting rotational-pendulum like trajectories. The dynamics of single condensate vortices in a channel have been already studied in [41]. We use this as a starting point for developing a point vortex formalism and then extend it by adding an interaction energy for the contribution of the Josephson vortex on the dynamics of the vortex molecule. We develop a special type of boundary condition called real projective plane boundary condition which emulates an infinite plane for a vortex molecule and use this to parametrize the interaction energy of the vortex molecule as a function of the molecular distance d between the two vortices. The dynamics and in turn the phase space in the channel trap shows different features for zero and non-zero intercomponent interaction between the condensates. Our extended point vortex model captures all the phase space features consisting of saddle points (hyperbolic fixed points), their associated separatrices and elliptical fixed points. Predictions from the point-vortex model are then compared to trajectories predicted by the GPE which show good agreement.

We then develop a point vortex model with extended vorticity and use it to compare with precession frequency of a centered vortex molecule in a flat bottomed disc geometry. Instead of just the contribution of the boundaries on each vortex and the contribution of the Josephson vortex due to stretching, we extend the point vortex model into a point vortex distribution to understand the contribution of the boundaries on the Josephson

vortex as well. This significantly reduces the net contributions of the boundaries on the centered vortex molecule. Equations of motion of this vortex distribution model are developed for a vortex molecule in a flat disc geometry. We then compare the predictions of our model along with earlier models in the literature with GPE simulations for the precession frequency of a centered vortex molecule as a function of d (length of the vortex molecule). We find our distributed vorticity model agrees most with the GPE results.

Lastly, we depart from vortex molecules and discuss a new protocol to create persistent supercurrents in a ring-shaped single condensate. We use a protocol that has been discussed in the context of one-dimensional condensates by nucleating dark solitons. We numerically observe the creation of ring currents by this protocol by the nucleation of a vortex in the outer wall of the ring, which then steadily rotates about the ring while radially getting closer to the center. Near the end of the protocol it enters the inner ring culminating in the creating of ring currents.

The thesis is divided into the following chapters. Chapter 2 gives the relevant background information regarding most of the work done in this thesis. This chapter introduces the familiar form of the GPE and also an alternative hydrodynamic form similar to the Madelung equations. We then give a brief overview on the theory of vortices in condensates and point vortex dynamics. It goes over the Hamiltonian formulation of vortex dynamics and the method of images, which are both widely used in Chapters 3 and 4. We briefly cover some properties of off-center vortices and then touch on Josephson vortices. Vortex molecules are then covered in the light of linearly coupled condensates. A brief review of numerical methods is given at the end.

The main research outputs of this thesis are presented in Chapter 3 and Chapter 4 in the forms of published manuscripts. Additional results are discussed in Chapter 5.

Chapter 3 describes the dynamics of the vortex molecule in a flat-bottomed channel trap. Building upon a point-vortex framework we extend it with an interaction potential and then compare the phase space between our point-vortex model and GPE simulations.

Chapter 4 describes the precession frequency of a vortex molecule in a disc. The extended point vortex model is expanded upon with a new distributed vorticity model, predictions of which, are then compared to GPE simulation data.

Chapter 5 departs from vortex molecules and describes persistent supercurrents in a ring-shaped geometry. We discuss a special protocol to create persistent supercurrents by nucleation of a vortex inside the ring.

Chapter 6 gives the conclusion and further outlook of this thesis.

Published works included in this thesis

Chapters 3-4 are verbatim copies of the published work below except for editorial changes made to match the style of the thesis.

- Sarthak Choudhury and Joachim Brand, "Rotational pendulum dynamics of a vortex molecule in a channel geometry", Phys. Rev. A 106, 043319 (2022).
- Sarthak Choudhury and Joachim Brand, "Distributed vorticity model for vortex molecule dynamics", arXiv:2212.07131 (2022)

Chapter 2

Theoretical background

The Gross-Pitaevskii Equation (GPE) forms the basis of our understanding of vortex molecule dynamics. We use numerical simulations of relevant dynamics of the GPE to compare with our point vortex and charge distributed models. Relevant details of coherently coupled condensates and Josephson vortices and a short review of the corresponding work done in the context of vortex molecules is then provided. We also discuss briefly the numerical techniques used to solve the GPE.

2.1 Gross-Pitaevskii Equation (GPE)

Our main approach to the system of BECs is mean-field in nature i.e. we only take into account the condensed bosons in the superfluid state and express this state by a complex order parameter $\psi(\mathbf{r},t)$ [42, 43]. This simplifies the Schrödinger equation for the many body wavefunction into a much simpler equation for an order parameter which takes the form of a non-linear wave equation. This order parameter describes the behavior of the superfluid as a whole. The GPE is given by

$$i\hbar\frac{d\psi(\mathbf{r},t)}{dt} = \left[-\frac{\hbar^2}{2m}\nabla^2 + V(\mathbf{r})\right]\psi(\mathbf{r},t) + g\left|\psi(\mathbf{r},t)\right|^2\psi(\mathbf{r},t), \tag{2.1}$$

where $V(\mathbf{r})$ is an external potential in which the BEC has been confined. This term is used to introduce channel or disc boundaries to the BEC in Chapter 3 and Chapter 4 respectively. We assume only particle-particle s-wave interactions which gives rise to the non-linear term $g = 4\pi\hbar^2 a/m$ where a is the scattering length. Moreover, we also work in the dilute gas limit with the gas parameter given by $na^3 \ll 1$, where $n = |\psi(\mathbf{r},t)|^2$ is the density of the condensate. The chemical potential μ acts as a control for the number of particles in numerical simulations and m is the mass of the individual bosons. A rigorous derivation of the Gross-Pitaevskii equation for the ground state of a Bose-gas with repulsive interactions ($g > 0$) is given by [44].

We can obtain time independent stationary solutions by assuming that $\psi(\mathbf{r},t) =$

$\Psi(\mathbf{r})e^{-\frac{i\mu t}{\hbar}}$ and place it in Eq. (2.1) obtaining

$$\mu\Psi(\mathbf{r}) = \left[-\frac{\hbar^2}{2m}\nabla^2 + V(\mathbf{r})\right]\Psi(\mathbf{r}) + g\left|\Psi(\mathbf{r})\right|^2\Psi(\mathbf{r}) \ . \tag{2.2}$$

A trivial homogenous solution of this equation where $V(\mathbf{r}) = 0$, is given by $|\Psi(\mathbf{r})| = \sqrt{n} = \sqrt{\mu/g}$ where n is the density. The healing length of the GPE is defined as

$$\xi = \frac{\hbar}{\sqrt{mgn}} = \frac{\hbar}{\sqrt{m\mu}}. \tag{2.3}$$

The healing length defines the length scale in which the order parameter 'heals' back to the homogenous solution away from forced local inhomogeneties. This is essentially the length scale in which the order parameter recovers from any disturbances due to the boundaries, centers of vortices or solitons. Any changes in length scales smaller than the healing length cannot be observed in the density n of the order parameter. For brevity, we drop the explicit dependence of the order parameter on position and time and write $\psi(\mathbf{r}, t)$ as ψ henceforth. The energy functional for the GPE is defined as

$$W = \int\left[\frac{\hbar^2}{2m}\left|\nabla\psi\right|^2 + V(x)\left|\psi\right|^2 - \mu\left|\psi\right|^2 + \frac{g}{2}\left|\psi\right|^4\right]d\mathbf{r}. \tag{2.4}$$

W is used throughout this thesis as a measure of the energy of the different systems. One can get back the GPE in Eq. (2.1) from the energy functional via the relation $i\hbar\partial\psi/\partial t = \delta W[\psi, \psi^\star]/\delta\psi^\star$.

2.1.1 Continuity Equation and Velocity of the Condensate

The continuity equations are one of the most fundamental classes of equations that describe the transport of conserved quantities. The continuity equation in our present context can be described in terms of the velocity of the condensate and its sources and sinks. This is essentially the start of our discussion on velocities of the superfluid and vortices. If we multiply Eq. (2.1) with $\psi^\star$ and subtract the complex conjugate we get the familiar form of the continuity equation,

$$\frac{\partial n}{\partial t} + \nabla\cdot\boldsymbol{j} = 0, \tag{2.5}$$

where $n = |\psi|^2$ is the particle-number density and $\boldsymbol{j} = -\frac{i\hbar}{2m}(\psi^\star\nabla\psi - \psi\nabla\psi^\star)$ is associated with the current density.

In order to define the velocity of the condensate we write the complex order function in terms of two real valued functions (also known as the Madelung ansatz), the phase S,

and the density n as,

$$\psi = \sqrt{n}e^{iS}. \tag{2.6}$$

The phase S is similar to the velocity potential in hydrodynamics. This can be seen by inserting the ansatz in Eq. (2.6) into Eq. (2.5) which gives us

$$\mathbf{j} = n\frac{\hbar}{m}\nabla S. \tag{2.7}$$

We define the velocity of the condensate as

$$\mathbf{v_s} = \frac{\hbar}{m}\nabla S. \tag{2.8}$$

such that $\mathbf{j} = n\mathbf{v}$, akin to the current density in electromagnetism. This gives us an expression for the velocity of the condensate flow which we use to initiate our brief foray into vortices and their properties.

To finish this subsection for completeness, we insert our ansatz in Eq. (2.6) into Eq. (2.1) to find

$$\hbar\frac{\partial}{\partial t}S + \left(\frac{1}{2}m{\mathbf{v_s}}^2 + V + gn - \frac{\hbar^2}{2m\sqrt{n}}\nabla^2\sqrt{n}\right) = 0, \tag{2.9}$$

which is the corresponding time-dependent equation for the phase. This is similar to Euler's equation in hydrodynamics for a potential flow of non-viscous gas except for the term containing the gradient of the density, also called the "quantum pressure" term, which is a direct consequence of the Heisenberg uncertainty principle. The quantum analog of Euler's equation along with the continuity equation in Eq.(2.5) are a set of coupled equations equivalent to the GPE in Eq.(2.1).

2.2 Vortices

Vortices have been the subject of study in superfluid systems especially in liquid helium for a long time [29, 45–51]. It would be unrealistic to cover all aspects of vortices in condensates in this thesis not only because it would be a substantial list but also since there are still aspects of vortices which are not completely understood, like vortex mass [52–55]. Hence, we restrict ourselves to those properties of vortices relevant to our eventual discussion of vortex molecules and their dynamics. We start this section by defining the circulation of a vortex and the velocity of the condensate in the presence of a vortex. We then define excitation energy and the Hamiltonian formulation of vortex dynamics and the point vortex model which are used extensively in Chapters 3 and 4. This also gives us an ideal platform to talk about off-center vortices which are a component of vortex molecules in a disk which will be discussed later in Chapter 4.

Continuing our analogy with hydrodynamics, the vorticity of the condensate is defined as $\boldsymbol{\omega} = \nabla \times \mathbf{v}_s$. If we calculate the vorticity of $\mathbf{v_s}$ from Eq. (2.8), we get zero (the curl of a gradient is always zero). The velocity ($\mathbf{v_s}$) of the condensate turns out to be distinctly irrotational. The concept of vortices in a condensate has already run into major problems. Nature solves this with a singularity in the phase at the center (also called the vortex core) of the vortex. The order parameter needs to be single-valued at all places and hence, the phase difference around the contour has to be a multiple of 2π.

Circulation of the vortex is given by

$$\Gamma = \oint_{\partial A} \mathbf{v_s} \cdot d\boldsymbol{l} = \frac{\hbar}{m} \oint_{\partial A} (\nabla S \cdot d\boldsymbol{l}) = 2\pi\kappa \frac{\hbar}{m}, \tag{2.10}$$

where κ is an integer representing the winding number of the singularity, also called the "charge" of the vortex and ∂A is a closed loop in space enclosing the vortex. The value of κ is taken to be ± 1 unless otherwise stated. The circulation of a vortex in a condensate is quantised in units of $2\pi\frac{\hbar}{m}$.

In the context of the GPE the phase field for a vortex at the origin, in an infinite two-dimensional plane is single valued, rotationally symmetric and given by

$$S_v(x, y) = \kappa\theta, \tag{2.11}$$

where θ is angular coordinate in the polar coordinate system. In the Cartesian system for a vortex in an arbitrary position $\mathbf{R_0} = (X, Y)^t$, the phase can be expressed as $S_v = \arctan[(y - Y)/(x - X)]$. The density at the vortex core goes to zero and hence the order parameter itself is not singular avoiding any pathological behavior. Inserting this phase function into Eq. (2.8) we get the velocity field of the condensate due to a vortex in an infinite two-dimensional plane

$$\mathbf{v}(\mathbf{r}) = \frac{\hbar\kappa}{m} \nabla S_v = \frac{\hbar\kappa}{m} \frac{\hat{z} \times (\mathbf{r} - \mathbf{R}_0)}{|\mathbf{r} - \mathbf{R}_0|^2}, \tag{2.12}$$

where, $\hat{z}$ is the unit vector in the z direction transverse to the plane.

A vortex state is an excited state. The excitation energy is defined as

$$E_v = W_{\text{vortex}} - W_{\text{homogeneous}} \tag{2.13}$$

where W_{vortex} is the energy functional in Eq.(2.4) due to the vortex solution and $W_{\text{homogeneous}}$ is the energy functional of the homogenous solution with the same chemical potential μ. The interaction potential of the vortex as a function of molecular length d is also described similarly in Chapter 3. The energy of a centered vortex in a disk-shaped

geometry with radius R similar to the one used in Chapter 4 using Eq.(2.13) is [42]

$$E_v = \pi n \frac{\hbar^2}{m} \ln\left(1.464 \frac{R}{\xi}\right). \tag{2.14}$$

The energy of the vortex turns out to be dependent on the trap size. This essentially means that the energy of the vortex in an infinite plane is logarithmically divergent.

If we now rotate the container of the condensate with a rotational frequency Ω then, vortices can be shown to be energetically stable beyond a critical frequency. According to classical mechanics [56] the energy E_v' of a rotating frame in terms of the energy E_v of the non-rotating frame is

$$E_v' = E_v - \mathbf{L} \cdot \mathbf{\Omega}, \tag{2.15}$$

where $\mathbf{L}$ is the angular-momentum vector and $\mathbf{\Omega}$ is the angular velocity vector describing the rotation of the container or trap. A state will be energetically favorable to the ground state if Ω exceeds a critical value Ω_c which depends on the character of the excited state and especially the geometry of the container [46, 57, 58]. The order parameter for the centered vortex is an eigenstate of the angular momentum operator and the angular momentum which is conserved is given by $\mathbf{L} = (0, 0, N\hbar)^t$ where N is the total number of particles in the condensate with each particle carrying one unit of angular momentum.

2.2.1 Point Vortex model and the method of images

The reader might have noticed that though we have specified that the density n at the center of a vortex goes to zero, we have not explicitly gone over the actual solution. The solution is obtained by inserting the phase in Eq. (2.11) and our ansatz in Eq (2.6) into the GPE (2.1) and then solving for n. The variational approximation in [50], $\sqrt{n(x)} = \sqrt{n_0}x/\sqrt{x^2+2}$ provides a good fit to the numerical solution of the GPE, where $x = r/\xi$, ξ is the healing length and n_0 is the background density for the homogenous solution without a vortex.

The point-vortex assumption essentially ignores the density profile of the vortex and assumes them to be point singularities in the phase. This assumption is justified if all other length scales are much larger than ξ the healing length which is the case in most of the remaining thesis. Within the point-vortex framework we can use the tools already developed in hydrodynamics to deal with vortex dynamics [59, 60].

Hamiltonian Formulation

In this section we go through the basic ideas of vortices in an irrotational fluid. We assume that the condensate is incompressible meaning $\nabla \cdot \mathbf{v_s} = 0$. The vorticity as defined before is $\boldsymbol{\omega} = \nabla \times \mathbf{v_s}$. In this section we define the vector potential $\boldsymbol{\mathcal{H}}$ where, $\nabla \times \boldsymbol{\mathcal{H}} = \mathbf{v}_s$.

Taking the curl on both sides and rearranging we get

$$\nabla^2 \boldsymbol{\mathcal{H}} = -\boldsymbol{\omega}. \tag{2.16}$$

The vector potential satisfies a Poisson's equation with vorticity on the right side. Using standard techniques [61] one can write the solution in terms of the Greens's function for the Laplacian,

$$\boldsymbol{\mathcal{H}}(\mathbf{r}) = \int G(\mathbf{r}-\mathbf{z})\boldsymbol{\omega}(\mathbf{z})d\mathbf{z}. \tag{2.17}$$

We now focus on the two-dimensional case and assume the vorticity to be zero everywhere except at the origin, where it has a singularity, or in other words $\omega(\mathbf{z}) = \kappa\delta(\mathbf{z})$, where $\delta(\mathbf{z})$ is the well-known Dirac-delta function and $\omega(\mathbf{z})$ is the z component of the vorticity and points out of the plane. The Green's function in this case for two dimensions comes out as

$$G(\mathbf{r}) = -\frac{1}{2\pi}\ln|\mathbf{r}|, \tag{2.18}$$

with

$$\nabla^2 G(\mathbf{r}) + \delta(\mathbf{r}) = 0. \tag{2.19}$$

An additional feature of two-dimensional flows is that the vector-potential is essentially a scalar in the sense that even though a vector it only has non-zero components in the axes orthogonal to both the dimensions i.e. $\boldsymbol{\mathcal{H}} = (0, 0, \mathcal{H})^t$.
Hence,

$$\mathbf{v}_s = \nabla \times \boldsymbol{\mathcal{H}} = (\partial_y \mathcal{H}, -\partial_x \mathcal{H}, 0) \equiv \nabla^{\perp}\mathcal{H}. \tag{2.20}$$

These equations for the velocity of a condensate in the presence of vortices can be rewritten as

$$\dot{X} = \frac{\partial \mathcal{H}}{\partial Y}, \tag{2.21a}$$

$$\dot{Y} = -\frac{\partial \mathcal{H}}{\partial X}\ . \tag{2.21b}$$

These take the form of Hamilton's equations [62] and hence the vector potential plays the role of a time-dependent Hamiltonian in the flow of two-dimensional fluids. In the terminology of hydrodynamics $\mathcal{H}$ is called a Kirchoff-Routh function and Eqs. (2.21) are called Kirchoff equations [63, 64].

We use Eq. (2.21) to derive the equations of the vortex field of N vortices in a two-dimensional plane. The vorticity in such a case is $\omega(\mathbf{z}) = \sum_{\alpha=1}^{N} \kappa_\alpha \delta(\mathbf{z} - \mathbf{R}_\alpha)$, where $\mathbf{R}_\alpha =$

$(X_\alpha, Y_\alpha)^t$ is the position of the αth vortex and κ_α is its respective charge. Hence,

$$\begin{aligned}\mathcal{H}_\alpha(\mathbf{r}) &= -\frac{1}{2\pi}\int \kappa_\alpha \ln|\mathbf{r}-\mathbf{z}|\delta(\mathbf{z}-\mathbf{R}_\alpha)d\mathbf{z} \\ &= -\frac{\kappa_\alpha}{2\pi}\ln|\mathbf{r}-\mathbf{R}_\alpha|. \end{aligned} \tag{2.22}$$

The velocity field of N vortices is a linear superposition of all such fields and hence, $\mathbf{v}_N = \sum_\alpha^N \nabla^\perp \mathcal{H}_\alpha$. The velocity of each point vortex is the local velocity of the fluid which is not affected by the velocity field of the vortex itself. If we take the special case of two point vortices at positions $\mathbf{R}_\beta = (X_\beta, Y_\beta)^t$ and $\mathbf{R}_\gamma = (X_\gamma, Y_\gamma)^t$, the velocity of vortex at point β following Eq. (2.21) is given by

$$\dot{X}_\beta = \frac{1}{2\pi}\kappa_\beta \frac{X_\beta - X_\gamma}{|\mathbf{R}_\beta - \mathbf{R}_\gamma|^2}, \tag{2.23a}$$

$$\dot{Y}_\beta = -\frac{1}{2\pi}\kappa_\beta \frac{Y_\beta - Y_\gamma}{|\mathbf{R}_\beta - \mathbf{R}_\gamma|^2}. \tag{2.23b}$$

We transition from this unitless hydrodynamic system to a system of equations with physical significance in Chapter 3 to derive the extended point vortex model and compare with our vorticity model in Chapter 4. In the limit of vortex cores being away from the boundaries at length scales larger than the healing length ξ and with vortex velocities much smaller than the speed of sound one can assume the superfluid to be nearly incompressible. In this incompressible limit we can use point vortex motion to describe the dynamics of quantum vortices [65, 66]. To describe the dynamics of point-vortices, the Kirchoff-Routh function is given by a rescaled $\mathcal{H}(X,Y) = E_{\mathrm{SV}}(X,Y)/2\pi n\hbar\kappa$ where E_{SV} is the energy of a vortex at position $R = (X,Y)^t$, ignoring the compressible corrections and a constant offset.

Method of Images

Another consequence of the condensate being irrotational is that the phase S of the vortex follows Laplace's equation

$$\nabla^2 S_v = 0. \tag{2.24}$$

This is similar to the electrical potential in a volume with a given electrostatic charge distribution. Just as in electrostatics [67] we can also predict the velocity field for a known vortex distribution using the method of images. The method of images is primarily a mathematical tool which emulates the effect of the boundaries on the dynamics of vortices. Instead of solving the original problem with boundaries one solves a problem with vortices and corresponding virtual "image" vortices with opposite charge, with the conditions that no superfluid flows "across" the boundaries i.e. there is no component of the velocity field perpendicular to the boundaries. In the last section we showed that the vortex velocity

field is a superposition of the different velocity fields of the individual vortices. One uses this to create an image vortex in a position such that the resulting superimposed velocity field is not perpendicular to the boundaries. Using this method, vortex dynamics can be accurately predicted at distances much larger than the healing length from the boundaries, in condensates without any large density modulations (i.e. $\nabla n \approx 0$ except near the vortices or boundaries) [68–70]. Since this method is only valid for point vortices in incompressible fluids, predictions of the velocity field from the method of images usually diverge at the boundaries which is not the case for the physical system. The velocity of an off-center vortex at position $\mathbf{R} = (X, Y)^t$ in a disc shaped geometry centered at the origin with radius L where $R < L$ can be estimated using the method of images. For a disc shaped geometry, the position of the image vortex is given by $\tilde{\mathbf{R}} = L^2\mathbf{R}/|\mathbf{R}|^2$ [67].

Following Eq. (2.23) velocity of the vortex due to the image vortex in polar coordinates comes out as

$$\begin{aligned}\mathbf{v}(\mathbf{R}) &= -\frac{\hbar\kappa}{m}\frac{\hat{z}\times(\mathbf{R}-\tilde{\mathbf{R}})}{|\mathbf{R}-\tilde{\mathbf{R}}|^2} \\ &= -\frac{\hbar\kappa}{m}\frac{R}{L^2-R^2}\hat{\theta}(t),\end{aligned} \tag{2.25}$$

where $\hat{\theta}(t)$ is the time-dependent unit vector perpendicular to $\mathbf{R}$ and $R = |\mathbf{R}|$. The velocity vector is always perpendicular to the radial direction and therefore, the vortex moves in a circle around the disc. The velocity increases as R increases and diverges at the boundaries, which is an artifact of the method of images as discussed before.

The method of images only works in problems where the boundaries of the condensate have some symmetry which can be exploited to make the problem easier to solve. This is the case for the hard wall channel (symmetric in one dimension) that we consider in Chapter 3 and the disc (rotationally symmetric) in Chapter 4.

Off-centered vortex

We further discuss precession frequency in the case of off-centered vortices since this directly ties into our discussion of vortex molecules. An off-center vortex in a rotationally symmetric trap precesses in a circle around the center as discussed before in Eq. (2.25). For an off-center vortex one can use the method of images to estimate the extra kinetic energy due to the velocity field. The excitation energy [43] up to leading order logarithmic dependence of R/ξ is

$$E_v = \frac{mn\kappa^2}{4\pi}[\ln(L/\xi) + \ln(1 - R^2/L^2)], \tag{2.26}$$

where the vortex is at position $\mathbf{R}$ inside a circular disc of radius L and $R = |\mathbf{R}|$. It is also straightforward to find the angular momentum of an off-center vortex [42]

$$L_z = \pi L^2 n\hbar \left(1 - \frac{R^2}{L^2}\right), \tag{2.27}$$

where L_z is the z-component of the angular momentum $\mathbf{L}$.

Now, Eq.(2.15) can be used to describe the energy of an off-center vortex in the lab frame from the rest frame of the vortex i.e. a frame rotating with the same frequency as the vortex. Differentiating Eq. (2.15) we get $\Omega = \partial E/\partial L$. The precession frequency of an off-centered vortex is

$$\Omega = \frac{\partial E}{\partial L} = \frac{\partial E/\partial R}{\partial L/\partial R} = \frac{\hbar\kappa}{m}\frac{1}{L^2 - R^2}. \tag{2.28}$$

This matches the prediction of the precession frequency from the velocity in Eq.(2.25) using $\Omega = |\mathbf{v}|/R$. The angular momentum approach using Eq. (2.28) does not need complete information about the whole velocity field. It is more useful to characterize other rotating excited states with more complicated velocity fields. We use this later to define the precession frequency of a vortex molecule for a coupled condensate system.

2.3 Coupled Condensate System

For the majority of this thesis, we will mainly be interested in coupled BEC condensates. The mean field description of a coupled condensate follows Eq. (2.1) involving two complex order parameters ψ_1 and ψ_2:

$$i\hbar\frac{d\psi_1}{dt} = \left[-\frac{\hbar^2}{2m}\nabla^2 + V(\mathbf{r}) - \mu + g_1\left|\psi_1\right|^2 + g_{12}\left|\psi_2\right|^2\right]\psi_1 - \nu\psi_2, \tag{2.29a}$$

$$i\hbar\frac{d\psi_2}{dt} = \left[-\frac{\hbar^2}{2m}\nabla^2 + V(\mathbf{r}) - \mu + g_2\left|\psi_2\right|^2 + g_{12}\left|\psi_1\right|^2\right]\psi_2 - \nu\psi_1, \tag{2.29b}$$

where, $V(\mathbf{r})$ is the external potential and m is the mass of the bosons as before. We have assumed that masses of individual atoms of both condensates are the same. ν is the spatially invariant coherent (Rabi) coupling which can be realized by an electromagnetic field or by driving a two-photon microwave transition continuously [71]. The s-wave non-linear intra-component interaction potentials for the two condensates are g_1 and g_2 and g_{12} is the intercomponent interaction potential.

Experimentally, this can be realized by having a BEC of ultra-cold atoms restricted to two hyperfine states e.g. in ^{23}Na where $g_{12} \approx 0.9g_1 \approx 0.9g_2$ as in [72, 73]. This is also the ratio of g, g_{12} we have taken in our numerics. Another way would be to have a single condensate separated by a barrier potential [35]. The tunneling frequency would act as ν with the two order parameters being realized in the two wells even though homogeneity

needs to be ensured in the two directions and this only describes a system with $g_{12} = 0$.

For simplicity, we are mainly interested in the miscible regime i.e. $g + |\nu|/n_0 > g_{12}$ [74]. This is the regime in which the condensates are not phase separated and form a homogenous mixture. Throughout this thesis we also assume $g_1 = g_2$. The unbalanced case where $g_1 > g_2$ or vice versa is also a regime with rich vortex physics [75–78], but that also introduces additional buoyancy effects, which is beyond the scope of this work.

The corresponding energy functional analogous to Eq (2.4) is

$$W = \int \Bigg\{ \sum_{i=1}^{2} \left[\frac{\hbar^2}{2m} |\nabla \psi_i|^2 + V(x) |\psi_i|^2 + \frac{g_i}{2} |\psi_i|^4 - \mu |\psi_i|^2 \right] + g_{12} |\psi_1|^2 |\psi_2|^2 - \nu(\psi_1 \psi_2^* - \psi_1^* \psi_2) \Bigg\} d\mathbf{r}. \tag{2.30}$$

In the simplest case of Eq. (2.29), we can replace the kinetic energy term by a constant which physically corresponds to two one dimensional condensates in a double well trap with tunneling between them. This form of Eqs. (2.29) can be mapped to that of a pendulum [79–81]. Similar to a pendulum, such a system shows small amplitude oscillations in the density (also called Josephson oscillations) and unstable oscillations around its highest point (also called macroscopic self trapping).

It is interesting to note that the two condensates have two $U(1)$ symmetries separately when coupling (ν) is zero. Changing the phase of the order parameter by an arbitrary factor does not change the solution. This symmetry corresponds to the number conservation of the particles of each individual species i.e. $\int d\mathbf{r} \, |\psi_1|^2 = N_1$ and $\int d\mathbf{r} \, |\psi_2|^2 = N_2$. This is no longer the case when $\nu \neq 0$. The conservation of particles in each condensate is broken since particles can be interchanged between the two species. Only the total number of atoms $\int d\mathbf{r}(|\psi_1|^2 + |\psi_1|^2) = N$ is conserved corresponding to only one $U(1)$ symmetry. Hence, the system does not change even if we change the phases but keep the relative phase constant.

2.4 Josephson Vortex

Vortices have been studied in superconductivity especially in the context of Josephson junctions for some time [82–85]. The Ginzburg-Landau theory [86] states that the superconducting state can be characterized by a complex order parameter that is similar to the complex order parameter of the GPE. The Josephson vortex is a special type of quantum vortex, also called a domain wall in [87], that sits in the non-conducting barrier between two long superconductors shown in Fig. 2.1. The relevant system can be described by a partial differential equation called the sine-Gordon equation [34]. If Φ is the phase difference between the two superconductors then the equation of motion

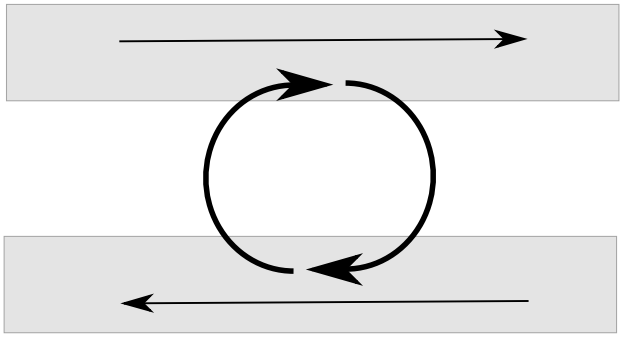

Figure 2.1: The grey boxes represent long superconducting Josephson junctions while the black arrows give the direction of supercurrent in a Josephson vortex. The center of the vortex lies in between the two long Josephson junctions.

governing the flow of supercurrents is

$$\frac{\partial^2\Phi}{\partial x^2} - \frac{\partial^2\Phi}{\partial t^2} = \sin\Phi. \tag{2.31}$$

The Josephson vortex solution is a stable stationary wave solution of this equation, which can be written as

$$\Phi = 4\arctan\left(e^{\pm x}\right), \tag{2.32}$$

corresponding to a rotation in Φ by 2π (-2π) described as a fluxon (antifluxon).

It was shown by [88] that the system of two coupled BECs in one dimension can also be described by the sine-Gordon equation in the limit of small ν and large non-linearity. These solutions can be directly mapped to the dispersion relations of Josephson vortex solutions of the sine-Gordon equation in Eq. (2.31) within a parameter regime.

Kaurov and Kuklov in [89, 90] found analytic solutions to the system of equations (2.29) without a trap, in an infinite medium and considering only one spatial dimension. Solutions of the system in an infinite medium corresponding to Josephson vortices are marked by $\psi_1 = \psi, \psi_2 = \psi^*$ and the relative phase between the two condensates is an integer multiple of 2π. The solutions are:

$$\psi_{1,2} = \sqrt{1+\frac{\nu}{\mu}}\tanh\left(2\sqrt{\frac{\nu m}{\hbar}}x\right) \pm i\frac{\sqrt{1-3\frac{\nu}{\mu}}}{\cosh(2\sqrt{\frac{\nu m}{\hbar}}x)}. \tag{2.33}$$

As seen in Eq. (2.33) this solution of Josephson vortices is only valid if $\nu/\mu < 1/3$. If coherent coupling increases beyond this then the solution converts into another type of topological excitation called a dark soliton as shown by [88]. Dark solitons are localized density dips which propagate at constant speed without being deformed. They have been extensively studied in cold atom physics and were primarily discovered as a feature of single-component BECs [22, 91–93].

The relative phase change by 2π is vital in recognizing the presence of a Josephson vortex. This relative phase signature of a Josephson vortex in coupled condensates can be seen in the vortex molecule from numerical calculations. They are compared with the relative phase change of the Josephson vortex solution of the sine-Gordon equation in Chapter 3.

2.5 Vortex Molecule

A vortex molecule consists of two vortices in separate condensates with a domain wall or Josephson vortex in between. This excitation is a solution of the two-dimensional analogue of Eq. (2.29). One can even couple three condensates together to create trimers [94] or more exotic excitations similar to Baals *et.al.* [95], but we restrict our discussion to only two components.

As discussed in Section 2.2 the energy of an excited state with non-zero angular momentum can be made lower than the ground state by moving to a rotating frame of reference. Essentially, the trap itself is made to rotate so that the system favors solutions with non-zero angular momenta. In our system of equations in Eqs. (2.29) this corresponds to adding an extra term $\Omega\hat{L}_z\psi_{1/2}$ to both equations to move to a rotating frame of reference. Here Ω is the frequency of rotation and $\hat{L}_z$ is the angular momentum operator which introduces a rotation of the container in the z axis perpendicular to the plane of the condensate. In such a rotating system, the ground state vortex molecular length (d) changes by changing Ω. Vortex molecules with larger (or smaller) lengths rotate clockwise (or anticlockwise) in real time evolution.

Vortices in either condensate are termed as fractional quantised vortices due to their circulation being fractional in units of $2\pi\hbar/m$ [96–101]. Let us assume we have a coherently coupled quasi 1d condensates and we have a vortex in only one condensate i.e. $\psi_1 = \sqrt{n_1}e^{iS_v}$ and $\psi_2 = \sqrt{n_2}$. If we calculate the mass circulation following Eq. (2.10) we get

$$\Gamma = \oint_A \frac{|\psi_1|^2 \mathbf{v}_1 + |\psi_2|^2 \mathbf{v}_2}{|\psi_1|^2 + |\psi_2|^2} \cdot d\boldsymbol{l} = \frac{\hbar}{m}\oint_A \frac{|\psi_1|^2 \nabla S_v}{|\psi_1|^2 + |\psi_2|^2} \cdot d\boldsymbol{l} = 2\pi\frac{\hbar}{m}\frac{n_1}{n}, \tag{2.34}$$

where, n is the total density i.e. $n = n_1+n_2$. The term $\frac{n_1}{n}$ 'makes' individual vortices in two coupled condensates fractional vortices. This essentially illustrates that in the presence of linear coupling ($\nu > 0$) individual vortices in each condensate in a two condensate system can no longer create a stationary state [102]. Either the vortex needs to be connected to another vortex in the other condensate via a domain wall creating a vortex molecule. Or the vortex line terminates in another anti-vortex in the same condensate creating a vortex-antivortex pair. Calculating the mass circulation of a vortex molecule we get, $\Gamma_{\mathrm{M}} = 2\pi\frac{\hbar}{m}$ i.e. again an integer circulation.

Kasamatsu *et al.* [103] first showed numerically that in a coherently coupled system, two vortices form a topologically stable vortex molecule bound together by a domain wall in the relative phase. Moreover, for finite rotation frequency, the non-axisymmetric

molecule is always lower in energy than the axisymmetric one, similar to single condensate vortices [104]. As the rotation frequency increases the distance between the vortices, which we call the mean molecular distance d, also decreases.

We end this section briefly mentioning vortex molecule lattices. The study of lattices consisting of vortices in condensates mainly stems from Abrikosov lattice structures (unit cell being a triangle) in superconducting systems [105, 106]. Vortex molecules form off-center Abrikosov lattices for vortices in each condensate. To minimize the intercomponent interactions (g_{12}) the triangular cells of vortices in each condensate are offset such that the vortex in one condensate is at the center of the triangular cell of the other. If the intercomponent interaction is increased then this triangular lattice structure becomes a shifted square lattice [96, 107–109]. Increasing the linear coupling ν beyond a critical value the positions of the vortices in the two condensates coincide creating a lattice with the unit cell returning to triangular in shape [110].

2.5.1 Numerical methods

To solve Eq. (2.29) we use a 5th order Runge-Kutta method based on the improved algorithm in [111] found in the software library `DifferentialEquations.jl`. Vortex trajectory detection was performed using methods from `VortexDistributions.jl`. We have used a 7 point stencil to resolve the Laplacian in Eq. (2.29). All simulations were taken with $n_g > 2$ where n_g is the number of grid points per healing length ξ.

We use imaginary time evolution to get the lowest energy state of a system. This method does not conserve particle number and therefore, we have a term containing μ in Eq. 2.29 which conserves the particle number with $\int(|\psi_1|^2+|\psi_2|^2)d\mathbf{r} = N$. Imaginary time evolution is done by substituting t by $\tau = -it$, in Eq. (2.29). This has been used primarily to calculate the energy of the domain wall as a function of molecular distance d (the length of the domain wall given by the distance between the vortices in each condensate) in Chapter 3 and also to fix initial starting positions of the vortex molecule. Imaginary time evolution can be thought of as a gradient-descent optimization of the GPE energy functional. It converges the system to its lowest energy solution. As mentioned in Section 2.2, vortices are excited states, so imaginary time evolution ultimately converges to a state with no vortex left in the condensate. Hence, narrow Gaussian pinning potentials are used to keep the vortices in place during imaginary time evolution and then removed during time evolution. Removal of the pins results in negligible noise which does not change any results. Vortex molecules are seeded with two vortices pinned at a finite length d. Imaginary time evolution is done for an optimal number of time steps for the system to converge to a vortex molecule. Although this is not the global energy minimum, imaginary time evolution will converge to a local energy minima corresponding to the positions of the vortices.

Chapter 3

Rotational pendulum dynamics of a vortex molecule in a channel geometry

3.1 Introduction

Nonlinear topological excitations like vortices have been the topic of study in many fields ranging from high-energy to condensed-matter physics [112, 113]. They are long lived and stable due to protection by topological constraints and can only be destroyed by annihilation with opposite charges, or by moving out of the superfluid domain. Intriguing examples of topological excitations are vortex molecules [103, 114], which exist in two-component superfluids with linear coupling.

Recent experimental progress has made it possible to study two-dimensional two-component Bose-Einstein condensates (BECs) with homogeneous linear (Rabi) coupling between the two components [33, 72, 115], thus creating an extended linearly-coupled two-component superfluid. The linear coupling tends to align the phases of the two condensates. As such, a vortex filament piercing only one of the two condensates initiates a domain wall of the relative phase [87], which can terminate at an antivortex in the same condensate, or at a vortex in the other one. The latter situation is referred to as a vortex molecule [103], or sometimes a fractional vortex molecule [116], since either of the two individual vortices only carries a fraction of the total vortex charge. Vortex molecules have been studied extensively in the theoretical literature [103, 109, 114, 117–119]. Interest in vortex molecules is partly motivated by the fact that the domain wall creates an energy cost that is approximately linear with the separation of the two vortices, which evokes analogies to color confinement in quantum chromodynamics [36, 116].

Predicting and understanding vortex dynamics is a challenging problem. A ubiquitous situation in ultracold gas experiments is the elongated or cigar-shaped geometry [42, 120, 121], where a vortex perpendicular to the long trap axis is a stable nonlinear excitation

in a scalar superfluid [122]. In such an elongated trap, a single vortex becomes a localised excitation on the length scale of the narrow trap diameter resembling a dark soliton, which gives rise to the concept of a solitonic vortex [123–129].

In this work we analyse the motion of a vortex molecule in a channel, or slab geometry that is extended in one dimension and has parallel hard-wall boundaries in the second. We assume the third dimension to be tightly confined to the order of the healing length or smaller, such that the problem effectively becomes two-dimensional. This channel geometry embodies the essential qualitative features of the ubiquitous elongated atom trap, while at the same time providing access to analytical treatment. Furthermore, near homogeneous potentials with hard walls, so-called flat bottom traps, have become increasingly available to experiments in recent years [130, 131].

The dynamics of a single vortex in a channel was analysed in Ref. [129] starting from the method of images and applying compressible corrections as a perturbation. For a vortex molecule, the presence of the domain wall connecting the vortices provides an interaction potential, which has an interesting interplay with the effects of the channel boundaries on the vortex motion. Here, we develop a simple model for the dynamics of a vortex molecule augmenting the method of images by a parameterised interaction potential capturing the effects of the domain wall. Similar ideas have previously been implemented to understand the rotation dynamics of a centered vortex molecule in an isotropic harmonic trap [117, 119]. For the channel geometry the model predicts a rich phase space for the vortex molecule dynamics with different dynamical regimes separated by separatices. A particularly intriguing rotational-pendulum-like regime of motion is predicted in the case of repulsive cross-condensate nonlinear interactions where the vortex-vortex interaction has a minimum at finite vortex separation. Numerical simulations with the Gross-Pitaevskii equation (GPE) complement and support the predictions of the simplified model.

The chapter is structured as follows. Section 3.2 introduces the system in light of the GPE. Section 3.3 introduces the main point-vortex model and its equations of motion. Section 3.4 discusses the resulting dynamics of the vortex molecule comparing predictions from the point vortex model with full time-dependent simulations of the GPE dynamics, with conclusions provided in Sec. 3.5. Appendix 3.6 provides details on the calculation and the parametrization of the vortex molecule energy and the twisted projective plane boundary conditions used in the calculations.

3.2 Mean-Field Formulation

We describe a system of two linearly coupled Bose-Einstein condensates with complex order parameters $\psi_1(\mathbf{r}, t)$ and $\psi_2(\mathbf{r}, t)$ in two spatial dimensions described by the coupled

GPEs

$$i\hbar\frac{d\psi_1}{dt} = \left(\hat{h} - \mu + g_1|\psi_1|^2 + g_{12}|\psi_2|^2\right)\psi_1 - \nu\psi_2, \tag{3.1a}$$

$$i\hbar\frac{d\psi_2}{dt} = \left(\hat{h} - \mu + g_2|\psi_2|^2 + g_{12}|\psi_1|^2\right)\psi_2 - \nu\psi_1, \tag{3.1b}$$

where $\hat{h} = -\frac{\hbar^2}{2m}\nabla^2 + V_{\text{ext}}$ is the single-particle Hamiltonian for bosons of mass m, $V_{\text{ext}}(\mathbf{r})$ is an external potential experienced by both components, and $\mathbf{r} = (x, y)^t$ denotes the vector of spatial coordinates. In the following, we assume the external potential to provide hardwall boundaries and otherwise be flat, such that we do not have to carry the external potential explicitly. The chemical potential μ is used to control the particle number in numerical simulations. The coupling constants g_1 and g_2 describe the intra-component nonlinear interactions, and g_{12} the intercomponent nonlinearity. The physics of Eq. (3.1) can be experimentally realized by a BEC of ultracold atoms restricted to two hyperfine states, e.g. ^{23}Na as in Ref. [72] where $g_{12} \approx 0.9g_1 \approx 0.9g_2$. A spatially homogeneous coherent (Rabi) coupling between the hyperfine states with the energy scale ν can be provided by driving a radio-frequency or a two-photon microwave transition continuously. Using different atomic species, such as ^{41}K may make it possible to tune the cross-component coupling constant g_{12} with a Feshbach resonance [14]. Alternatively, the physics of Eq. (3.1) with $g_{12} = 0$ could also be accessed by using a single-component BEC and double-well potential in z direction where barrier tunneling provides the linear coupling ν and the component order parameters $\psi_{1/2}(\mathbf{r})$ are realised in the different wells [35]. Ensuring homogeneity in two spatial dimensions will be more difficult with such a setup, however. To avoid phase separation, we assume $g_{12}^2 < g_1 g_2$. For simplicity, we choose $g \equiv g_1 = g_2 > 0$ and $\nu > 0$ [132]. The unbalanced case i.e. $g_1 \neq g_2$ offers additional effects like relative buoyancy between the components and scale separation for the healing length of each component, which have been discussed in the literature [29, 75–78].

The free energy associated with the GPE (3.1) is given by

$$W = \int \Bigg[\sum_{i=1}^{2} \left(\psi_i^* \hat{h} \psi_i + \frac{g_i}{2}|\psi_i|^4 - \mu|\psi_i|^2 \right) + g_{12}|\psi_1|^2|\psi_2|^2 - \nu(\psi_1^*\psi_2 + \psi_1\psi_2^*) \Bigg] d\mathbf{r}. \tag{3.2}$$

Numerically we find low energy solutions by propagating Eq. (3.1) in imaginary time, i.e. replacing $t \to -i\tau$, which corresponds to minimizing the free energy W by gradient flow.

A trivial or ground state solution of Eq. (3.1) (for $V_{\text{ext}} = 0$) is found with constant $\psi_1 = \psi_2$, where the densities of the individual component condensates are homogeneous and identical, with $|\psi_i|^2 = n_0 \equiv (\mu + \nu)/(g + g_{12})$ for $i = 1, 2$. The healing length $\xi =$

$\hbar/\sqrt{m(\mu+\nu)}$ provides the length scale on which this homogeneous solution is recovered away from forced local inhomogeneities due to solitons, vortices, or boundary conditions.

Vortex molecules are composed of a vortex in each component connected by a domain wall of the relative phase. Relevant analytically known solution of Eq. (3.1) with nonlinear defects are the simple vortex and the Josephson vortex.

3.2.1 Simple vortex

The simple vortex solution is one where a vortex penetrates both components at the same place. It can be understood of a special case of a vortex molecule where the two vortices occur at the same location. To find the solution we assume $\psi_1(\mathbf{r}) = \psi_2(\mathbf{r})$, which simplifies Eq. (3.1) to the single-component GPE

$$i\hbar\frac{d\psi_1}{dt} = \left(\hat{h} - \mu_{\text{eff}} + g_{\text{eff}}|\psi_1|^2\right)\psi_1, \tag{3.3}$$

with $\mu_{\text{eff}} = \mu + \nu$ and $g_{\text{eff}} = g_1 + g_{12}$, the vortex solutions of which are well known on an infinite domain [133]. They are characterised by a singular phase distribution, an integer vortex charge κ, and a density node at the vortex location. Specifically for a vortex located at the origin of the coordinate system,

$$\psi_1(\mathbf{r}) = \psi_2(\mathbf{r}) = \sqrt{n_0} f_\kappa(r/\xi) e^{i\kappa\phi}, \tag{3.4}$$

where (r, ϕ) are the polar coordinates, and f_κ is a dimensionless function with $f_\kappa(0) = 0$ (for $\kappa \neq 0$) and $f_\kappa(\infty) = 1$ [133]. Due to phase gradients that decay only weakly away from the vortex singularity, the excitation energy of the simple vortex solution diverges logarithmically with the integration domain.

3.2.2 Josephson vortex

The Josephson vortex is a stationary solution of the coupled GPEs (3.1) that realises a domain wall of the relative phase. The solution exists for $\nu < \mu/3$ and is homogeneous in one dimension (say along the y coordinate) and inhomogeneous in the other [89, 90]

$$\psi_{1/2}(\mathbf{r}) = \sqrt{n_0}\left[\tanh\left(\frac{x}{\xi_{\text{J}}}\right) \pm i\sqrt{\frac{\mu-3\nu}{\mu+\nu}}\,\text{sech}\left(\frac{x}{\xi_{\text{J}}}\right)\right], \tag{3.5}$$

where $\xi_{\text{J}} = \hbar/\sqrt{4m\nu}$ is the Josephson vortex length scale. The stationary Josephson vortex is connected to a single-parameter family of moving solitary-wave solutions, which were characterized in Ref. [88]. The whole family of solutions is dynamically stable in one spatial dimension (corresponding to tight confinement in the y dimension) For $\nu \lessapprox 0.15\mu$ the stationary Josephson vortex is a local minimum of the dispersion relation. This means that it has a positive effective mass [88] and thus is dynamically stable also in two

dimensions [134–136]. For $0.15\mu \lessapprox \nu < \mu/3$ the Josephson vortex has negative effective mass and suffers the snaking instability with eventual decay into vortices similar to the instability of dark solitons [124, 137]. At $\nu \to \mu/3$ the Josephson vortex solution reaches a bifurcation point where it becomes identical to a dark soliton [88, 89].

The energy (line) density of the Josephson vortex is

$$\sigma_{\mathrm{J}} = \frac{W_{\mathrm{JV}} - W_{\mathrm{hom}}}{L} = \frac{8\hbar\sqrt{\nu}}{3\sqrt{m}} \frac{3\mu - \nu}{g + g_{12}}, \tag{3.6}$$

where W_{JV} and W_{hom} are the free energies of the Josephson vortex and the homogeneous solution, respectively, and L is the extent of the integration domain in the y direction. Approximate descriptions of a domain wall of the relative phase as a soliton solution of the sine-Gordon equation are sometimes used [87, 89]. These reproduce the properties of the Josephson vortex solutions of the GPE, including the energy, to leading order in $\sqrt{\nu/\mu}$, i.e. when the linear coupling is a small parameter [88].

3.2.3 Vortex molecule

In this work we are interested in the dynamics of a vortex molecule in a channel geometry. Thus we consider a channel of width D aligned along the x-axis with hard wall boundaries at $|y| \geq D/2$. We further use a finite computational domain with $x \in (-D, D]$ with antiperiodic boundary conditions, i.e. adding a π phase to each of $\psi_{1/2}$, as appropriate for a single vortex.

In order to obtain a vortex molecule numerically, we imprint the known phase profile of a vortex in a channel for a single incompressible superfluid [129] with different vortex positions in each component and then evolve to a low-energy configuration using imaginary-time evolution. Imaginary time evolution quickly removes most excitations but is slow to move vortex singularities. While local minima of the free energy W are obtained by evolving in imaginary time until convergence, evolution for a finite amount of imaginary time will yield near ideal field configurations corresponding to the lowest energy for the given position of the vortex singularities. Vortex positions are located by accurately tracking the positions of the phase singularities using the software library `VortexDistributions.jl` [138].

Figure 3.1 shows a vortex molecule in a channel with width $D = 100\xi$. The vortices located in component 1 and 2 show up in the relative phase $\phi_r = \arg(\psi_1\psi_2^*)$ as vortex and antivortex, respectively, see Fig. 3.1 (a). In the single-component density shown in panel (b) the depleted vortex core appears black while the vortex in the other component leads to a local density maximum due to the repulsive cross-component nonlinearity and thus appears as a bright spot. Panel (c) shows a three-dimensional schematic indicating how a vortex filament can be understood to thread the arrangement. If the linear coupling between the two components originates from a double-well trap, the components will be displaced in the z dimension as shown. If, on the other hand, Rabi coupling of internal

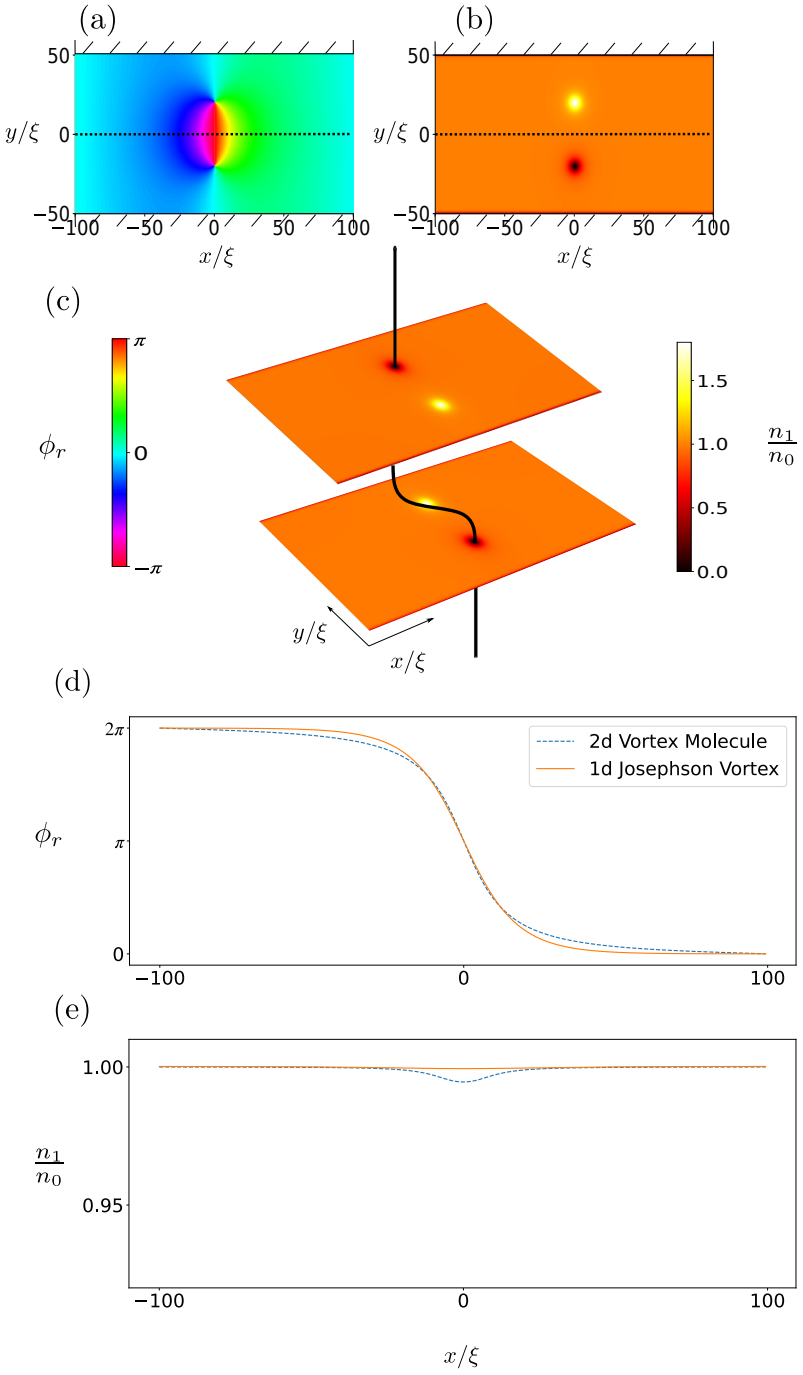

Figure 3.1: Vortex molecule in a channel geometry of width $D = 100\xi$ with hard-wall boundaries at $y = \pm D/2$. (a) Relative phase $\phi_r(\mathbf{r}) = \arg(\psi_1\psi_2^*)$ showing the domain wall oriented along the y axis with a large phase gradient. The singular termination points indicate the locations of vortices in the component condensates. (b) Single component density $n_1(\mathbf{r}) = |\psi_1|^2$ with a density depletion and local density maximum at the locations of the vortices in components 1 and 2, respectively. (c) Concept diagram showing how a vortex filament can be understood to thread the two-component condensate. The density of component 1 is shown on the lower plane and that of component 2 is shown on the upper plane. (d) Relative phase from panel (a) along the $y = 0$ line [dotted line in panel (a)], shown as the dashed blue line in comparison to the relative phase $\arg(\psi_1\psi_2^*)$ from the analytic Josephson vortex solution of Eq. (3.5) (full red line). (e) Density of component 1 from panel (b) along the $y = 0$ line [dotted line in panel (b)], shown as the dashed blue line in comparison to the component density $|\psi_1|^2$ from the analytic Josephson vortex solution of Eq. (3.5) (full red line). Parameters are $\nu = 2 \times 10^{-4}\mu$, $g_{12} = 0.9g$, and $g = 0.53\mu\xi^2$.

states is used, the separation is merely conceptual. Since the vortex line cannot simply terminate, it must thread between the component, which gives rise to the domain wall of the relative phase. The domain wall structure is clearly seen in the relative phase in Fig. 3.1 (a). More detailed views are shown in panels (d) and (e), which compare the cross sections of the relative phase and single-component density from panels (a) and (b), respectively, with the exact Josephson vortex solution of Eq. (3.5). While small differences exist, it is seen that the Josephson vortex solution provides a reasonable description of the domain wall in the vortex molecule.

The domain wall has an energy content, which may be expected to be linear in its length d and approximated by $\sigma_J d$, according to Eq. (3.6). If the domain wall is stretched beyond a critical length, it becomes energetically favourable to generate vortex-antivortex pairs and break up the domain wall into shorter segments [136]. Within the picture of Fig. 3.1 (c) this can be understood as the vortex filament looping outside of the condensates (or the in-between region), where its existence comes without an energy cost.

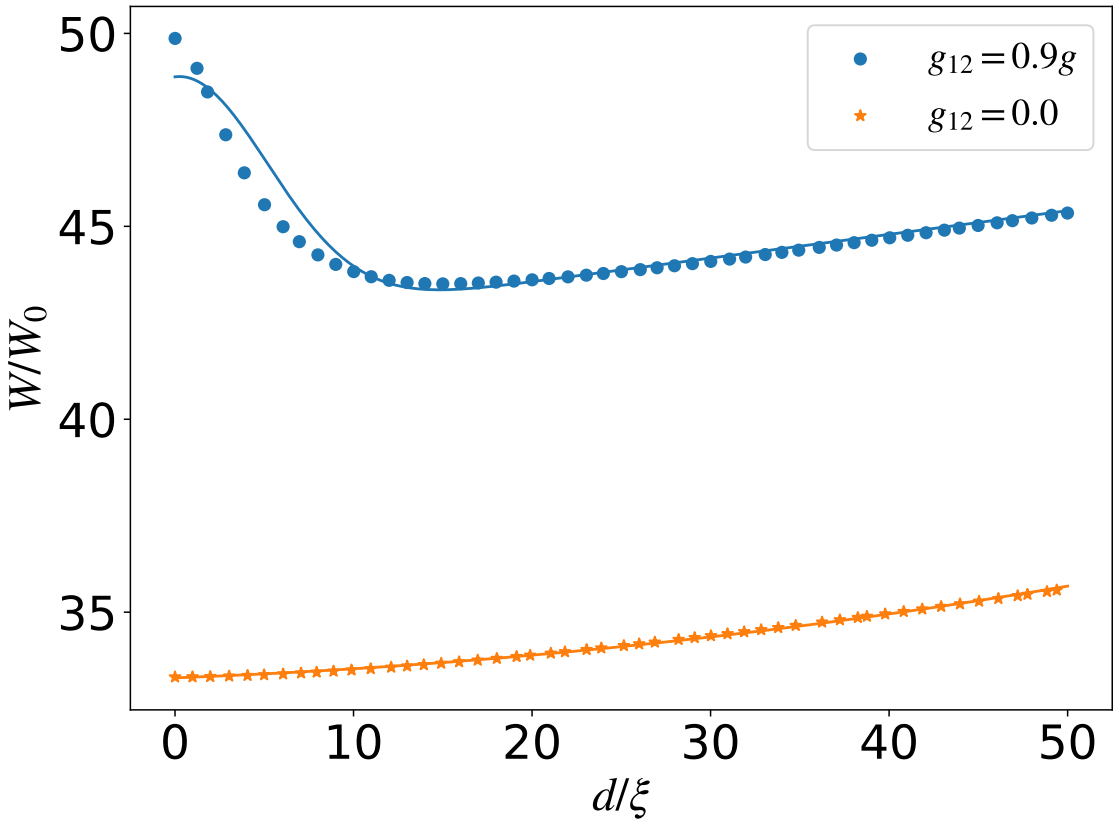

Figure 3.2: Total energy of the vortex molecule as a function of the molecular distance d on a square domain of $180\xi \times 180\xi$. The symbols are numerical results from imaginary time evolution and the lines are fits to the numerical data. In the absence of cross-component interactions, the vortex molecule energy is monotonous with a minimum at $d = 0$, while for repulsive cross-component interactions at $g_{12} = 0.9g$ and energy minimum appears at the equilibrium distance $d_{\rm eq} = 14.8\xi$. Other parameters are $\nu = 2 \times 10^{-4}\mu$, $g = 0.53\mu\xi^2$ for $g_{12} = 0.9g$, and $g = \mu\xi^2$ for $g = 0$. The unit of energy is $W_0 = \hbar^2(\mu + \nu)/m(g_1 + g_c)$. Details of the fitting procedure and boundary conditions are described in Appendix 3.6.

In order to better understand and quantify the energy cost of the domain wall, i.e. the interaction energy of a vortex molecule, we compute the total energy as a function of the molecular size d, the distance between the two constituent vortices as shown in Fig. 3.2. The computational details and the boundary conditions, which are designed to approximate the vortex molecule on an infinite plane, are described in Appendix 3.6. Results for two different values of the intercomponent nonlinear coupling g_{12} are shown, and neither is strictly linear, indicating that other effects come into play in addition to the linear domain wall contribution. Moreover, the slope is consistently less than the Josephson vortex energy density $\sigma_{\rm J}$ consistent with a finding of Ref. [36]. For $g_{12} = 0$ the energy is monotonous as a function of d, and the lowest energy configuration is at $d = 0$, i.e. when the vortex molecule realises the simple vortex solution of Eq. (3.4). When $g_{12} > 0$ the repulsive intercomponent nonlinearity favors filling the vortex core in one component with density from the other, which leads to an

energy benefit when the vortex cores do not overlap. In this case the energy has an energy minimum at a finite molecular distance, which becomes a stable equilibrium of the vortex molecule in real-time evolution.

3.3 Extended Point-vortex Model

The potentially complicated dynamics of a condensate described by the GPE, a partial differential equation, can be simplified considerably by reducing it to the motion of point vortices. This is justified when no or little other excitations such as solitons or phonon radiation are present or generated, i.e. when the motion proceeds by moving near adiabatically through low-energy vortex configurations. In this case the motion can be described in a Hamiltonian framework just from knowing the energy (gradients) of the different vortex configurations [60]. In the case of a near-homogeneous BEC with hard-wall boundary conditions this is greatly aided by the method of images. The method of images is exact for an incompressible and irrotational fluid, and becomes a useful approximation for the GPE on length scales large compared to the healing length. Here we combine the numerically determined interaction energy of a vortex molecule with the method of images for capturing the influence of the channel boundaries on the vortex motion.

3.3.1 Single component vortex in a channel

Reference [129] solved the vortex in a channel in a single-component BEC starting from the method of images and developing compressible corrections as a power series in $(\xi/D)^2$. We summarise some of the results and use them as a starting point. Ignoring the compressible corrections and a constant offset, the energy of a single vortex in a channel extended along the x direction with walls located at $y = \pm D/2$ is

$$E_{\mathrm{SV}}(Y) = \frac{\pi\hbar^2\kappa^2 n}{m} \ln\cos\left(\frac{Y}{D}\pi\right), \tag{3.7}$$

where n is the (background) density and Y is the y-displacement of the vortex from the origin (with $-D/2 < Y < D/2$). The velocity field (phase gradient) of the vortex solution is exponentially localised in the x dimension on the length scale D. The momentum in x direction is simply proportional to Y,

$$P_{\mathrm{SV}} = 2\pi n\hbar\kappa Y, \tag{3.8}$$

which is consistent with the phase space for vortex motion being two-dimensional.

Following Ref. [60], it is convenient to introduce a rescaled Hamiltonian function

$$\mathcal{H}(X,Y) = \frac{E(X,Y)}{2\pi n\hbar\kappa}, \tag{3.9}$$

where $E(X,Y)$ is the energy of a vortex with coordinates X and Y. With this definition, the y coordinate of a vortex becomes the canonical momentum of its x coordinate, and Hamilton's equations take the form

$$\dot{X} = \frac{\partial \mathcal{H}}{\partial Y}, \tag{3.10a}$$

$$\dot{Y} = -\frac{\partial \mathcal{H}}{\partial X}. \tag{3.10b}$$

For the single vortex in the channel, we find [with $E(X,Y) = E_{\mathrm{SV}}(Y)$]

$$\dot{X} = -\frac{\pi\kappa\hbar}{2mD}\tan\left(\frac{Y}{D}\pi\right), \tag{3.11a}$$

$$\dot{Y} = 0. \tag{3.11b}$$

A single vortex thus propagates at constant velocity along the channel, i.e. in the x direction. The velocity depends on the (constant) Y position in the channel. It vanishes when the vortex is situated in the center of the channel (at $Y = 0$) and diverges as the vortex molecule approaches the edges of the channel. Note that this divergence is regularized and disappears for a compressible BEC as the predictions from the point vortex model become invalid when the vortex separation from the boundaries is less than the healing length ξ. The effective mass is given by [129]

$$\begin{aligned} M_{\mathrm{SV}} = \frac{dP_{\mathrm{SV}}}{d\dot{X}} &= \left(\frac{\partial^2\mathcal{H}}{\partial P_{\mathrm{SV}}^2}\right)^{-1} = \frac{(2\pi n\hbar\kappa)^2}{E''_{\mathrm{SV}}(Y)} \\ &= -\frac{4}{\pi}mnD^2\left[\cos\left(\frac{Y}{D}\pi\right)\right]^2. \end{aligned} \tag{3.12}$$

It is negative and its magnitude is approximately the mass of the superfluid enclosed by the area D^2 while the vortex is near the center of the channel.

3.3.2 Vortex molecule point vortex model

For the Hamiltonian of the vortex molecule we use a simple ansatz where we simply add the energies of each vortex in the channel and an interaction energy

$$\mathcal{H}_{\mathrm{VM}}(X_1,X_2,Y_1,Y_2) = \frac{E_{\mathrm{SV}}(Y_1) + E_{\mathrm{SV}}(Y_2) + V(d)}{2\pi n\hbar\kappa}, \tag{3.13}$$

where $V(d)$ is an interaction energy that depends only on the distance $d = \sqrt{(X_1-X_2)^2 + (Y_1-Y_2)^2}$ between the two vortices. The equations of motion then

become

$$\dot{X}_{1/2} = \frac{\partial \mathcal{H}_{\mathrm{VM}}}{\partial Y_{1/2}}, \tag{3.14a}$$

$$\dot{Y}_{1/2} = -\frac{\partial \mathcal{H}_{\mathrm{VM}}}{\partial X_{1/2}}. \tag{3.14b}$$

The phase space of the vortex molecule is four dimensional and more complex than that of a single vortex in a channel. While the motion of the center of mass does not fully decouple from the relative motion, it still does so approximately when the center of mass is close to the center of the channel. In particular, when the molecule is symmetrically centered in the channel with $Y_1 = -Y_2$ then it follows from Eqs. (3.14) and (3.13) and the fact that $E_{\mathrm{SV}}(Y)$ of Eq. (3.7) is an even function of Y, that $\dot{X}_1 + \dot{X}_2 = 0 = \dot{Y}_1 + \dot{Y}_2$. I.e. the center of mass is stationary and the phase space of the vortex molecule motion reduces to the two-dimensional phase space of relative motion.

3.3.3 Approximate separation of the center-of-mass motion

In order to obtain more insights we introduce a symmetric transformation to new canonical coordinates for center-of-mass $(\tilde{Q}, \tilde{P})$ and relative motion $(\tilde{q}, \tilde{p})$

$$\tilde{q} = \frac{X_1 - X_2}{\sqrt{2}}, \qquad \tilde{Q} = \frac{X_1 + X_2}{\sqrt{2}}, \tag{3.15a}$$

$$\tilde{p} = \frac{Y_1 - Y_2}{\sqrt{2}}, \qquad \tilde{P} = \frac{Y_1 + Y_2}{\sqrt{2}}. \tag{3.15b}$$

The Hamiltonian function in the new coordinates is

$$\tilde{\mathcal{H}}(\tilde{q}, \tilde{Q}, \tilde{p}, \tilde{P}) = \mathcal{H}_{\mathrm{VM}}\left(\frac{\tilde{Q} + \tilde{q}}{\sqrt{2}}, \frac{\tilde{Q} - \tilde{q}}{\sqrt{2}}, \frac{\tilde{P} + \tilde{p}}{\sqrt{2}}, \frac{\tilde{P} - \tilde{p}}{\sqrt{2}}\right), \tag{3.16}$$

with $\mathcal{H}_{\mathrm{VM}}$ given by Eq. (3.13). By expansion of the relevant terms in powers of $\tilde{P}$ and $\tilde{p}$ we find that the Hamiltonian can be written in the approximately separable form

$$\tilde{\mathcal{H}}(\tilde{q}, \tilde{Q}, \tilde{p}, \tilde{P}) = \tilde{\mathcal{H}}_{\mathrm{com}}(\tilde{Q}, \tilde{P}) + \tilde{\mathcal{H}}_{\mathrm{rel}}(\tilde{q}, \tilde{p}) + \mathcal{O}(\tilde{P}^2 \tilde{p}^2), \tag{3.17}$$

which confirms that relative motion can be considered independently at or close to a fixed point of the center-of-mass motion with $\tilde{P} = 0$, consistent with the result from the previous section. Conversely, center-of-mass motion can be considered independently at a fixed point of the relative motion with $\tilde{p} = 0$. The center-of-mass motion described by

$$\tilde{\mathcal{H}}_{\mathrm{com}}(\tilde{Q}, \tilde{P}) = \frac{E_{\mathrm{SV}}(\tilde{P}/\sqrt{2})}{\pi n \hbar \kappa}, \tag{3.18}$$

which is, up to rescaling factors, that of a single-component vortex in a channel. Displacement from center in the y direction thus induces a constant velocity in x direction according to Eq. (3.11). The center-of-mass effective mass in physical units is

$$\begin{aligned} M_{\mathrm{VM}} &= 4\pi n\hbar\kappa \left(\frac{\partial^2 \tilde{\mathcal{H}}_{\mathrm{com}}}{\partial \tilde{P}^2} \right)^{-1} \\ &= 2M_{\mathrm{SV}}(\tilde{P}/\sqrt{2}), \end{aligned} \tag{3.19}$$

which is twice the mass of a single vortex in this approximation, and $\tilde{P}/\sqrt{2} = (Y_1 + Y_2)/2$ is the y position of the vortex molecule's center. The relative motion is described by

$$\tilde{\mathcal{H}}_{\mathrm{rel}}(\tilde{q}, \tilde{p}) = \frac{2E_{\mathrm{SV}}(\tilde{p}/\sqrt{2}) + V(\sqrt{2}\sqrt{\tilde{q}^2 + \tilde{p}^2})}{2\pi n\hbar\kappa}, \tag{3.20}$$

which captures both the effects of the channel boundary conditions via E_{SV} and the molecular interaction via the vortex molecule energy V.

3.4 Vortex molecule dynamics with fixed center of mass

The extended point vortex model of the previous section presents a simple model of vortex motion in a Hamiltonian framework. It greatly reduces the complexity associated with the partial differential equations of the GPE description. Our goal is to show that it can capture the major qualitative features of vortex molecule dynamics appropriate to a given trap geometry with a parameterized vortex interaction.

We consider the dynamics of a vortex molecule in a channel of width D in y direction and infinite extent in x direction. To emulate the infinite channel in our numerical GPE simulations, we use a computational domain of $2D \times D$ extent with hard wall boundaries in y and antiperiodic boundary conditions (periodic with a π phase twist) in x direction, which realizes a ribbon with a periodic vortex – anti-vortex train. Due to the exponential localization of the solitonic vortex (Sec. 3.3.1 and Ref. [129]), the phase gradients become negligible near the x boundaries, and the single vortex in an infinite channel is well emulated.

In the extended point vortex model, where energy is conserved, the trajectories of a vortex molecule are the contour lines of the Hamiltonian $\mathcal{H}_{\mathrm{VM}}$ in the four-dimensional phase space. For the interaction energy $V(d)$, we use a parameterized fit of the total energy of a vortex obtained from imaginary-time evolution in real projective plane boundary conditions, which mimic a vortex molecule on an infinite plane. For details see Appendix 3.6 and Fig. 3.2. In the following we consider the situation where the vortex molecule is aligned symmetrically in the channel and hence its center of mass remains stationary (see Sec. 3.3.2). In this case the dynamics of the vortex molecule is fully captured by the

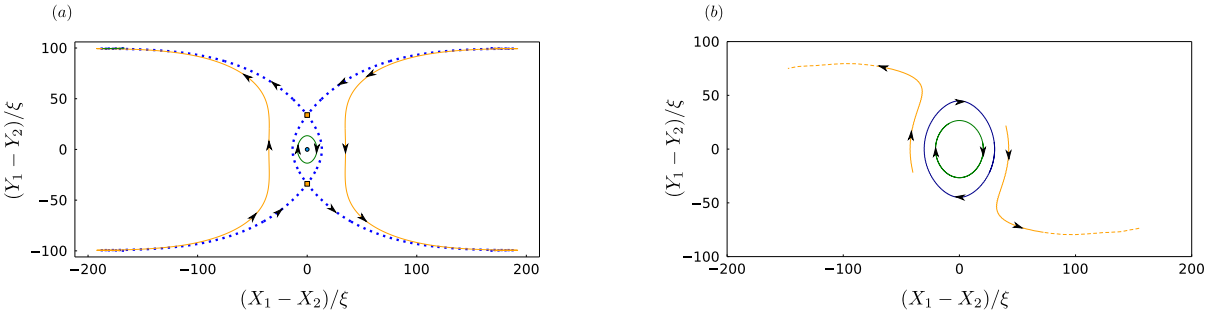

Figure 3.3: Phase space of relative motion for the vortex molecule in a channel of width $D = 100\xi$ in the absence of intercomponent nonlinearity ($g_{12} = 0$). Trajectories are shown as lines with arrows in the relative coordinates of the vortices $X_1 - X_2 = \sqrt{2}\tilde{q}$ and $Y_1 - Y_2 = \sqrt{2}\tilde{p}$ with a hard-wall boundary at $Y_1 - Y_2 = \pm D$. (a) Extended point vortex model of Eqs. (3.13) and (3.14). Symbols indicate fixed points. The round blue dot indicates a stable (elliptical) fixed point that is also a local energy minimum. The orange squares indicate saddle points (hyperbolic fixed points). The associated stable/unstable manifolds (dotted blue lines) provide separatrices separating bounded and unbounded motion. (b) Vortex trajectories obtained from solving the time-dependent GPE (3.1). Other parameters are $\nu = 2 \times 10^{-4}\mu$ and $g = \mu\xi^2$.

relative motion Hamiltonian $\tilde{\mathcal{H}}_{\rm rel}$ of Eq. (3.20).

The phase space of a vortex molecule in a channel in the absence of intercomponent interactions is show in Fig. 3.3. The phase space portrait from the point-vortex model in panel (a) is contrasted by the vortex trajectories obtained from GPE simulation in panel (b) with low-energy starting configurations cleaned by imaginary-time evolution. The central local energy minimum [marked with a blue dot in panel (a)] corresponds to a simple vortex of Sec. 3.2.1 located in the center of the channel. It is an elliptic fixed point, and the surrounding elliptic trajectories describe the vortex molecule rotating clockwise around its center of mass. A separatrix (dotted blue line) separates the bounded periodic motion from unbounded trajectories where vortices move mainly under the influence of the boundary-induced image vortices. The yellow marked trajectories correspond to motion where vortices in component 1 and 2 approach each other along the channel boundaries, then perform a partial molecule rotation before they move away from each other along the boundary.

When a repulsive intercomponent interaction of $g_{12} = 0.9g$ is present, the picture changes qualitatively, and the phase space becomes considerably more complex. This is seen in Fig. 3.4. While the dotted (blue) separatrix system with its hyperbolic fixed points stays in place, and outside the phase space remains qualitatively unchanged, the inner domain enclosed by the dotted (blue) separatrix looks very different. Instead of a basin with a single minimum, a distorted Mexican hat shape emerges. Specifically, the central elliptic fixed point that corresponds to the simple vortex configuration [marked with a green diamond in panel (a)] now marks a local energy maximum. This is due to the energy benefit of off-setting the vortices when the cross-component interaction is repulsive, as already seen in Fig. 3.2. As a consequence, the elliptic trajectories surrounding the fixed point have an anti-clockwise orientation in Fig. 3.4 (a) and (b). The rim of the Mexican

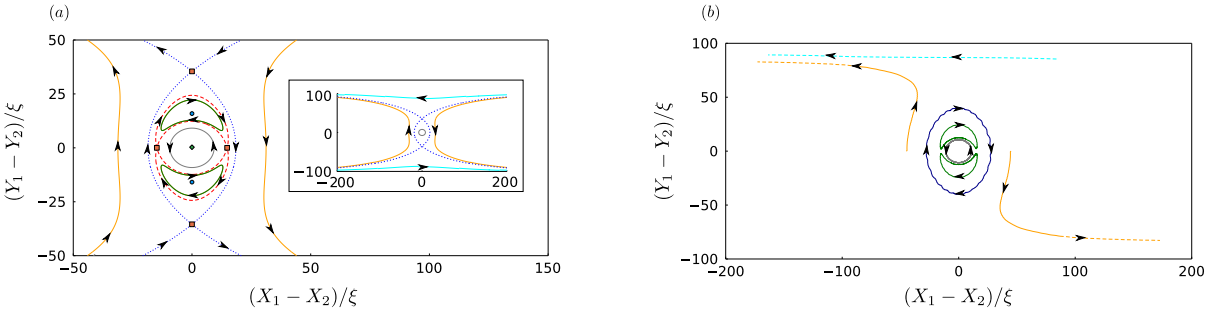

Figure 3.4: Phase space of relative motion for the vortex molecule in a channel of width $D = 100\xi$ in the presence of intercomponent nonlinearity ($g_{12} = 0.9g$). Trajectories are shown as lines with arrows in the relative coordinates of the vortices $X_1 - X_2 = \sqrt{2}\tilde{q}$ and $Y_1 - Y_2 = \sqrt{2}\tilde{p}$ with a hard-wall boundary at $Y_1 - Y_2 = \pm D$. (a) Extended point vortex model of Eqs. (3.13) and (3.14). Symbols indicate fixed points. The round blue dots (local energy minima) and the green diamond (local energy maximum) are elliptical fixed points. The orange squares indicate saddle points (hyperbolic fixed points), which give rise to two different sets of disconnected separatrices (blue dotted lines and dashed orange lines). The inset provides an overview up to the channel boundaries. (b) Vortex trajectories obtained from solving the time-dependent GPE (3.1). Other parameters are $\nu = 2 \times 10^{-4}\mu$ and $g = 0.53\mu\xi^2$.

hat is distorted by the effect of the channel boundaries through $E_{\rm SV}(Y)$. Local energy minima now appear above and below the central fixed point and are marked with blue round dots in panel (a). Saddle points with $Y_1 - Y_2 = 0$ provide hyperbolic fixed points [marked with red squares in panel (a)] and give rise to a new set of separatrices marked with dashed (red) lines.

Due to the changed phase-space structure, we now find crescent shaped trajectories (marked with green lines) that exhibit a rocking motion enclosing the local minima, reminiscent of a rotational pendulum. These trajectories appear close to the equilibrium separation of a vortex molecule in the absence of boundaries seen in Fig. 3.2. For smaller and larger separations, trajectories showing anti-clockwise and clockwise rotational motion, respectively, are now possible.

At higher energies, non-compact vortex trajectories are predicted and observed in both scenarios of Figs. 3.3 and 3.4, where they are marked in yellow and cyan colors. For these trajectories the vortex separation d becomes arbitrarily large, i.e. the vortex molecule is stretched indefinitely. Within the point-vortex model, the vortex interaction energy $V(d)$ is assumed to derive from the contribution of a domain wall that extends in a straight line between the two vortices. For the non-compact trajectories, this energy grows without bounds as d increases. This is compensated for by negative energy contributions from $E_{\rm SV}$ of Eq. (3.7), which diverges logarithmically as a vortex nears the channel boundary.

The non-compact trajectories are interesting, because at some point the vortex interaction energy $V(d)$ will be large enough to account for the creation of a vortex-antivortex pair. Such a pair production of vortices could lead to lowering the total energy, as the vortex filament could be threaded outside the coupled superfluid without energy cost, and thus break the linear dependence of the vortex energy on the

separation d. Quantum, thermal, or other technical fluctuations are necessary to initiate the pair production because there is an energy barrier to overcome.

The GPE simulations are generally found to follow the predictions of the point vortex model. Animations of the GPE real-time evolution are available in the Supplementary Information for trajectories corresponding to rotational-pendulum-like motion, vortex-molecule rotation, and unbounded motion [139]. In addition to the vortices following the characteristic trajectories, small amounts of noise originating from radiation due to vortex acceleration are seen there as well [140].

In our GPE simulations we have not observed vortex pair production upon stretching vortex molecules. However, we have not seen the boundless growth of domain walls with arbitrary length either. Instead we have seen domain walls bending towards the hard-wall boundaries, where the interaction energy can be contained by routing the vortex filament outside the superfluid. An example of the vortex filament exiting the condensate through the boundary is shown in Fig. 3.5 in snapshots taken from the cyan trajectory of Fig. 3.4 (b).

So far we have discussed the dynamics of symmetric configurations where the center of mass was at rest in the middle of the channel. Off-setting the center of mass in the y direction leads to an overall translational motion of the vortex molecule in x direction on top of the internal dynamics described above, as expected from the discussion in Sec. 3.3.3. Additional effects that may be anticipated from the coupling of the relative and center-of-mass degrees of freedom are a distortion of the relative-degree-of-freedom phase space depending of center-of-mass state of motion and vice versa. A deeper study of these effects is beyond the scope of the present work.

3.5 Conclusions

We have set up a point-vortex framework in which vortex molecule dynamics can be explored. Applied to the motion of a vortex molecule in a channel geometry we find that the point-vortex model predicts all important qualitative features of vortex dynamics in the GPE simulation. The point-vortex model is particularly well suited for inspecting the phase space structure in detail. It may be interesting to study vortex-molecule dynamics in other geometries, such as billiards, in the future.

Our model could be further refined by taking into account potential inertial effects in the vortex dynamics [141, 142]. Such inertial effects may be expected in the case where $g_{12} > 0$ due to the partial core filling of a vortex in one component by a density bump in the other. While we have not seen any clear evidence in our simulations, such effects could become more relevant in some situations, e.g. for imbalanced interaction strengths.

The vortex molecule dynamics in the channel geometry is particularly interesting because it produces unbounded trajectories where the vortex molecule is stretched by a competition of the domain wall tension and vortex attraction from the boundaries. Future

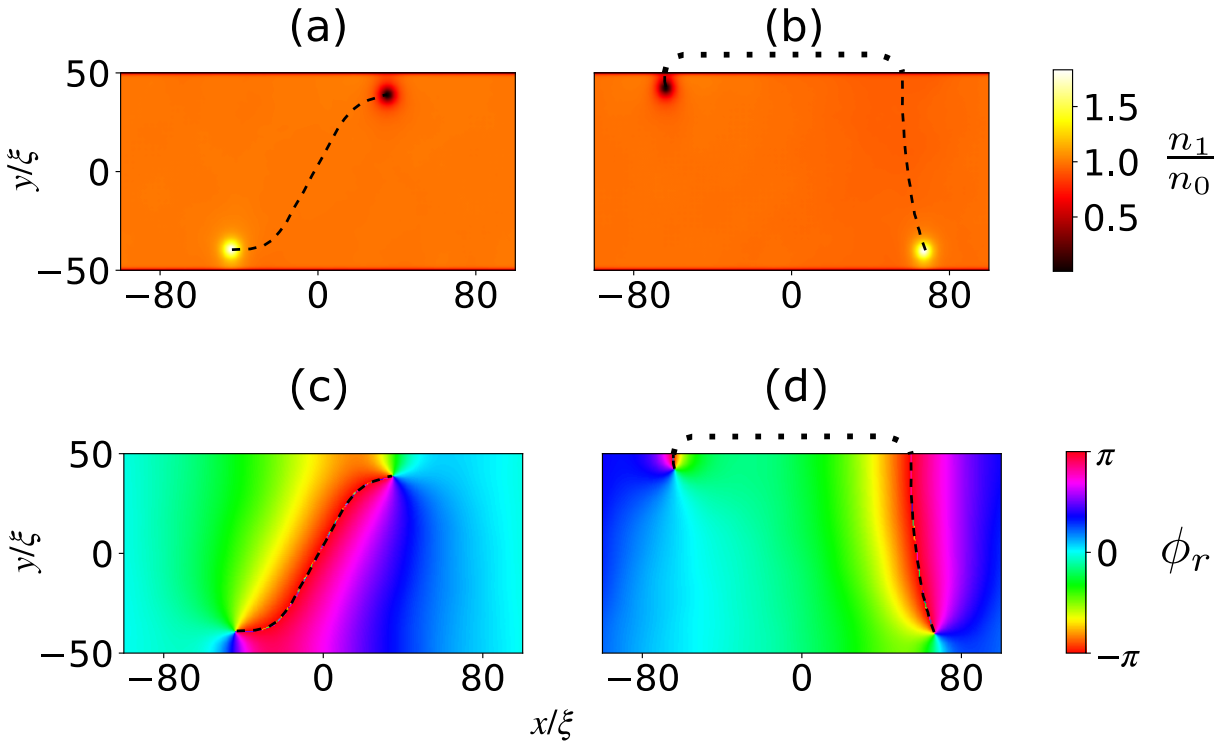

Figure 3.5: Snapshots of the vortex molecule motion in an unbounded trajectory from the time-dependent GPE (3.1). The left column (a), (c) shows an early time and the right column (b) and (d) show a later time in the cyan colored trajectory shown in Fig. 3.4 (b). The top row shows the color-coded normalized density of component 1, $n_1(\mathbf{r})/n_0$ in panels (a) and (b). The positions of the vortices in component 1 and 2 can be inferred from the bright and dark spots, respectively. The bottom row shows the relative phase $\phi_r(\mathbf{r}) = \arg(\psi_1\psi_2^*)$ in panels (c) and (d). The dashed line in all panels marks the line of π phase indicating the presence of a domain wall of the relative phase. The dotted line outside the channel boundaries (on the top and bottom edge) in panels (b) and (d) indicate the topological connection of the domain wall outside of the domain occupied by the superfluid. Parameters are the same as in Fig. 3.4.

work could examine the role quantum fluctuations may play in seeding vortex-antivortex pair creation and thus creating a laboratory analog of color confinement in quantum chromodynamics [116].

Acknowledgements

We thank Ashton Bradley for discussions and for providing code for vortex detection with `VortexDistributions.jl` [138].

3.6 Appendix A: Interaction energy of a vortex molecule

In order to obtain the total energy of a vortex molecule shown in Fig. 3.2 we imprint each condensate with a single vortex phase mask at an equal distance $d_{\mathrm{ini}}/2$ and opposite direction from the center of a square computational domain with dimensions $180\xi \times 180\xi$. We use $d_{\mathrm{ini}} = 60\xi$ in this work. We also locate pinning potentials (peaked Gaussian potentials) on the positions of the phase singularity of each vortex and evolve the system according to Eq. (3.1) in imaginary time until convergence. This creates a vortex molecule with the accurate appropriate phase structure. Then we remove the pinning potential for another round of imaginary time evolution during which the molecular distance d changes towards the equilibrium, and plot the energy vs. distance. This gives us a fairly accurate picture of the interaction energy as a function of molecular distance d. The procedure approximately, but not exactly, produces the minimum energy configuration constrained by the position of the vortex singularities. Indeed, we see small changes in energy values depending on the initial position of the vortex imprint, in particular during early stages of the imaginary time evolution. For this reason we only use data for fitting the parameterization with $d < 40\xi$ when the distance of the initial imprint is $d = 60\xi$, as this data is well converged.

3.6.1 Twisted real projective plane boundary conditions

In order to optimally capture the energy content of a vortex molecule in the absence of boundaries, we use boundary conditions that are designed to approximately generate the density and phase structure expected from a single vortex molecule on an infinite two-dimensional plane. At a distance $r \gg d$ from the vortex molecule, we expect the phase and density structure in each component to be approximately described by that of a simple vortex of Eq. (3.4). This will be exact for a vortex molecule with $d = 0$. Choosing a square domain and placing the vortex molecule in the center, this implies in particular that the phase of each component has exactly a π offset when comparing opposite points on the boundary (by inversion), while the density is the same. Hence we implement boundary

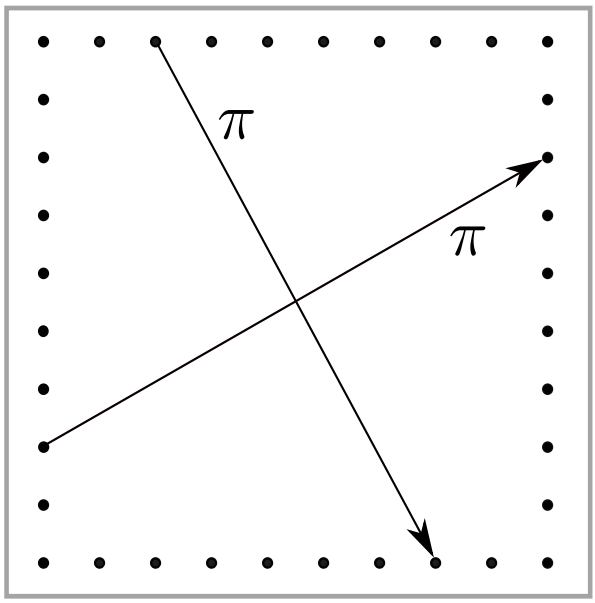

Figure 3.6: Twisted real projective plane boundary conditions. Grid points on the boundary of the computational domain are connected to diagonally opposite points (by inversion) and restricted to have the same modulus and a complex phase offset of π. This applies to both complex fields $\psi_1(x, y)$ and $\psi_2(x, y)$.

conditions that enforce antiperiodicity (i.e. the same modulus but phase offset by π) diagonally across the domain. These boundary conditions implementing a real projective plane with a π phase twist are illustrated in Fig. 3.6. Note that the required phase shift of π across the diagonal leads to an increased energy cost if the vortex molecule is not centered in the computational domain. Thus imaginary time evolution will automatically center the vortex molecule.

The phase structure resulting from applying the twisted real projective plane boundary conditions to a charge 1 vortex molecule is shown in Fig. 3.7. The total phase shown in panel (a) is broadly that of a charge 2 vortex, with the individual unit charges separated at a distance d. The relative phase shown in panel (b) reveals the domain wall located between the vortex positions, and healing towards equal phase well before the boundaries are reached. The residual total phase compared to a centered charge 2 vortex shown in panel (c) reveals that most of this residual is localized close to the vortex molecule with length scale d. However, faint residuals spanning the whole computational domain can also be distinguished.

While Fig. 3.7 mostly supports our assumption that the twisted real projective plane boundaries efficiently remove boundary effects from the simulation, we also repeat the calculation of the vortex molecule energy in computational domains of different size. The results are shown in Fig. 3.8. We see that different box sizes broadly lead to the same energy as a function of molecular distance d, but shifted by a constant value. This is expected as a larger computational domain will integrate a larger part of the energy density of the vortex flow pattern, which ultimately is expected to logarithmically diverge

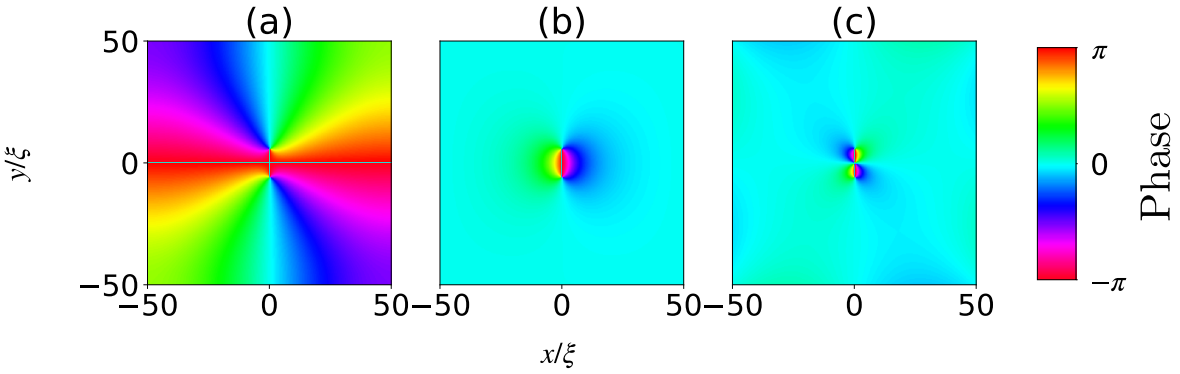

Figure 3.7: Phase structure of a vortex molecule with charge $\kappa = 1$ and $d = 8.5\xi$ under the twisted real projective plane boundary condition. (a) Total phase of the condensates $\arg(\psi_1\psi_2)$. (b) Relative phase $\arg(\psi_1\psi_2^*)$. (c) Residual phase $\arg(\psi_1\psi_2/\psi_s^2)$, where ψ_s is the complex order parameter of a simple vortex of Eq. (3.4), located in the center of the computational domain. The comparison shows that the total phase of the vortex molecule deviates from that of a simple vortex mainly in a narrowly localised region, with some faint residuals extending about the computational domain. Parameters are $g = \mu\xi^2$, $g_{12} = 0$, and $\nu = 2 \times 10^{-3}\mu$.

with increasing the box size. However, this does not matter for the purpose of Hamiltonian dynamics in the extended point-vortex model of Sec. 3.3 where a constant energy offset is irrelevant and does not change the resulting equations of motion. For the smaller box size of 80ξ we can see some deviations from the otherwise parallel behavior of the data shown in Fig. 3.8, which we attribute to a boundary effect. It becomes prominent when the molecular separation d is larger than half of the linear box dimension. Hence, we use the data with the largest box size $180\xi \times 180\xi$ for parametrizing the interaction energy.

3.6.2 Parametrization

For the purpose of the point vortex model it is very convenient to parameterize the interaction energy of a vortex molecule rather than relying on numerical data that is only available at specific discrete values of the molecular distance d. We have performed calculations of the vortex molecule energy as a function of d for altogether four different parameter values as shown in Fig. 3.9.

We fit the curves in Fig. 3.9 with two different functional forms depending on the value of g_{12}. For $g_{12} = 0$ we use

$$V(d) = a l_a \log[\cosh(\frac{d}{l_a})] + b l_b \log[\cosh(\frac{d}{l_b})] + c, \tag{3.21}$$

and for $g_{12} = 0.9g$ we use

$$V(d) = \alpha e^{-d^2/\beta} + \gamma d + \delta, \tag{3.22}$$

where, $a, b, l_a, l_b, \beta, \gamma, \delta$ are fitting parameters. The equilibrium distance of the vortex

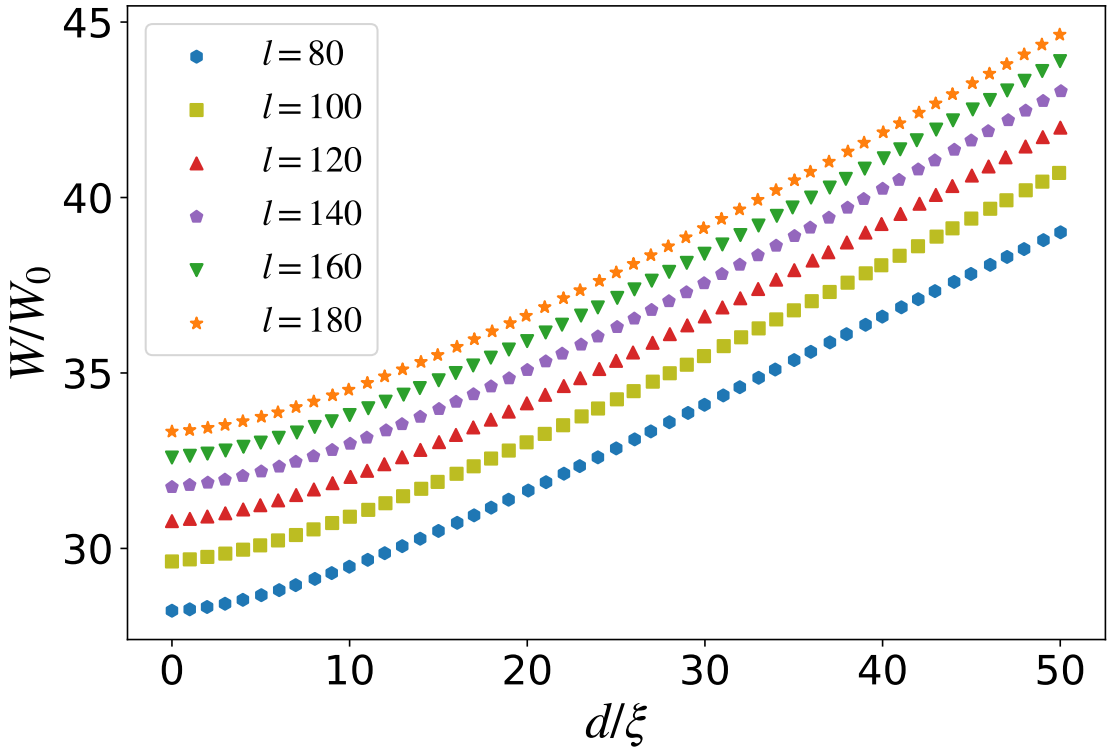

Figure 3.8: Vortex molecule energy as a function of molecular distance d for different sizes $l\xi \times l\xi$ of the computational domain. Different symbols indicate the different sizes l as indicated in the plot legend. The initial distance of vortex seeding is $d_{\text{ini}} = 60\xi$. The slopes vary very little, but each curve is shifted by a constant due to the additional energy of the vortex velocity field captured with the changing size of the computational domain. Other parameters are $g = \mu\xi^2$, $g_{12} = 0$, and $\nu = 2 \times 10^{-3}\mu$.

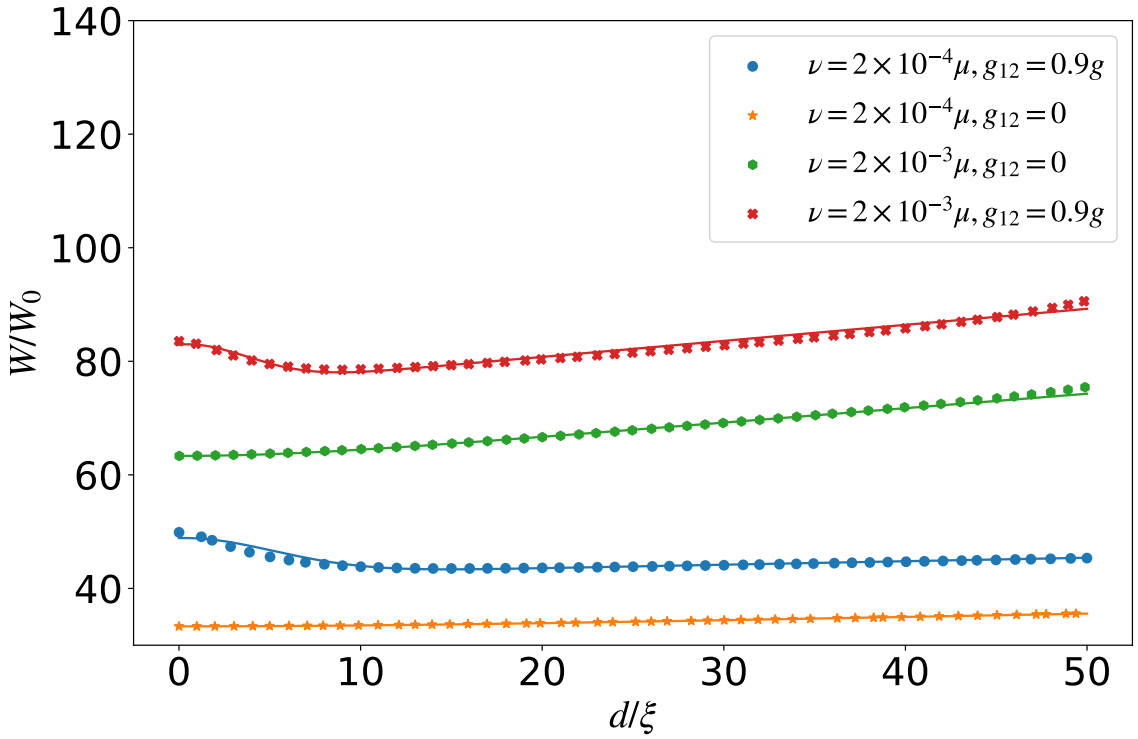

Figure 3.9: Vortex molecule interaction energy and parameterizations for different parameter values. Symbols are numerical data from imaginary time evolution with different values of the constant ν and g_{12} as indicated in the legend. Full lines of the corresponding color are the fits according to Eqs. (3.21) and (3.22). Other parameters are $g = 0.53\mu\xi^2$ when $g_{12} = 0.9g$, and $g = \mu\xi^2$ when $g_{12} = 0$. The molecular distance is measured in units of healing length $\xi = \hbar/\sqrt{m(\mu+\nu)}$ and the energy is measured in $W_0 = \hbar^2(\mu+\nu)/m(g+g_{12})$. Energies corresponding to same values of ν and g_{12} have been shifted by arbitrary amounts for graphical purposes. As is evident non-zero g_{12} creates an energy maxima at zero distance due to the absence of core filling. On the other hand the same values of ν lead to the same slope for large d. Larger ν results in higher tension from the Josephson vortex and steeper energy slopes. The data shown for $\nu = 2\times10^{-3}\mu$ is the same as shown in Fig. 3.2.

Table 3.1: Fitting parameters for $g_{12} = 0.9g$

ν/μ	$d_{\rm eq}/\xi$	β/ξ^2	$\gamma\xi/W_0$	δ/W_0
$2\times10^{-4}\mu$	14.83	53.8687	0.0614	22.3328
$2\times10^{-3}\mu$	8.83	26.9334	0.2824	25.1213

Table 3.2: Fitting parameters for $g_{12} = 0$

ν/μ	$a\xi/W_0$	l_a/ξ	$b\xi/W_0$	l_b/ξ	c$/W_0$
2×10^{-4}	1.0227	17.81416077	-0.96324	17.81416075	33.3192
2×10^{-3}	1.1218	10.0701960	-0.8672	10.0701959	33.3336

molecule is defined as $d_{\rm eq}$. This is the molecular distance of the lowest energy configuration. We set $\alpha = \beta\gamma\exp(d_{\rm eq}^2/\beta)/2d_{\rm eq}$, which ensures that $V(d)$ has a minimum at $d_{\rm eq}$. The relevant parameters for both cases are given in Table 3.1 & 3.2, where ξ is the healing length and $W_0 = \hbar^2(\mu+\nu)/m(g+g_{12})$.

This parametrization gives us a form for the interaction energy between the vortex molecules which we use to predict vortex trajectories along with our analytical model.

MASSEY UNIVERSITY
GRADUATE RESEARCH SCHOOL

STATEMENT OF CONTRIBUTION
DOCTORATE WITH PUBLICATIONS/MANUSCRIPTS

We, the candidate and the candidate's Primary Supervisor, certify that all co-authors have consented to their work being included in the thesis and they have accepted the candidate's contribution as indicated below in the *Statement of Originality*.

Name of candidate:	Sarthak Choudhury
Name/title of Primary Supervisor:	Joachim Brand
Name of Research Output and full reference:	
Sarthak Choudhury and Joachim Brand, "Rotational pendulum dynamics of a vortex molecule in a channel geometry," Phys. Rev. A 106, 043319 (2022).	
In which Chapter is the Manuscript /Published work:	Chapter 3
Please indicate:	
• The percentage of the manuscript/Published Work that was contributed by the candidate:	70
and	
• Describe the contribution that the candidate has made to the Manuscript/Published Work:	
Original draft preparation; manuscript review and editing; data curation and analysis; data visualizaton; implementation of code based on preliminary code by supervisor and relevant data generation.	
For manuscripts intended for publication please indicate target journal:	
Candidate's Signature:	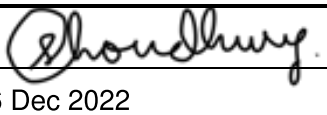
Date:	16 Dec 2022
Primary Supervisor's Signature:	
Date:	15 Dec 2022

(This form should appear at the end of each thesis chapter/section/appendix submitted as a manuscript/ publication or collected as an appendix at the end of the thesis)

Chapter 4

Distributed vorticity model for vortex molecule dynamics

4.1 Introduction

The quantization of vortex lines is a striking feature of superfluids that appears as a consequence of Bose-Einstein condensation [143]. The dynamics of superfluid vortices still poses many open questions and is actively pursued [131, 144–146]. Shortly after the first observation of quantized vortices in a dilute gas Bose-Einstein condensate (BEC) [147], experiments introduced coherent coupling in multi-component BECs by applying a radio-frequency electromagnetic field that drives a Rabi transition between internal (hyperfine) states in the constituent atomic gas [148], with more refined experiments becoming available recently [33, 72, 115]. Theoretical work then examined the peculiar structure of vortices in such a two-component BEC under the continuous influence of coherent coupling [87, 114]. Due to the coherent coupling, the phases of the component condensates align in equilibrium. As a consequence, vortices in the component BECs have to be connected by a vortex line that extends between the two BECs as a domain wall of the relative phase, also known as a Josephson vortex. Analytic solutions for stationary Josephson vortices were first found by Kaurov and Kuklov [89, 90], and families of moving Josephson vortices were characterized in Ref. [88].

Domain walls have an energy content, or surface tension, which is approximately linear in their extent, i.e. length in two dimensions and area in three dimensions. This makes them susceptible to breaking up into smaller fragments. Their dynamical stability is determined by the sign of their effective mass, which depends on the competition between the Rabi coupling and the nonlinear mean-field energy in the BECs [88, 135, 136]. Interesting analogies to axions and quark confinement were first pointed out by Son and Stephanov [87] (see also [37, 38, 116]).

In two-dimensional BECs, a domain wall can either terminate at a boundary of the superfluid domain, or at an appropriately charged vortex in either of the component

BECs. A configuration with same-charge vortices in each component connected by a domain wall is known as a vortex molecule [103]. Sometimes it is referred to as fractional vortex molecule to highlight the fact that the quantized vortex charge can be thought of as being split into fractional charges residing in separate locations at the vortices in each component BEC [36]. Theoretical studies of equilibrium configurations have been extended to vortex molecule lattices [109]. Topological defects analogous to vortex molecules are being investigated experimentally in superfluid ^{3}He [149].

The dynamics of vortex molecules has first been considered by Tylutki *et al.* [117] in the context of a two-dimensional coupled BEC in an isotropic harmonic trap. In this scenario a symmetrically centered vortex molecule rotates with a constant angular frequency around the trap axis, referred to as precession. The vortex molecule dynamics was described by the superposition of three separate velocity components: One derived from the influence of the harmonic trapping potential on the individual (point) vortices in a Thomas Fermi approximation, and two contributions from the Magnus effect related to a short-range core repulsion and an attractive force due to the surface tension of the domain wall. A generalised Magnus force on a quantized vortex gives rise to a transverse velocity component according to $\mathbf{F} = 2\pi n_0 \hbar \hat{\kappa} \times \mathbf{V}$, where n_0 is the superfluid density, $\hat{\kappa}$ is the circulation unit vector, and $\mathbf{V}$ is the velocity of the vortex relative to that of the background superfluid [150, 151]. Calderaro *et al.* [119] then developed a Lagrangian variational formalism focussing on the effect of the domain wall on the vortex dynamics. They obtained analytic results in two different regimes: The attractive Magnus force is linear in the molecular distance d (the length of the domain wall) in the regime of weak Rabi coupling where $\xi_\mathrm{J} \gg d \gg \xi$, and ξ_J is the Josephson vortex length scale (width of the domain wall), and ξ is the condensate healing length. In this regime, the Magnus force contribution to the precession frequency is constant. The other regime of strong Rabi coupling where $d \gg \xi_\mathrm{J} \gg \xi$ is the one considered by Tylutki *et al.* [117] where the Magnus force is constant and provided by the surface tension of an infinite domain wall.

In a previous work we developed an extended point vortex model to analyze the dynamics of a vortex molecule in a flat-bottom trap realizing a channel geometry with parallel hard walls [152]. The model includes the Magnus-force effects of the domain wall and possible core repulsion by parameterizing a numerically-obtained vortex-vortex interaction energy in the absence of domain boundaries. The effects of the hard-wall boundaries are separately taken into account by the method of images applied on the individual component vortices. This theory was able to predict all the qualitative features in the pendulum-like phase space of the vortex molecule dynamics in the channel geometry of Ref. [152].

In this work we aim for a more accurate description of the vortex-molecule dynamics in the presence of hard-wall trapping potentials. Instead of treating the component vortices as localized point vortices, we consider the vorticity to be distributed along the domain wall connecting the component vortices for the purpose of generating image vorticity. This

is motivated by the fact that over length scales larger than the molecular separation and the Josephson length scale, the phase of both condensate components aligns in numerical simulations.

Figure 4.1 shows the density and phase features of a vortex molecule from a numerical solution of the Gross-Pitaevskii equation (GPE). The component vortices are clearly distinguished by their low-density cores (dark dots) in panels (a) and (b). They also give rise to phase singularities (all colors of the rainbow meeting in a single point) in the phase plots in panels (c) and (d). The domain wall is clearly visible as a region of large phase gradients in panel (c), showing the relative phase between the two condensates. The fact that the relative phase nearly vanishes outside of the localised domain wall indicates that both condensates have the same phase structure. This observation is inconsistent with the assumptions of the extended point vortex model of Refs. [117, 152], where the point vortices are located at different positions in the component condensates, namely at either end of the vortex molecule, which leads to a global misalignment of the component phase fields. In addition to the numerical observations, it also makes sense to assume that the phases of the component condensates align outside of the immediate vicinity of the domain wall, as this will minimise the local energy density [153].

Modelling instead the component vortices by a vorticity distribution that is equal in each component condensate and distributed along the domain wall, the phase of the two condensates is identical everywhere outside the domain wall. For the purpose of the distributed vorticity model we will assume a uniform vorticity distribution along the domain wall, which is modelled as a (narrow) straight line extending over the size of the molecule. The uniform distribution is the simplest assumption that can be made, and is furthermore consistent with a constant total phase of the component condensates, as it is observed in the GPE simulation, see Fig. 4.1(d). In essence, the assumption of a distributed vorticity along the molecular axis represents the action of the domain wall on the relative phase, but shrunken to a line of zero width.

The assumed distributed vorticity is relevant for the vortex molecule dynamics by generating a continuous distribution of image vortices from the boundaries of the trap. In the following we consider a flat-bottom trap, which is modeled as a container with hard wall boundaries. The concept of a distributed vorticity is thus used in a very different context than in Ref. [154], where distributed image vorticity was found useful in modelling the vortex motion in a single condensate while dealing with a Thomas-Fermi parabolic density profile (or soft boundaries).

Additional Magnus-force contributions to the dynamics originating from the domain-wall surface tension and core-interaction are obtained from the numerically generated vortex-molecule interaction energy as in our previous work [152]. For the current work we use a more accurate representation of the numerical data compared to the parameterization used in Ref. [152], combining interpolation and extrapolation,

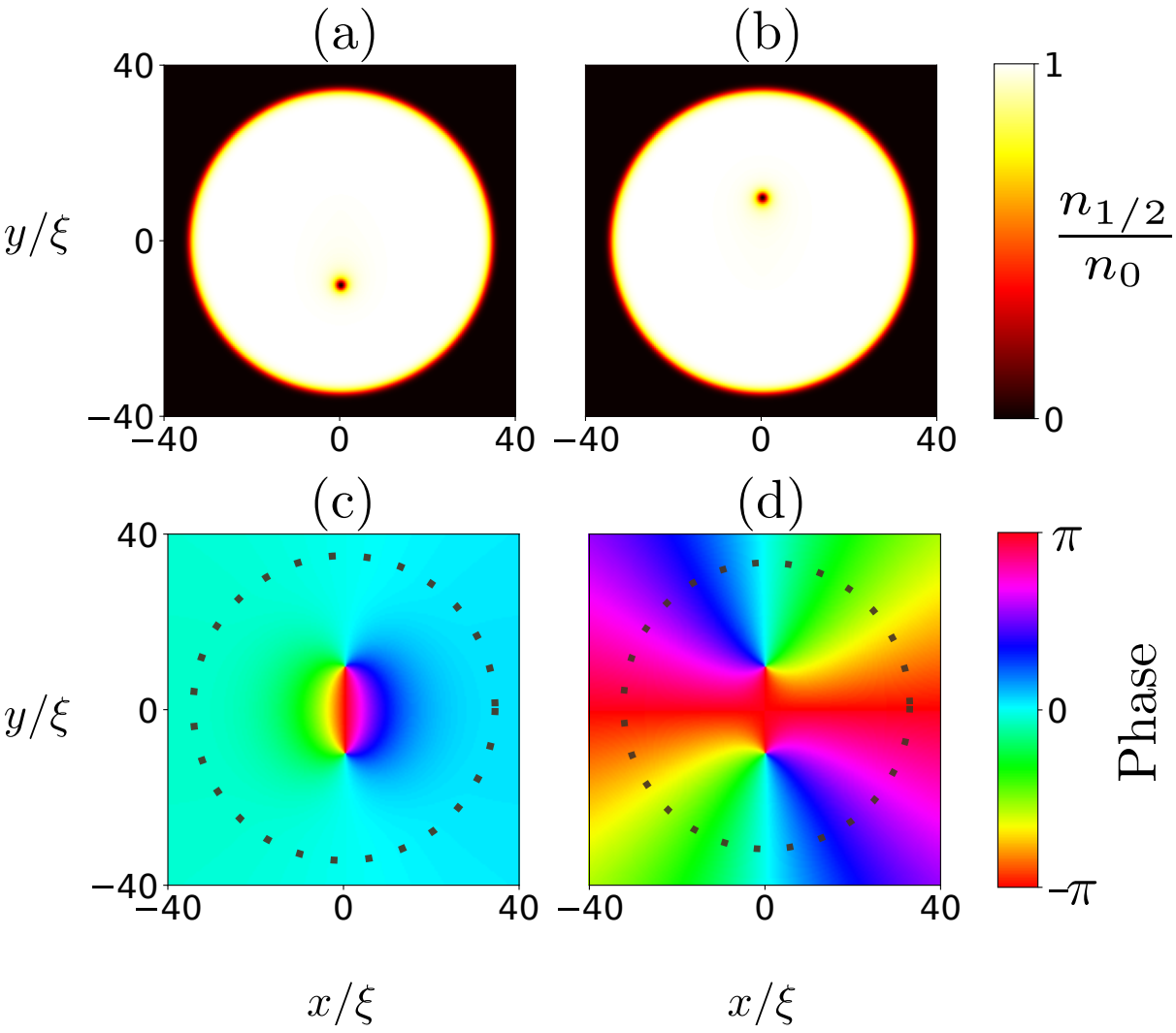

Figure 4.1: Vortex molecule in a disc. Numerical solution of the GPE (4.1) with a centered vortex molecule with molecular length $d = 20\xi$ in a disc-like trap described by Eq. (4.5). (a) Density of condensate 1, $n_1 = |\psi_1|^2$. (b) Density of condensate 2, $n_2 = |\psi_2|^2$. (c) Relative phase $\arg(\psi_1\psi_2^*)$. (d) Total phase $\arg(\psi_1\psi_2)$. The black dotted circles in panels (c) and (d) denote the trap boundary at the disk diameter of $2L = 70\xi$. Other parameters are $\nu = 2 \times 10^{-3}\mu$, $g_{12} = 0$.

which we found necessary in order to obtain quantitative agreement with fully numerical simulations of the vortex molecule dynamics. The new parametrization is now consistent with the regimes of weak and strong Rabi coupling examined analytically in Ref. [119].

We derive and solve the equations of motion for the distributed vorticity model for the case of a single vortex molecule in a disc shaped domain with hard wall boundary conditions. This situation could be achieved in BEC experiments with a flat-bottom trap. The model solutions are compared with fully numerical solutions of the GPE. We also compare with the simpler method of images for point vortices and a simplified description of the surface tension that is linear in the domain wall size and find that the refined model gives the best agreement with the GPE data.

The chapter is structured as follows. Section 4.2 introduces the coupled GPE governing the system of coherently coupled condensates. Section 4.3 introduces the point vortex formulation and reviews the extended point vortex model before defining the distributed vorticity model. The general formulations are applied to the dynamics of a vortex molecule in a flat-bottom trap in Sec. 4.4 before concluding in Sec. 4.5. Appendix 4.7 provides relevant details for the parameterization of the interaction energy and Appendix. 4.8 discusses the calculation of the general integrals of the charge distribution model.

4.2 Mean-Field Formulation

We characterize two coherently coupled atomic Bose-Einstein condensates with complex order parameters, $\psi_1(\mathbf{r},t)$ and $\psi_2(\mathbf{r},t)$ in the mean-field description of coupled GPEs

$$i\hbar\frac{d\psi_1}{dt} = \left(\hat{h} - \mu + g_1|\psi_1|^2 + g_{12}|\psi_2|^2\right)\psi_1 - \nu\psi_2, \tag{4.1a}$$

$$i\hbar\frac{d\psi_2}{dt} = \left(\hat{h} - \mu + g_2|\psi_2|^2 + g_{12}|\psi_1|^2\right)\psi_2 - \nu\psi_1, \tag{4.1b}$$

where $\hat{h} = -\frac{\hbar^2}{2m}\nabla^2 + V_{\text{ext}}$ is the single-particle Hamiltonian for bosons of mass m. The chemical potential μ controls the number of particles in numerical simulations. The spatially homogeneous coherent (Rabi) coupling ν can be realized by a two photon microwave field or a driving radio frequency. The atoms are assumed to be strongly confined along the z spatial dimension to realize a quasi two dimensional quantum gas with a positional coordinate denoted as $\mathbf{r} = (x,y)^{\text{t}}$. Additional box-like confinement in the two-dimensional plane is provided by the external potential $V_{\text{ext}}(\mathbf{r})$, which we take to vanish inside the superfluid domain and rising sharply at the domain boundaries. This will create a uniform quasi-two-dimensional Bose-Einstein condensate with rigid (hard-wall) boundaries as realized, e.g., in Ref. [130].

Our zero temperature theory is applicable to the low temperature and high particle-number-density regime of experiments [130]. The free energy associated with

the GPE (4.1) is given by the integral

$$W = \int \Bigg[\sum_{i=1}^{2} \left(\psi_i^* \hat{h} \psi_i + \frac{g_i}{2} |\psi_i|^4 - \mu |\psi_i|^2 \right) + g_{12} |\psi_1|^2 |\psi_2|^2 - \nu (\psi_1^* \psi_2 + \psi_1 \psi_2^*) \Bigg] \mathrm{d}^2 r. \tag{4.2}$$

In order to reduce the number of parameters, we choose equal intra-component interactions $g_1 = g_2 \equiv g$. The homogeneous and time-independent ground-state solution of Eq. (4.1) for $V_{\mathrm{ext}} = 0$ is given by equal and constant density $n_{1/2} \equiv |\psi_{1/2}|^2 = (\mu + \nu)/(g + g_{12}) \equiv n_0$ in the component condensates. We are interested in the miscible regime where $g + |\nu|/n_0 > g_{12}$ [74]. The homogeneous solution n_0 serves as the background bulk density for localized vortex or non-linear-wave solutions. The linear coupling $\nu > 0$ ensures that component condensates phases align and thus $\psi_1 = \psi_2$ in equilibrium [132], but a global phase factor remains undetermined due to a global $U(1)$ symmetry of the coupled BECs. The healing length

$$\xi = \frac{\hbar}{\sqrt{m(g + g_{12})n_0}} = \frac{\hbar}{\sqrt{m(\mu + \nu)}} \tag{4.3}$$

provides the length scale on which a homogeneous solution is recovered away from forced local inhomogeneities due to vortex cores, or boundary conditions [42].

A point vortex model, nominally applicable to an incompressible fluid, requires that the healing length is smaller than other relevant length scales like the separation of vortices, or the distance of vortices from the boundaries [59, 155]. Reference [129] showed how to relax the incompressibility condition of the point vortex model and obtain correction terms for vortex dynamics as a series expansion in ξ^2/D^2, where D is a length scale of the superfluid domain. Vortex molecules introduce two additional length scales on top of the healing length. The molecular size d is the separation between the vortex singularities in the component vortices and also determines the length of the domain wall in the relative phase in situations where the domain wall extends along a straight line connecting the component vortices. The third length scale

$$\xi_{\mathrm{J}} = \frac{\hbar}{\sqrt{4m\nu}}, \tag{4.4}$$

is called the Josephson vortex length scale and determines the width of the domain wall connecting the two component vortices. Exact solutions for a stationary and moving Josephson vortex were characterized in Refs. [89] and [88], respectively.

In the numerical example shown in Fig. 4.1 the molecular size $d = 20\xi$ is slightly larger than that Josephson length scale $\xi_{\mathrm{J}} \approx 11.2\xi$. The domain wall of the relative phase is clearly seen as a feature with large phase gradients in the relative phase in panel (c). We can understand the domain wall to be centered around the line of constant relative

phase $\arg(\psi_1\psi_2^*) = \pm\pi$ and extending over a width of ξ_J. In the distributed vorticity model proposed in this work the domain wall is reduced to a straight line of zero width along which the vorticity of the vortex molecule is distributed. The model thus assumes that both the healing length ξ and the Josephson length ξ_J are small compared to any other length scale, including the domain size D and the molecular size d.

The numerical vortex-molecule solution of the coupled GPE (4.1) show in Fig. 4.1 models a disc-shaped two-component BEC. The disc-shaped radially-symmetric external potential of radius L is described by

$$V_{\text{ext}}(\mathbf{r}) = (\mu + \nu)\left(1 + \tanh\frac{|\mathbf{r}| - L}{\xi}\right). \tag{4.5}$$

The solution shown in Fig. 4.1 was obtained by first imprinting a single vortex in each condensate component at the desired locations $\mathbf{R}_1$, $\mathbf{R}_2$. A low energy solution is then obtained by evolving Eq. (4.1) in imaginary time, i.e. replacing $t \to -i\tau$, which corresponds to minimizing the energy functional W by gradient flow. Imaginary time evolution quickly removes most density and non-topological phase excitations. On a slower timescale, the location of vortex phase singularities move towards lower energy configurations, which eventually moves them outside the trap. To avoid this, Gaussian pinning potentials are used to pin the vortices in a particular configuration for each vortex while only having minimal effect on the phase and density structure. While the obtained solutions are stationary only in the presence of the pinning potential, they also serve as suitable initial conditions for studying vortex dynamics under real-time evolution of the coupled GPE (4.1) after the pinning potentials are removed. Under the assumptions of the point vortex model, the vortex dynamics only depends on the instantaneous position of the vortex singularities by evolving through minimal energy configurations. This neglects, in particular, the effects of sound emission or reabsorption. We test the predictions of the point vortex model by comparing with fully time-dependent GPE dynamics. Vortex positions are tracked by accurately locating the phase singularities using the software library `VortexDistributions.jl` [138].

4.3 Point vortex formulation

The idea of the point vortex model is that the dynamics of vortices is fully determined by the positions of all vortices in the system together with the boundary conditions. The model strictly applies to ideal inviscid and incompressible fluids [59, 60], and can be applied to the GPE in situations where the healing length ξ can be considered a small parameter [129, 155]. For an ideal fluid in two dimensions one can define a scalar stream function whose contours are co-linear with the local fluid velocity $\mathbf{u}(\mathbf{r})$. The velocity of a point vortex at position $\mathbf{R}$ can be found from the stream function after the singular contribution of the vortex itself has been removed [60]. While the stream function cannot

be used for multi-component coupled BECs, an alternative approach based on energy conservation is still applicable.

The idea is to find the point vortex trajectories as the contours of a conserved energy function, which only depends on the vortex coordinates after the boundary conditions are defined. This leads to a Hamiltonian formulation where the vortex x and y coordinates play the role of canonically conjugate variables. In this formulation additive contributions to the total energy provide additive contributions to the vortex velocity.

4.3.1 Extended point vortex model for the vortex molecule

In Ref. [152] we presented an extended point vortex model where the total energy of a vortex molecule is given by

$$E_{\rm vm}(\mathbf{R}_1,\mathbf{R}_2) = E_{\rm bound}(\mathbf{R}_1,\mathbf{R}_2) + V(|\mathbf{R}_1-\mathbf{R}_2|), \tag{4.6}$$

where $\mathbf{R}_j = (X_j, Y_j)^{\rm t}$ is the coordinate vector of the jth component vortex, $E_{\rm bound}(\mathbf{R}_1,\mathbf{R}_2)$ is an energy contribution from the boundary-induced image vortices, and $V(d)$ is an internal energy of the vortex molecule that only depends on the separation of the component vortices, or the molecular size, $d = |\mathbf{R}_1 - \mathbf{R}_2|$. The trajectories of the component vortices are then obtained from the equation of motion

$$\dot{\mathbf{R}}_j = \nabla_j^{\perp} \frac{E_{\rm vm}(\mathbf{R}_1,\mathbf{R}_2)}{2\pi n_0 \hbar\kappa}, \tag{4.7}$$

$$\tag{4.8}$$

where $\kappa = \pm 1$ is the integer vortex charge and

$$\nabla_j^{\perp} = \begin{pmatrix} \frac{\partial}{\partial Y_j} \\ -\frac{\partial}{\partial X_j} \end{pmatrix} \tag{4.9}$$

is the projection of the curl onto the x–y plane. The equation of motion (4.7) has the structure of Hamilton's equations of motion common to the Hamiltonian formulation of point vortex dynamics [60]. As a consequence of the two energy contributions of Eq. (4.6) the equation of motion has two contributions to the point vortex velocity:

$$\dot{\mathbf{R}}_j = \mathbf{V}_j^{\rm bound} + \mathbf{V}_j^{\rm int}. \tag{4.10}$$

Reference [152] made specific assumptions for the two terms in Eq. (4.6): The boundary term was provided by the method of images for each component vortex separately

$$E_{\rm bound}(\mathbf{R}_1,\mathbf{R}_2) = E_{\rm sv}(\mathbf{R}_1) + E_{\rm sv}(\mathbf{R}_2), \tag{4.11}$$

where $E_{\rm sv}(\mathbf{R})$ is the energy contribution of a single vortex in the superfluid within the given boundaries, i.e. incorporating the contributions from image vortices. As a consequence, the point vortex velocity contributions in the equation of motion become

$$\mathbf{V}_j^{\rm bound} = \mathbf{V}_j^{\rm sv} \equiv (2\pi n_0 \hbar\kappa)^{-1} \nabla^{\perp} E^{\rm sv}(\mathbf{R})|_{\mathbf{R}=\mathbf{R}_j} \tag{4.12}$$

$$\mathbf{V}_j^{\rm int} = (2\pi n_0 \hbar\kappa)^{-1} \frac{{\rm d}V(d)}{{\rm d}d} \nabla_j^{\perp} |\mathbf{R}_1 - \mathbf{R}_2|. \tag{4.13}$$

The interaction energy $V(d)$ was parameterized from a numerical calculation of the vortex-molecule energy in the absence of boundaries. This model provided an adequate description of the dynamics of the vortex molecule in a channel with parallel side walls and was able to reproduce all qualitative phase space structures in Ref. [152].

We note, however, that this model is too simplistic for a fully quantitative description of vortex-molecule dynamics. In particular, the velocity contribution of the boundary term $\mathbf{V}_j^{\rm sv}$ originates from the image vortices of the component vortex at position $\mathbf{R}_j$ only. We know however that the phase structure of the component condensates is not independent of each other but rather strongly influenced by the Rabi coupling. A domain wall of the relative phase extends between the component vortices roughly along the molcular axis. At distances larger than $\xi_{\rm J}$ away from the domain wall, the relative phase drops to zero and the phases of each component BECs align, see Fig. 4.1.

This observation motivates us to modify the extended point vortex model by considering an image vortex distribution extended along the image of the domain wall of the relative phase. For this work we retain the formulation of the extended point vortex model of Eqs. (4.6) and (4.7), but improve the approximate representation of the two energy terms. For the interaction energy $V(d)$ we use a more accurate numerical representation based on the same numerical calculation as detailed in Appendix 4.7. An improved representation of the boundary contributions to the vortex molecule equation of motion is the subject of the distributed vorticity model.

4.3.2 Distributed vorticity model

Due to the effect of the boundaries each vortex obtains a velocity component that can be thought of as the linear superposition of velocity fields induced by all image vortices at the position of that vortex. Let

$$\kappa \mathbf{u}_{\rm im}(\mathbf{r}; \mathbf{R}) \tag{4.14}$$

denote the velocity field induced by the images of a vortex at position $\mathbf{R}$ with charge κ. The boundary-induced velocity contribution in the extended point vortex model of Sec. 4.3.1 of vortex j then becomes

$$\mathbf{V}_j^{\rm sv} = \kappa \mathbf{u}_{\rm im}(\mathbf{R}_j; \mathbf{R}_j). \tag{4.15}$$

For the distributed vorticity model we take the source of image vorticity to be distributed along the domain wall of the relative phase extending between the two component vortices of the vortex molecule, i.e. along the molecular axis. Thus the velocity component of vortex j originating from the image vorticity becomes a superposition of velocity contributions

$$\mathbf{V}_j^{\mathrm{dv}} = \kappa \int_0^1 \mathbf{u}_{\mathrm{im}}(\mathbf{R}_j; (1-t)\mathbf{R}_1 + t\mathbf{R}_2)\mathrm{d}t. \tag{4.16}$$

Figure 4.2 is a concept diagram that shows how the distributed vorticity of the vortex molecule can be thought of as being composed of individual vortices of fractional charge, giving rise to a distribution of image vortices in turn. The placement of image vortices is chosen such that the no-flow boundary condition for flow perpendicular to the disk boundary is satisfied. In the following we will apply these ideas to the disc geometry.

4.4 Vortex molecule dynamics in a flat-bottom disc trap

4.4.1 Velocity of a simple vortex in a disc

The simple vortex solution in the two-component condensate can be understood as a special case of a vortex molecule where the two vortices are at the same location. In this case the phases of the two component condensates can align perfectly and thus no domain wall of the relative phase is present. The velocity of the simple vortex in a disc is thus completely determined by the contribution from the boundaries. Moreover, the predictions from the extended point vortex model and from the distributed vorticity model trivially agree and become equivalent to the point vortex model for a single-component superfluid.

In the point vortex model we ignore the compressibility of the superfluid, formally taking $\xi \to 0$, and assume a constant condensate density. The phase of the GP order parameter of a single vortex at position $\mathbf{R} = (X, Y)^{\mathrm{t}}$ is given by $\arg[\psi(\mathbf{r})] = \kappa \arctan \frac{y-Y}{x-X}$ in the absence of boundaries (up to a constant), and the correponding velocity field is

$$\mathbf{u}(\mathbf{r}) = \frac{\hbar}{m}\nabla \arg(\psi) = \frac{\hbar\kappa}{m}\frac{\hat{z} \times (\mathbf{r} - \mathbf{R})}{|\mathbf{r} - \mathbf{R}|^2}. \tag{4.17}$$

The influence of the box-like trapping potential is to create a no-flow boundary condition, i.e. a condition that prohibits a perpendicular component of the superfluid velocity distribution at the boundary. For a circular disc centered at the origin with radius L this boundary condition is met by adding an image vortex with charge $-\kappa$ at

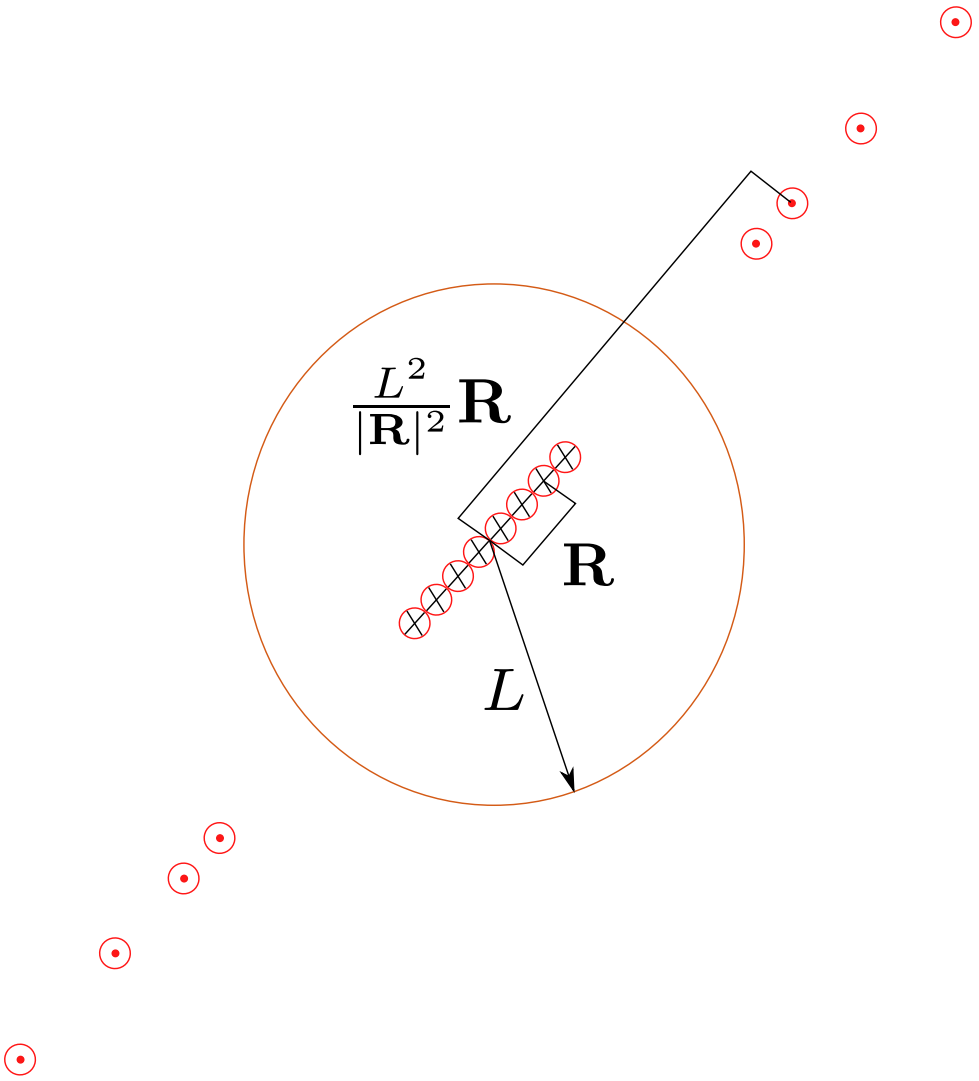

Figure 4.2: Concept diagram of the vorticity distribution model for a centered vortex molecule in a disc trap. The image vortices are formed at locations $\tilde{\mathbf{R}} = \frac{L^2}{|\mathbf{R}|^2}\mathbf{R}$ where $\mathbf{R}$ is the position of the original charge. The distance of the image vortices from the center of the condensate is inversely proportional to the distance of its original vortex from the center. Hence, even though the charge distribution is evenly spaced the image charges are not and reach out to infinity as $|\mathbf{R}| \to 0$.

the position [60]

$$\tilde{\mathbf{R}} = \frac{L^2 \mathbf{R}}{|\mathbf{R}|^2}. \tag{4.18}$$

The velocity field induced by the image of a vortex with charge κ at position $\mathbf{R}$ is thus

$$\kappa \mathbf{u}_{\rm im}(\mathbf{r}; \mathbf{R}) = -\frac{\hbar\kappa}{m} \frac{\hat{z} \times (\mathbf{r} - \tilde{\mathbf{R}})}{|\mathbf{r} - \tilde{\mathbf{R}}|^2}. \tag{4.19}$$

The boundary contributions to the velocities of the component vortices in a vortex molecule can now be obtained by substituting Eq. (4.19) into Eqs. (4.15) and (4.16) for the extended point-vortex model and the distributed vorticity models, respectively. The full equation of motion for the vortex molecule is then given by Eq. (4.10) in combination with Eq. (4.13).

4.4.2 Precession of a centered vortex molecule

In order to quantitatively compare between the different models, we now focus on the situation where the vortex molecule is located symmetrically in the center of the disc with $\mathbf{R}_1 = -\mathbf{R}_2$ and $|\mathbf{R}_j| = d/2$. In this case the symmetry is preserved during the vortex motion. The point vortex velocity is perpendicular to the molecular axis and the vortex molecule rotates with a constant precession frequency around the axis of the disc trap

$$\begin{aligned} \Omega_{\rm vm} \hat{\mathbf{z}} &= \frac{\mathbf{R}_j \times \mathbf{V}_j}{|\mathbf{R}_j|^2}, \\ &= (\Omega_{\rm bound} + \Omega_{\rm int}) \hat{\mathbf{z}}, \end{aligned} \tag{4.20}$$

which breaks up into components originating from the boundary and interactions as per Eq. (4.10). The interaction contribution to the precession frequency becomes, from Eq. (4.13)

$$\Omega_{\rm int} = \frac{\kappa}{\pi n_0 \hbar d} \frac{{\rm d}V(d)}{{\rm d}d}. \tag{4.21}$$

In a situation where the domain wall energy is purely linear in d, as derived for $d \gg \xi_{\rm J}$ in Ref. [119], the gradient term is constant and the interaction contribution to the precession frequency becomes inversely proportional to the molecular length scale d. This term is divergent for small d.

For the boundary contribution $\Omega_{\rm bound}$ we consider the single vortex contribution from the extended point vortex model and the distributed vorticity model. The precession frequency from the extended point vortex model becomes [from Eqs. (4.15) and (4.19)]

$$\Omega_{\rm sv}(d) = -\frac{\hbar\kappa}{m} \frac{4}{4L^2 - d^2}. \tag{4.22}$$

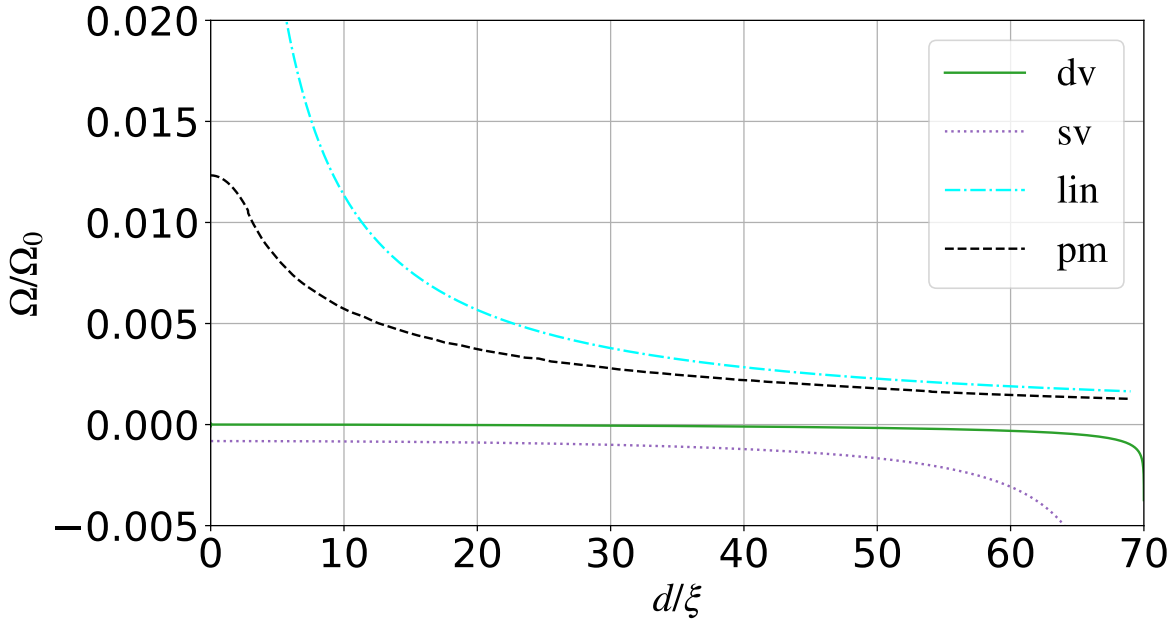

Figure 4.3: Components of the vortex molecule precession frequency according to various models as a function of the molecular size d. The negative-valued boundary contributions Ω_{bound} are labeled "dv" for the distributed velocity contribution Ω_{dv} of Eq. (4.23) and "sv" for the single vortex contribution Ω_{sv} of Eq. (4.22). The interaction components Ω_{int} follow Eq. (4.21) and bring positive contributions. The one labeled "lin" follows from a purely linear interaction potential with the surface tension of the idealized Josephson vortex. The contribution from the parameterized numerically obtained interaction energy is labelled "pm". The frequency is expressed in units of $\Omega_0 = (\mu + \nu)/\hbar$. Parameters are same as Fig. 4.1

This is the result of Ref. [152]. Obtaining the precession frequency of the distributed vorticity model requires evaluating the integral in Eq. (4.16). A closed form solution can be found and leads to

$$\Omega_{\mathrm{dv}}(d) = \frac{\hbar\kappa}{m}\frac{4}{d^4}\left[d^2 - 2L^2 \ln\left(\frac{4L^2 + d^2}{4L^2 - d^2}\right)\right]. \tag{4.23}$$

Expanding in powers of d in the vicinity of $d = 0$ we obtain

$$\Omega_{\mathrm{dv}}(d) = -\frac{\hbar\kappa}{m}\frac{d^2}{12L^4} + \mathrm{O}(d^6), \tag{4.24}$$

where the leading term is of second order in d. Thus, the boundary contribution to the precession frequency from the distributed vorticity model vanishes at small molecular size. This is in contrast to the single-vortex contribution from the extended point vortex model of Eq. (4.22), which has the finite limit $\Omega_{\mathrm{sv}}(0) = -\hbar\kappa/mL$. A comparison of the different contributions to the precession frequency is shown in Fig. 4.3.

Figure 4.3 also shows two different curves for Ω_{int} according to different models for the interaction energy of the vortex molecule. The simplest choice with a linear d dependence

is

$$V_{\rm lin}(d) = d\,\sigma, \tag{4.25}$$

where

$$\sigma = \frac{8\hbar\sqrt{\nu}}{3\sqrt{m}}\frac{3\mu-\nu}{g+g_{12}}, \tag{4.26}$$

is the energy (line density) of a Josephson vortex [89], the exact solution for a non-moving domain wall of the relative phase. Reference [117] used this model with an approximate domain wall energy density from Ref. [87] valid for small ν, which was also derived for $d \gg \xi_{\rm J}$ in Ref. [119].

As an alternative we have parameterized the numerically computed vortex molecule interaction energy $V_{\rm pm}(d)$. The numerical calculation of the interaction energy was first reported in Ref. [152]. For the current work we have re-parameterized the numerical data in order to obtain increased accuracy as detailed in Appendix 4.7. As an alternative we have parameterized the numerically computed vortex molecule interaction energy $V_{\rm pm}(d)$. The numerical calculation of the interaction energy was first reported in Ref. [152]. For the current work we have re-parameterized the numerical data in order to obtain increased accuracy as detailed in Appendix 4.7. We find that the parameterized numerical interaction energy as well as the derived frequency contribution $\Omega_{\rm pm}$ are significantly smaller than the linear model and deviate from it quite strongly for small and moderate values of d while it asymptotically agrees at large d, as is expected.

In Fig. 4.4 we show numerical results for the vortex molecule precession frequency from GPE simulations in comparison with model predictions combining different components for the boundary and interaction contributions. For small molecular size d the values of the precession frequency are dominated by the interaction contributions. The linear interaction energy model leads here to a divergent contribution, which is unphysical. The parameterized interaction contribution however, captures the numerically observed finite precession frequency at small molecular sizes rather nicely. Up to intermediate molecular sizes compared to the disk radius of $L = 35\xi$ the distributed vorticity and the single vortex contributions differ by an approximately constant shift with the gap widening for larger d. Over a wide range of molecular distances, the distributed vorticity model provides a better match with the GPE simulation data compared to the single vortex image model.

At large molecular size, where d becomes comparable to the disk diameter $2L$, the otherwise favored model "dv+pm" develops discrepancies from the GPE simulations seen in Fig. 4.4. In order to rationalize the failure of the model in this regime we visualize the numerical solution of the GPE for a large vortex molecule in Fig. 4.5. The component vortices are close to the boundaries of the disk trap in this case. While the relative phase in panel (c) clearly shows a strong feature reminiscent of a domain wall in the relative phase, it can also be seen that the relative phase does not return to values close to zero outside

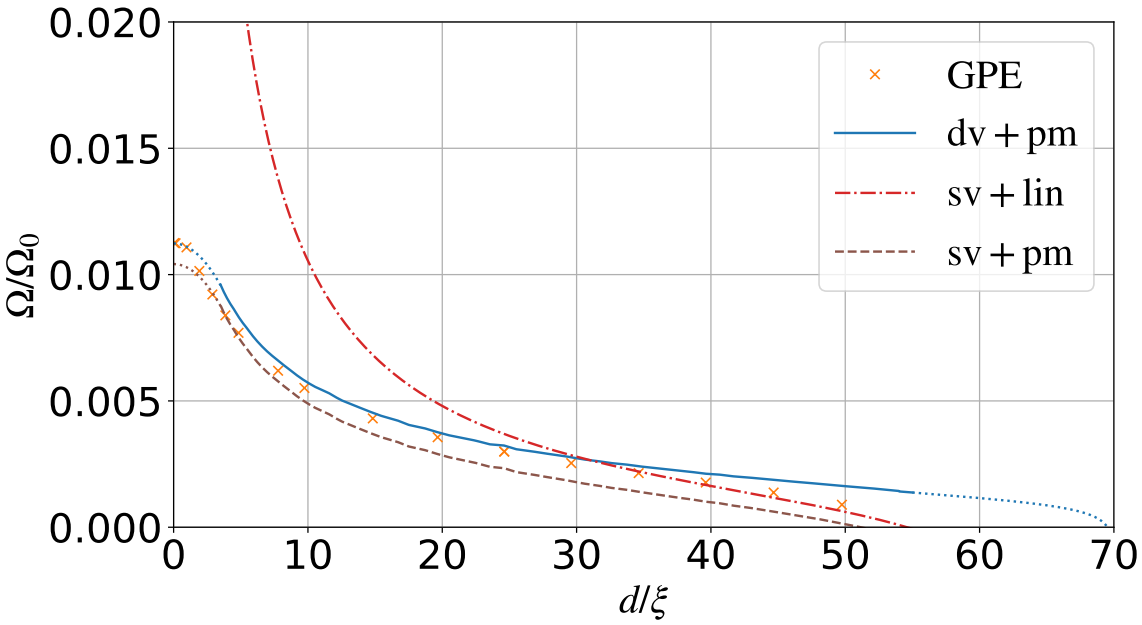

Figure 4.4: Precession frequency of a centered vortex molecule in a disc trap as a function of the molecular size d. The orange crosses represent real time evolution data from the GPE of Eq. (4.1). The curves are model predictions according to Eq. (4.20) with different combinations of the contributions for Ω_{bound} and Ω_{int} shown in Fig. 4.3. The blue solid line marked "dv+pm" combines the distributed vorticity variant of the boundary contribution with the parametrized interaction energy and provides the best explanation of the numerical GPE data within the available models. The red dot-dashed line marked "sv+lin" represents single vortex boundary contribution from Eq. (4.22) along with the linear interaction energy contribution from Eq. (4.25). The brown dashed line marked "sv+pm" represents single vortex boundary contribution along with parametrized interaction energy contribution. The frequency is expressed in units of $\Omega_0 = (\mu + \nu)/\hbar$. Parameters are same as Fig. 4.1

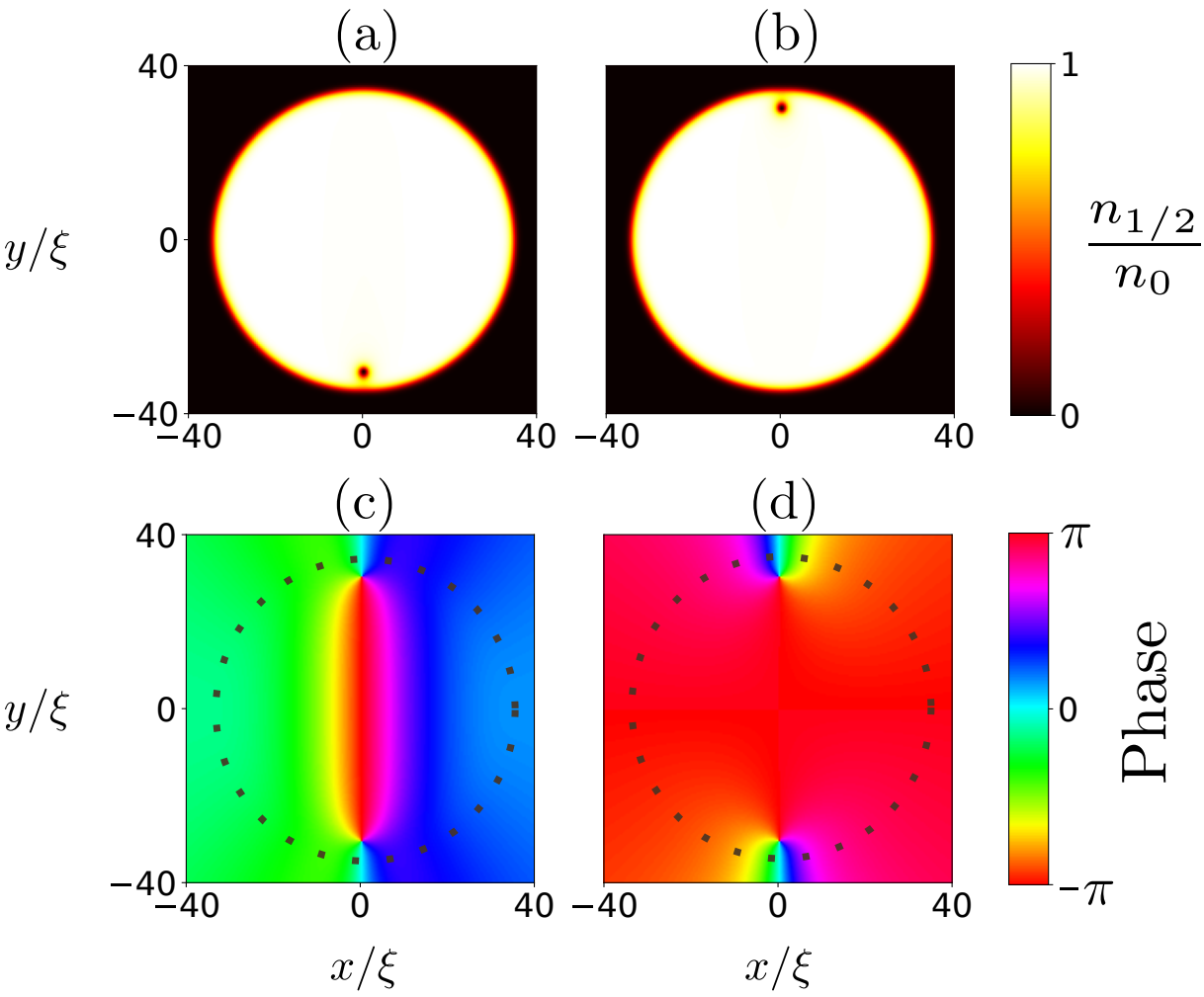

Figure 4.5: Numerical solution of the GPE with a centered vortex molecule with molecular length $d = 60\xi$. The component vortices are separated less than ξ_J from the trap boundaries and the assumption of a localized domain wall breaks down. (a) Density of condensate 1 $n_1 = |\psi_1|^2$. (b) Density of condensate 2 $n_2 = |\psi_2|^2$. (c) Relative phase $\arg(\psi_1\psi_2^*)$. (d) Total phase $\arg(\psi_1\psi_2)$. Parameters as in Fig. 4.1.

a localized region but rather differs from zero for most of the superfluid domain. Thus a crucial assumption of our model, i.e. the existence of a localized domain wall of the relative phase is violated for this case. The nonzero relative phase in the coupled BECs indicates that tunnel currents are present throughout the trap due to the Josephson-like relation between current and phase in linearly coupled Bose-Einstein condensates [79]. One of the consequences is that the continuity equation for each individual component, which underlies the point-vortex model, is now violated throughout the trap. The proximity of the component vortices to the trap boundary thus invalidated the assumptions of the distributed vorticity model and explains the discrepancies between the GPE data and model predictions for the precession frequencies seen in Fig. 4.4 for $d \gtrsim 40\xi$.

4.4.3 Off-centered vortex molecule

In addition to the centered vortex molecule, our models can also predict the trajectories of non-centered vortex molecules using the more general equation of motion (4.7) with details worked out in Appendix 4.8. Figure 4.6 shows the trajectory of one component vortex of a non-centered vortex molecule with $d = 16\xi$. The fact that trajectories do not overlap for the different models as seen in Fig. 4.6(a) indicates that the model predictions differ by more than just the precession frequency. Comparing the GPE trajectory with the model solution we find that the model combining a single vortex image with the linear assumption for the interaction energy (marked "sv+lin") not only severely overestimates the angular rotation frequency but also produces deviations from the correct trajectory. Figure 6(b) further visualizes the deviations of the point-vortex model from the GPE trajectory by plotting the instantaneous distance of vortex 1 between the point-vortex model and the GPE trajectory as a function of time. In comparison, the model based on distributed image vorticity combined with the parameterized interaction energy compares much more favorably to the GPE trajectories.

4.5 Conclusion

In conclusion, we have presented a distributed vorticity model for the dynamics of vortex molecules in a two-component Bose-Einstein condensate with linear coherent coupling. Our model extends previous work by considering a continuous distribution of image vorticity reflecting the effect of the domain wall on the vortex molecule phase structure. Specifically, the distributed vorticity model predicts a quadratic dependence for the image-induced contribution to the precession frequency on the length of the domain wall for small vortex molecules [Eq. (4.24)], while previous extended point vortex models predicted a constant angular frequency in the small molecule limit [Eq. (4.22)]. A second major finding is that assumption of a linear interaction energy made in Ref. [117] leads to an unphysical divergence in the precession frequency that is

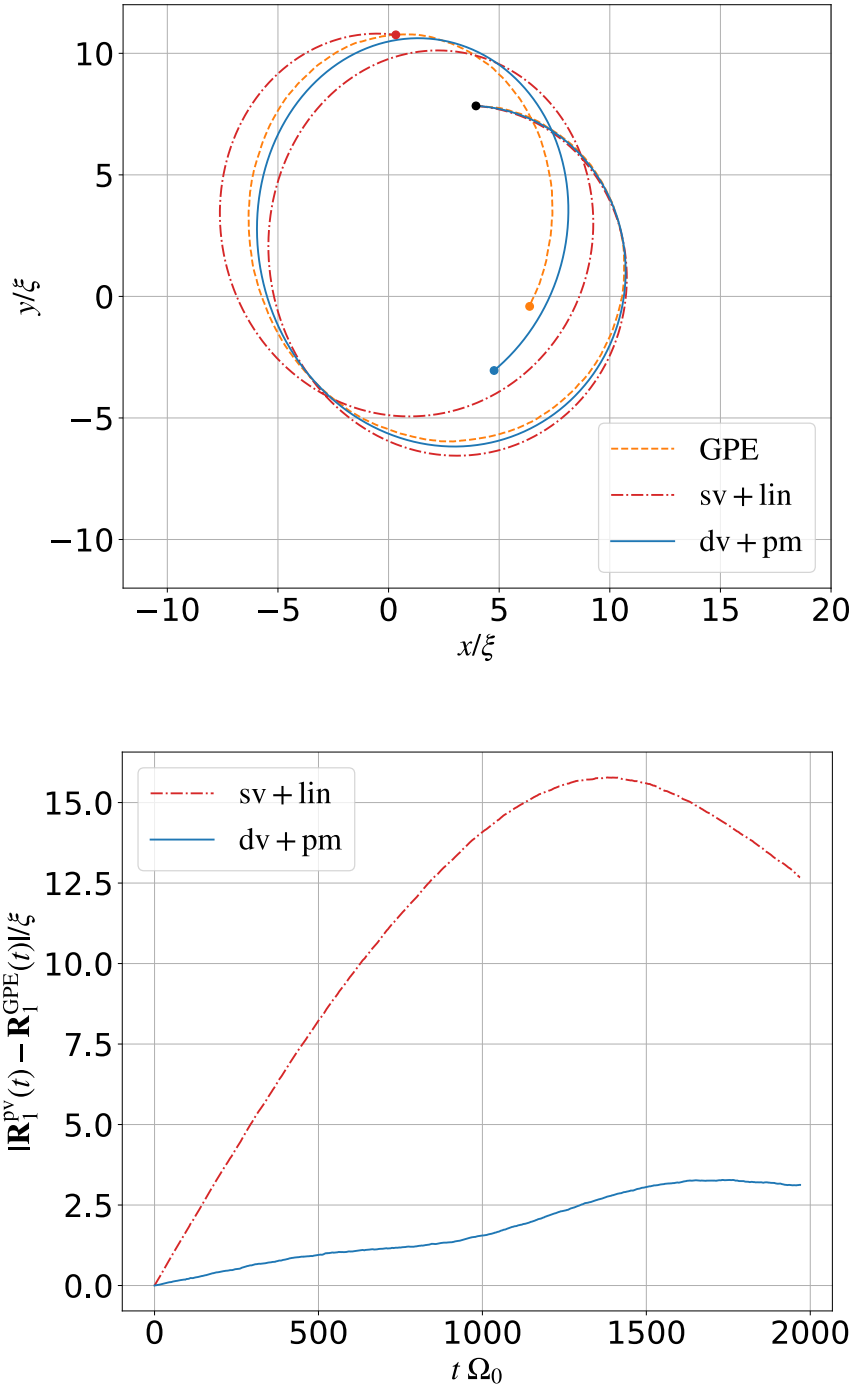

Figure 4.6: Trajectories predicted for an off-centered vortex molecule by different models, and their deviations. An off-centered vortex molecule moves in a disk-shaped trap ($L = 30\xi$) with initial positions $\mathbf{R}_1(t = 0) = (3.95\xi, 7.83\xi)$ (black dot in panel (a)), and $\mathbf{R}_2(t = 0) = (2.07\xi, -7.71\xi)$ (not shown). (a) Trajectories. The trajectory of vortex 1 is represented by colored lines showing the predictions from different models as in Fig. 4.4. The dashed line "GPE" denotes the numerical solution of the full Eq. (4.1). The dash-dotted line "sv+lin" shows the trajectory for the model with a single image vortex contribution of Eq. (4.22) combined with a linear interaction contribution based on Eq. (4.25). The full line "dv+pm" is obtained from combining the distributed vorticity contribution of Eq. (4.22) with the parameterized interaction contribution from Appendix 4.7. The colored dots mark the endpoints of the respective trajectories. (b) Deviations of the point vortex models from the GPE time evolution shown in panel (a). The instantaneous distance $|\mathbf{R}_1^{\mathrm{pv}}(t) - \mathbf{R}_1^{\mathrm{GPE}}(t)|$ between the location of vortex 1 according to the point vortex model and the GPE simulation is plotted as a function of time. Results are shown for the two point vortex models of panel (a) and labelled "sv+lin" and "dv+pm", respectively. The unit of time is $1/\Omega_0 = \hbar/(\mu + \nu)$.

inconsistent with the GPE data, while our model with the improved parametrization of the interaction energy avoids this unphysical divergence, and is consistent with the findings of Ref. [119]. We tested our model predictions over a range of molecule sizes against numerical simulations in a two-dimensional circular disc and found support for the improved model.

The main benefit of the distributed vorticity model compared to full GPE simulations is that it provides conceptual insights into the dynamics of vortex molecules. An extension to the dynamics of multiple vortex molecules and their interactions should be possible and can be expected to work well as long as the vortex molecules are well separated. This can be assured in a low-density and low-energy regime due to the linear-in-length energy content of the domain wall. Such a model could be useful for the study of quantum turbulence with a large number of vortex molecules in coupled BECs. Solving the coupled ordinary differential equations for the distributed vorticity model can be done with less computational effort than solving the full coupled GPEs. Moreover the absence of domain wall reconnections and vortex anniliation in the distributed vorticity model may provide key insights into the importance of such features for macroscopic observables when comparing the results to GPE simulations where all of this is included.

Our findings contribute to the ongoing research on the dynamics of superfluid vortices, which still poses many open questions. The peculiar structure of vortices in multi-component BECs, the competition between Rabi coupling and nonlinear mean-field energy, and the analogies to axions and quark confinement make this a rich and active area of research.

In this work we have specifically considered the case of vanishing cross-component nonlinearity in the GPE model, i.e. $g_{12} = 0$. In the more general case where $g_{12} > 0$ the cores of the component vortices are partly filled by local density maxima of the other component [117, 152]. This leads to a more complicated dynamics that could be modelled, at the point vortex level, by including inertial effects as in Refs. [141, 142]. Combining these ideas with the distributed vorticity model presented here could lead to a more accurate description of the dynamics of vortex molecules in a multi-component BEC with cross-component interactions.

4.6 Acknowledgements

S.C. acknowledges support by the Dodd-Walls Centre for Photonic and Quantum Technologies through a Dodd-Walls Centre PhD scholarship.

4.7 Appendix A: Interaction energy

The interaction energy is found as a function of molecular length d by creating a vortex molecule in a large computational domain of $180\xi \times 180\xi$ and using imaginary time evolution of the GPE in Eq. (4.1), i.e. replacing the time variable t by $-i\tau$, as described in Ref. [152]. The imaginary time evolution continually deforms the solution towards lower energy. While locally adjusting the correct density and gradients happens fairly quickly, on a slower time scale the position of the component vortices and thereby the molecular length d is altered. Under the assumption that the change in d happens while going through mininum energy configurations nearly adiabatically, we can extract the interaction energy $V(d)$ through a large range of values for d from a single simulation. Twisted real projective plane boundary conditions are applied as described in Ref. [152]. Here we detail the procedure to more accurately fit the interaction energy data than in [152], since small deviations in fitting result in large deviations of the derivative and hence in Fig. 4.4. We plot the raw data for the interaction energy $V(d)$ from imaginary time evolution (orange dots, only representative data point are shown) together with the parametrization used for the model dynamics. The parameterization is a composite using three different procedures.

The imaginary-time simulation was seeded with phase-imprinted component vortices at an initial distance of $d = 60\xi$ and then evolved to reduce the molecular distance d down to values much smaller than a healing length. We disregard data with $d > 55\xi$ where the domain wall is formed and imaginary-time evolution is not adiabatic. The raw data in the interval $3\xi < d < 55\xi$ is considered reliable, were we use a third order spline intepolation of the numerical data in order to obtain a continuous representation for $V(d)$. This is shown as a full blue line in Fig. 4.7. Since we expect the interaction energy to be linear at length scales much larger than $\xi_{\mathrm{J}} = 11.19\xi$, we perform a linear extrapolation for $d > 55\xi$ using the last three spline points. The linear extrapolation is shown as a dash-dotted green line.

The inset in Fig. 4.7 shows a closeup for small $d < 5\xi$. In this regime the imaginary-time evolution in τ decreased the molecular length d increasingly slowly while still reducing the energy, presumably by making subtle adjustments to the phase at large range. We thus consider the increasingly sharp drop of the energy near $d = 0$ in the imaginary time data an artefact. Instead we expect the true interaction energy to be an analytic function of the component vortex coordinates and an even function of d. Thus, it can be written as a power series in even powers of d. We thus extrapolate the interaction energy with a fourth order polynomial for $d < 4\xi$

$$V(d) = p_1 + p_2 d^2 + p_3 d^4. \tag{4.27}$$

The fitting parameters $p_1 = 33.35W_0$, $p_2 = 0.0239W_0/\xi^2$ and $p_3 = -0.000714W_0/\xi^4$ are obtained from a least-squares fit of the imaginary-time evolution data in the interval

$3\xi < d < 5\xi$. The quadratic extrapolation is shown as a dashed red line.

In our numerical simulations we have used dimensionless units where $1 = \tilde{\mu}+\tilde{\nu} = \tilde{\xi} = \tilde{g}+\tilde{g}_{12} = \tilde{n}_0$. The correct unit for the energy functional is thus $W_0 = \hbar^2(\mu+\nu)/m(g+g_{12}) = (\mu+\nu)^2\xi^2/(g+g_{12})$.

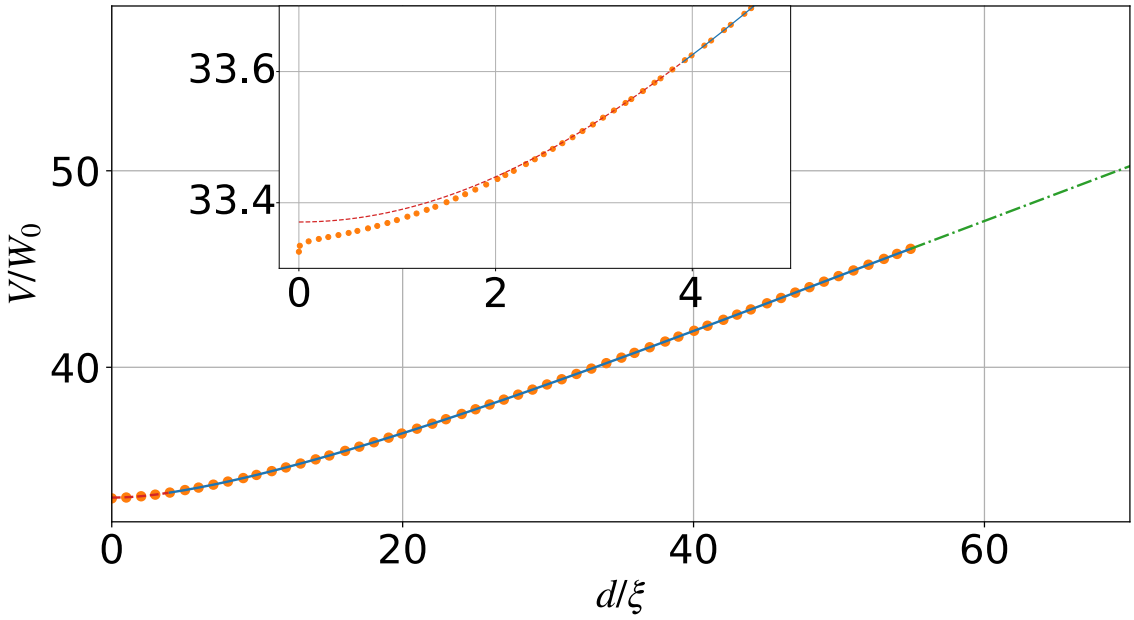

Figure 4.7: Fitting the interaction energy $V(d)$ as a function of molecular length d. The orange dots show data from imaginary time evolution of the GPE from Ref. [152] (only some representative data points are shown here). The inset is a closeup showing data for small values of d. The lines show the parameterization of $V(d)$ used for the model dynamics discussed in this chapter consisting of three different segments. The blue solid line shows a third order spline interpolation of the numerical data for $4\xi < d < 55\xi$. The green dot-dashed line is a linear extrapolation for large $d > 55\xi$. The red dashed line shows the quartic extrapolation of Eq. (4.27) for $d < 4\xi$. Parameters are $\nu = 2\times10^{-3}\mu$, $g_{12} = 0$. $W_0 = \hbar^2(\mu+\nu)/m(g+g_{12}) = (\mu+\nu)^2\xi^2/(g+g_{12})$ and an arbitrary offset was added to the energy.

4.8 Appendix B: General integrals of the charge distribution model

The velocity of the vortex at $\mathbf{R}_1$ in the distributed vorticity model in any arbitrary position of the vortex molecule is given by Eq. (4.16) as,

$$\mathbf{V}_1^{\mathrm{dv}}(R_1) = \kappa \int_0^1 \mathbf{u}_{\mathrm{im}}(\mathbf{R}_1; (1-t)\mathbf{R}_1 + t\mathbf{R}_2)\mathrm{d}t, \tag{4.28}$$

$$= \frac{\hbar\bar{\kappa}}{m}\hat{z} \times [\mathbf{R}_1 I_1 - \mathbf{R}_2 I_2]\,, \tag{4.29}$$

where I_1 and I_2 are

$$I_1 = \int_0^1 \frac{\left(1 - \frac{L^2}{R_i^2}\right) + t\frac{L^2}{R_i^2}}{|\mathbf{R_1}\left(1 - \frac{L^2}{R_i^2}\right) - \frac{L^2}{R_i^2}t\mathbf{d}|^2} dt, \tag{4.30}$$

$$I_2 = \int_0^1 \frac{\frac{L^2}{R_i^2}t}{|\mathbf{R_1}\left(1 - \frac{L^2}{R_i^2}\right) - \frac{L^2}{R_i^2}t\mathbf{d}|^2} dt, \tag{4.31}$$

with $\mathbf{d} = \mathbf{R}_2 - \mathbf{R}_1$ and $R_i^2 = |\mathbf{R}_1 + t\mathbf{d}|^2$. The scalar integrals come out as,

$$\begin{aligned} I_1 =& \frac{1}{dR_1^3}\left(dR_1 + L^2\left\{\left[\arctan(\cot\theta) - \right.\right.\right. \\ & \left.\arctan\left(\cot\theta + \frac{dR_1\,\mathrm{cosec}\,\theta}{R_1^2 - L^2}\right)\right]\cos 2\theta\,\mathrm{cosec}\,\theta \\ & \left.\left. + \cos\theta \ln\frac{d^2R_1^2 + (L^2 - R_1^2)^2 + 2dR_1(R_1^2 - L^2)\cos\theta}{(L^2 - R_1^2)^2}\right\}\right), \end{aligned} \tag{4.32}$$

$$\begin{aligned} I_2 =& \frac{R^2}{2d^2R_1^2}\left\{2\left[\arctan(\cot\theta) - \arctan\left(\cot\theta\right.\right.\right. \\ & \left.\left.\left. + \frac{dR_1\,\mathrm{cosec}\,\theta}{-L^2 + R_1^2}\right)\right]\cot\theta \right. \\ & \left. + \ln\frac{d^2R_1^2 + (L^2 - R_1^2)^2 + 2dR_1(R_1^2 - L^2)\cos\theta}{(L^2 - R_1^2)^2}\right\} \end{aligned} \tag{4.33}$$

with θ being the angle between $\mathbf{R}_1$ and $\mathbf{d}$. I_1 has a removable singularity at $\theta = 0$.

MASSEY UNIVERSITY
GRADUATE RESEARCH SCHOOL

STATEMENT OF CONTRIBUTION
DOCTORATE WITH PUBLICATIONS/MANUSCRIPTS

We, the candidate and the candidate's Primary Supervisor, certify that all co-authors have consented to their work being included in the thesis and they have accepted the candidate's contribution as indicated below in the *Statement of Originality*.

Name of candidate:	Sarthak Choudhury
Name/title of Primary Supervisor:	Joachim Brand
Name of Research Output and full reference:	
Sarthak Choudhury and Joachim Brand, "Distributed vorticity model for vortex molecule dynamics", arXiv:2212.07131	
In which Chapter is the Manuscript /Published work:	Chapter 4
Please indicate:	
• The percentage of the manuscript/Published Work that was contributed by the candidate:	80
and	
• Describe the contribution that the candidate has made to the Manuscript/Published Work:	
Original draft preparation; manuscript review and editing; data curation and analysis; data visualizaton; implementation of code based on preliminary code by supervisor and relevant data generation; derivation of relevant equations.	
For manuscripts intended for publication please indicate target journal:	
Physical Review A	
Candidate's Signature:	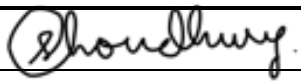
Date:	16/12/2022
Primary Supervisor's Signature:	
Date:	16/12/2022

(This form should appear at the end of each thesis chapter/section/appendix submitted as a manuscript/ publication or collected as an appendix at the end of the thesis)

Chapter 5

Vortices in annular rings and ring currents

In this chapter we depart from coupled condensates and focus on a single condensate in a ring geometry. Persistent supercurrents in a ring geometry, which we refer to as 'ring' currents from now on, are a topological excitation that can be used in components of atomtronics. Atomtronics is the use of atomic systems as transistors and diodes analogous to components of electronic or optical systems [156]. These can be used to construct matter-wave circuits of ultracold atoms [157, 158] and atomtronic analogues of SQUIDs (superconducting quantum interference devices) [159–163]. Cold-atom systems have also been used to implement qubits or quantum bits, which are the basic unit of quantum information in quantum computing The main idea is to use the supercurrents of cold-atom systems flowing in ring-shaped potential traps. [164–166].

The circulation of the order parameter in a ring current is marked by a rotation of multiples of $2\pi\frac{\hbar\kappa}{m}$ around the ring. This is exactly the same for a vortex which is located at the center of a ring. Persistent supercurrents have been experimentally created by different methods most notably imposing an external phase gradient on the ring [167], using a laser to create a repulsive potential to physically 'stir' the condensate around the ring [168–170], or using a laser to create a Raman transition of the atoms to a rotating state [159].

5.1 Protocol for creating ring currents

Kanamoto *et. al.* in [171, 172] showed topological states in a one-dimensional condensate in a toroidal trap could be manipulated by changing the frequency of rotation of the condensate. Continuous transitions can occur via metastable dark soliton states that exist between stable ring current states by changing the rotation of the system. This transition falls under quantum phase transition and is the basis on which the protocol in [173] is based upon. The angular momentum operator as introduced in Section 2.5 is

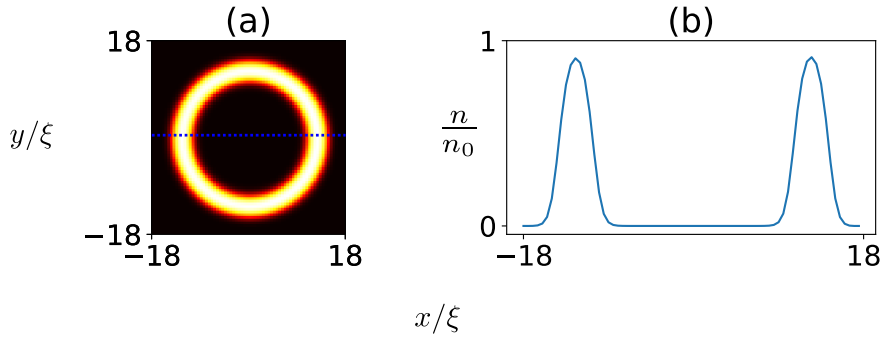

Figure 5.1: Density $n = |\psi|^2$ of a condensate in an annular ring geometry. This is the lowest energy solution found by imaginary time evolution of Eq. (5.2) with $\epsilon = 0$, $L_2 = 15\xi$ and $L_1 = 10\xi$. (b) is a transverse cut along the blue dotted line in (a). The background density is given by $n_0 = \mu/g$, $g = \mu\xi^2$ and ξ is the healing length.

defined as $\hat{L}_z = -i\hbar\partial/\partial\theta$, where θ is the polar coordinate with the center of the rings as the origin. Focusing only on the ring current states, if we express the condensate order parameter in the ring as $\psi(\mathbf{r}) = n(r)e^{iS_v}$ where $S_v = i\kappa\theta$ and κ is the charge of the vortex or ring current. This state is an eigenstate of the angular momentum operator and the eigenvalue equation can be expressed as

$$\hat{L}_z\psi = \kappa\hbar\psi. \tag{5.1}$$

Non-zero integer values of κ correspond to ring current states which are topological in nature. The aim is to introduce an adiabatic crossover of the condensate from the $\kappa = 0$ state with no ring current to the $\kappa = 1$ rotating state by nucleating a vortex. The authors of [173] have provided a protocol through which supercurrent can be induced from the ground state using a time dependent rotating potential. The global symmetry of the system is broken by the rotating potential adiabatically, by tilting the trap axis by a small angle. The rotational frequency of the potential is decreased to a final value after which the tilt is decreased. This creates an adiabatic passage of the system through a metastable dark soliton state. This passage is initiated by the nucleation of a vortex which moves through the ring radially inward into the center at zero density, thereby moving the system to a $\kappa = 1$ ring current state. The motion of the vortex towards the center of the rings is induced by slowing down the rotation of the external potential. In [173] the seeded dark soliton remains at the minimum of the potential or the maximum of the condensate density as it moves radially inward into the ring. We aim to use the same protocol for the two-dimensional condensate in a narrow ring.

5.2 Mean Field Formulation

The condensate is contained within a ring potential the time evolution of which similar to Eq. (2.1), is given by

$$i\hbar\frac{d\psi}{dt} = \left\{-\frac{\hbar^2}{2m}\nabla^2 + V(\mathbf{r}) - \mu + \epsilon(t)\cos\left[\theta - \omega_r(t)t\right]\right\}\psi + g\left|\psi\right|^2\psi, \tag{5.2}$$

where ϵ is the amplitude of the rotating symmetry breaking potential, $\theta = \arctan(y/x)$ and ω_r is the rotating frequency of the potential. The external ring shaped potential is given by

$$V(\mathbf{r}) = \mu\left(\tanh\frac{r - L_2}{\xi} - \tanh\frac{r - L_1}{\xi} + 2\right), \tag{5.3}$$

where L_1 is radius of the inner ring, L_2 is radius of the outer ring, $r = |\mathbf{r}|$ and $\xi = \hbar/\sqrt{m\mu}$ is the healing length. For the remaining discussion we take $L_1 = 10$ and $L_2 = 15$. The trivial background solution putting $V(\mathbf{r}) = 0$ and $\epsilon(t) = 0$ is given by $n_0 = |\psi_0|^2 = \mu/g$. This also represents the bulk density to which the condensate heals back to from the boundaries or the vortex core.

Following the protocol in [173], ϵ and ω_r both change in time. The potential amplitude $\epsilon(t)$ is given by

$$\epsilon(t) = \frac{\epsilon_0}{2}\{\tanh[\alpha(t - t_1)] - \tanh[\alpha(t - t_2)]\}, \tag{5.4}$$

where ϵ_0 is the maximum value of the potential, t_1 and t_2 are the times in which the change in the potential is the largest and α gives a measure of the slope of the increase of the potential. Fig. 5.4 (a) describes ϵ as a function of time. The potential frequency ω_r is given by

$$\omega_r(t) = \begin{cases}\omega_0 & t < t_1,\\ \omega_0[1 - \beta(t - t_1)] & t > t_1,\end{cases} \tag{5.5}$$

where t_1 is the time point in which the angular frequency of the rotating trap starts decreasing as seen in Fig. 5.4 (b). We choose ω_0 such that tangential velocity at the outer ring before t_1 is equal to the speed of sound i.e. $\omega_0 = cL_2$ where $c = \sqrt{ng/m}$ is the speed of sound.

5.3 Ring currents and solitonic vortex

The ground state is prepared in the numerical simulation by putting $\epsilon = 0$ and then imaginary time evolving from a constant density initial state according to Eq. (5.2). The density $n = |\psi|^2$ of this ground state is given in Fig. 5.1. This is a state with zero angular momentum and no ring current.

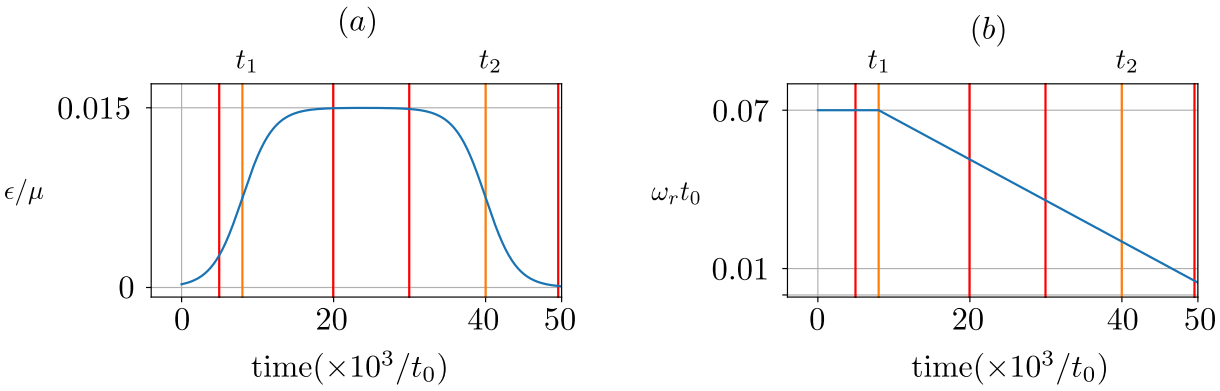

Figure 5.2: The external potential amplitude ϵ and angular frequency ω_r as a function of time. The orange vertical lines are $t_1 = 8000t_0$ and $t_2 = 40000t_0$ where $t_0 = \hbar/\mu$. The red vertical lines signify the different times in which snapshots of the density and phase are taken in Fig. 5.3 and Fig. 5.4, respectively. Other parameters are $\epsilon_0 = 0.015\mu$, $\omega_0 t_0 = 0.07$, $\alpha t_0 = 0.00025$, $\beta t_0 = 2.22 \times 10^{-5}$.

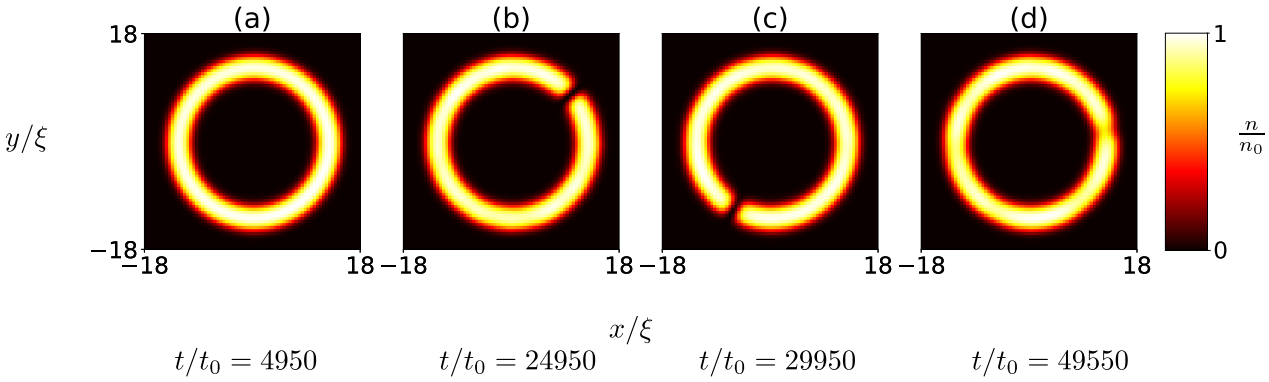

Figure 5.3: Density $n = |\psi|^2$ of a condensate in an annular ring geometry at different times. An external potential given by $\epsilon(t)$ in Eq. (5.4) is turned on at $t_1/t_0 = 8000$ and turned off at $t_2/t_0 = 40000$. The system begins with no rotation as seen in (a). The external potential breaks the symmetry and a vortex enters the ring-shaped condensate as seen by the region of zero density in the ring in (b). (c) shows the same vortex rotating in the ring creating a solitonic vortex state. (d) shows the system at the end of the protocol where even though there are no vortices as shown in the density but the phase seems to go around the ring in 2π as seen in subplot (d) in Fig. 5.4. into a state with a supercurrent. The interatomic interaction $g = \mu\xi^2$ and $t_0 = \hbar/\mu$ is a dimensional factor.

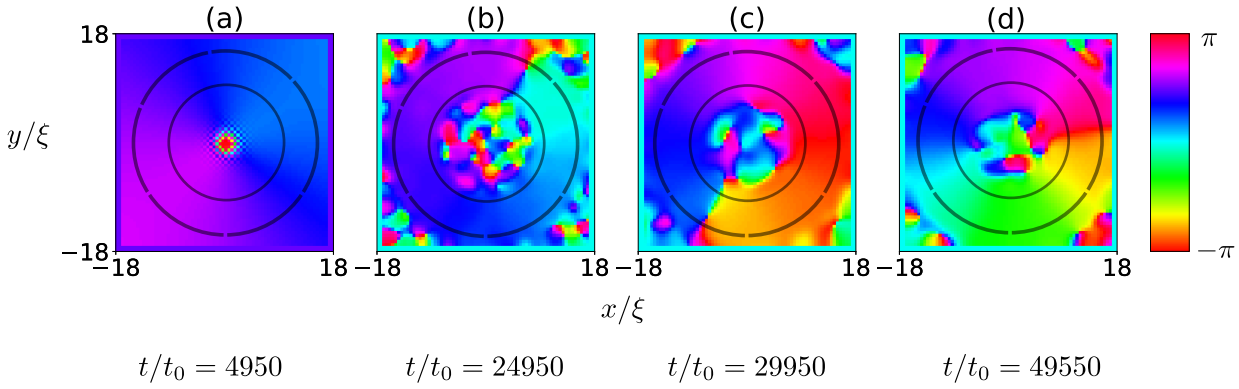

Figure 5.4: The phase $\arg(\psi)$ of a condensate in an annular ring geometry at the same times as Fig. 5.3. The vortices are clearly seen in (b) and (c) as points around which, the phase goes around by 2π. This corresponds to the same region in (c) and (d) of Fig. 5.3 of zero density. The ring current is illustrated in (d) by the phase, which changes by 2π as one traverses around the circular ring even though there are no vortices in the condensate. All parameters are same as Fig. 5.3.

The protocol is started by ramping up the time-dependent cosine-shaped external potential which is illustrated in Fig. 5.2. As the condensate experiences the maximum change at t_1, ω_r starts decreasing by a constant rate. As the system responds to this change, a vortex enters into the ring from the outer wall. The vortex rotates around the ring while moving closer radially and exits the condensate through the inner wall after which the external potential is ramped down at t_2. Even when the potential is ramped down to zero a steady ring current is observed in subplot (d) of Fig. 5.4 given by the rotation of the phase by 2π around the ring. Different stages of the protocol are shown via different snapshots of the density and phase of the system in Fig. 5.3 and Fig. 5.4, respectively which also correspond to the red vertical lines of Fig. 5.2.

Our system being two-dimensional creates distinct differences from the ring current generation in the idealized one-dimensional case. In [173] the dark soliton enters the minimum of the external potential and adiabatically moves into the inner ring always remaining in the minima. In our case though, the vortex does not enter at the minima, nor does it stay there throughout the protocol. This creates a ring current albeit non-adiabatically but through solitonic vortices in a ring as in [124].

The total time taken for the entire protocol is $t_p = 50\times10^3\ t_0$ as shown in Fig. 5.2, where $t_0 = \hbar/\mu$ is the dimensional unit. The authors of [174] have used a Bose-Einstein condensate of ^{23}Na atoms using a toroidal trap and Raman transitions to generate supercurrents. We use their experimental parameters to make a estimation of the time taken for our protocol. The experimental trap height determines the energy scale $\mu/\hbar = 0.5 \times 2\pi$ kHz. Our protocol would take about $t_p \approx 1.6s$ to generate ring currents which is still significantly less than the time ring currents were observed in the experiment (10s).

The experimental inner trap radius is $50\xi \approx 10\mu m$ which is 10 times the trap size

we have used. Increasing the trap size to 100 ξ in our protocol would only change ω_0 in Eq. (5.5) which is dependent on the radius of the outer ring.

5.4 Summary

We numerically show the possibility of creating ring currents in two-dimensional ring-shaped condensates using a protocol already used to create persistent currents in the idealized one dimensional case. We use a cosine shaped time dependent potential which decreases in angular frequency thereby seeding a vortex in the outer wall which ultimately moves to the center of the rings. This creates a ring current throughout the condensate which persists even when the potential is removed. We compare with experimental parameters and find that the whole protocol takes a fraction of the time in which ring currents were observed in the experiment.

Chapter 6

Conclusion and future outlook

Predicting BEC vortex dynamics in different trap geometries has been always a challenging problem. But the first step is to explore the dynamics in traps which have some symmetry that can be exploited to come up with simpler point-vortex models. We aim to shed some light on vortex molecule dynamics which consists of two vortices bound by a domain wall in between and is a more complicated problem. In this thesis we use two different traps to test an extended point vortex model and a distributed vorticity model which aims to simplify this complex dynamics into simpler ordinary differential equations.

The extended point vortex model captures all the phase space characteristics including saddle points (hyperbolic fixed points), associated separatrices and elliptical fixed points of a vortex molecule in a channel. It also predicts intriguing pendulum like trajectories for non-zero interatomic interaction which agree with GPE simulations. Both the GPE and the model predicts trajectories in which the vortex molecule stretches apart. These trajectories might inspire future experimental setups to create vortex molecules in channel traps. Just by choosing an appropriate initial position of the vortex molecule with reference to the channel, one might observe a vortex molecule stretch from a stable initial length to a critical length where it breaks up creating a new vortex molecule and vortex-antivortex pair confined to one condensate. This produces an ideal scenario for the laboratory analogue to the color confinement in quantum chromodynamics.

To fully understand the dynamics of a vortex molecule in a flat-bottomed isotropic disc we propose a new vorticity model. Instead of treating the component vortices as point vortices, we consider the vorticity to be distributed along the domain wall connecting the component vortices. We use this model to predict the precession frequency of a centered vortex molecule. We compare predictions from this model with previous models from literature and GPE simulations and find good support. It would be further interesting to see this model implemented for other trap geometries and see similar agreement to the GPE results.

Lastly, we numerically investigate the creation of ring currents in two-dimensional

ring-shaped condensates. Though this has been already done we use a protocol which has been described before to create persistent currents in an ideal one dimensional ring for a two-dimensional ring condensate. We use a cosine shaped time dependent potential which seeds a vortex in the outer wall which ultimately moves to the center of the rings, thereby creating a ring current. Though the protocol creates ring currents in the one dimensional ring adiabatically, we see ring currents appear in the two-dimensional condensate even non-adiabatically. This calls for further study into the pathway through which this non-adiabatic process occurs since the nucleated vortex does not stay at the minimum of the time dependent potential as in the idealized one-dimensional case. This could also provide an alternative way to create persistent ring currents experimentally.

Bibliography

[1] Bose, Zeitschrift für Physik **26**, 178 (1924).

[2] A. Einstein, "Quantentheorie des einatomigen idealen gases. zweite abhandlung," in *Albert Einstein: Akademie-Vorträge* (John Wiley and Sons, Ltd, 2005) pp. 245–257, https://onlinelibrary.wiley.com/doi/pdf/10.1002/3527608958.ch28 .

[3] P. Kapitza, Nature **141**, 74 (1938).

[4] J. F. Allen and A. D. Misener, Nature **141**, 75 (1938).

[5] P. Das, R. B. de Ouboter, and K. W. Taconis, in *Low Temperature Physics LT9*, edited by J. G. Daunt, D. O. Edwards, F. J. Milford, and M. Yaqub (Springer US, Boston, MA, 1965) pp. 1253–1255.

[6] D. J. Wineland, R. E. Drullinger, and F. L. Walls, Phys. Rev. Lett. **40**, 1639 (1978).

[7] E. L. Raab, M. Prentiss, A. Cable, S. Chu, and D. E. Pritchard, Phys. Rev. Lett. **59**, 2631 (1987).

[8] M. H. Anderson, J. R. Ensher, M. R. Matthews, C. E. Wieman, and E. A. Cornell, Science **269**, 198 (1995), http://science.sciencemag.org/content/269/5221/198.full.pdf .

[9] Y.-J. Lin, R. L. Compton, K. Jiménez-García, W. D. Phillips, J. V. Porto, and I. B. Spielman, Nature Physics **7**, 531 (2011).

[10] H. C. Po and Q. Zhou, Nature Communications **6**, 8012 (2015).

[11] N. T. Phuc, Y. Kawaguchi, and M. Ueda, Phys. Rev. Lett. **113**, 230401 (2014).

[12] T. Bravo, C. Sabín, and I. Fuentes, EPJ Quantum Technology **2**, 3 (2015).

[13] S. Eckel, A. Kumar, T. Jacobson, I. B. Spielman, and G. K. Campbell, Phys. Rev. X **8**, 021021 (2018).

[14] O. Fialko, B. Opanchuk, A. I. Sidorov, P. D. Drummond, and J. Brand, EPL Europhys. Lett. **110**, 56001 (2015), arXiv:1408.1163v2 .

[15] J. Braden, M. C. Johnson, H. V. Peiris, A. Pontzen, and S. Weinfurtner, Journal of High Energy Physics **2019**, 174 (2019).

[16] K. E. Strecker, G. B. Partridge, A. G. Truscott, and R. G. Hulet, Nature **417**, 150 (2002).

[17] A. I. Streltsov, O. E. Alon, and L. S. Cederbaum, Phys. Rev. Lett. **106**, 240401 (2011).

[18] A. Sreedharan, S. Choudhury, R. Mukherjee, A. Streltsov, and S. Wüster, Phys. Rev. A **101**, 043604 (2020).

[19] A. Sreedharan, S. Kuriyattil, S. Choudhury, R. Mukherjee, A. Streltsov, and S. Wuester, Europhysics Letters (2022).

[20] J. C. Smith, D. Baillie, and P. B. Blakie, Phys. Rev. Lett. **126**, 025302 (2021).

[21] C. R. Cabrera, L. Tanzi, J. Sanz, B. Naylor, P. Thomas, P. Cheiney, and L. Tarruell, Science **359**, 301 (2018), https://www.science.org/doi/pdf/10.1126/science.aao5686 .

[22] S. Burger, K. Bongs, S. Dettmer, W. Ertmer, K. Sengstock, A. Sanpera, G. V. Shlyapnikov, and M. Lewenstein, Phys. Rev. Lett. **83**, 5198 (1999).

[23] H. T. C. Stoof, E. Vliegen, and U. Al Khawaja, Phys. Rev. Lett. **87**, 120407 (2001).

[24] T.-L. Ho, Phys. Rev. Lett. **81**, 742 (1998).

[25] J. Ruostekoski and J. R. Anglin, Phys. Rev. Lett. **86**, 3934 (2001).

[26] M. A. Metlitski and A. R. Zhitnitsky, Journal of High Energy Physics **2004**, 017 (2004).

[27] Y. Kawaguchi, M. Nitta, and M. Ueda, Phys. Rev. Lett. **100**, 180403 (2008).

[28] N. D. Mermin, Rev. Mod. Phys. **51**, 591 (1979).

[29] M. R. Matthews, B. P. Anderson, P. C. Haljan, D. S. Hall, C. E. Wieman, and E. A. Cornell, Phys. Rev. Lett. **83**, 2498 (1999).

[30] S. Hofferberth, I. Lesanovsky, B. Fischer, T. Schumm, and J. Schmiedmayer, Nature **449**, 324 (2007).

[31] T. Betz, S. Manz, R. Bücker, T. Berrada, C. Koller, G. Kazakov, I. E. Mazets, H.-P. Stimming, A. Perrin, T. Schumm, and J. Schmiedmayer, Phys. Rev. Lett. **106**, 020407 (2011).

[32] E. Nicklas, H. Strobel, T. Zibold, C. Gross, B. A. Malomed, P. G. Kevrekidis, and M. K. Oberthaler, Phys. Rev. Lett. **107**, 193001 (2011).

[33] E. Nicklas, W. Muessel, H. Strobel, P. G. Kevrekidis, and M. K. Oberthaler, Phys. Rev. A **92**, 053614 (2015).

[34] A. Barone and G. Paternò, *Physics and Applications of the Josephson Effect* (Wiley, New York, 1982).

[35] T. Schweigler, V. Kasper, S. Erne, I. Mazets, B. Rauer, F. Cataldini, T. Langen, T. Gasenzer, J. Berges, and J. Schmiedmayer, Nature **545**, 323 (2017).

[36] M. Eto and M. Nitta, Phys. Rev. A **97**, 023613 (2018).

[37] S. Yasui and M. Nitta, Phys. Rev. C **101**, 015207 (2020).

[38] M. Kobayashi and M. Nitta, "Proximity effects of vortices in neutron $^3p_2$ superfluids in neutron stars: Vortex core transitions and covalent bonding of vortex molecules," (2022).

[39] D. J. Griffiths, *Introduction to Quantum Mechanics* (Cambridge University Press, 1994).

[40] L. Pollet, Reports on Progress in Physics **75**, 094501 (2012).

[41] L. A. Toikka, , 1 (2017), arXiv:1711.04970 .

[42] C. J. Pethick and H. Smith, *Bose-Einstein Condensation in Dilute Gases* (Cambridge University Press, Cambridge, UK, 2008).

[43] L. Pitaevskii and S. Stringari, *Bose-Einstein Condensation* (Clarendon, Oxford, 2003).

[44] E. H. Lieb, R. Seiringer, and J. Yngvason, Phys. Rev. A **61**, 043602 (2000).

[45] A. L. Fetter, Phys. Rev. **138**, A429 (1965).

[46] D. S. Rokhsar, Phys. Rev. Lett. **79**, 2164 (1997).

[47] K. W. Madison, F. Chevy, W. Wohlleben, and J. Dalibard, Phys. Rev. Lett. **84**, 806 (2000).

[48] B. P. Anderson, P. C. Haljan, C. E. Wieman, and E. A. Cornell, Phys. Rev. Lett. **85**, 2857 (2000), arXiv:cond-mat/0005368 .

[49] S. A. McGee and M. J. Holland, Phys. Rev. A **63**, 043608 (2001).

[50] A. Fetter, Rev. Mod. Phys. **81**, 647 (2009).

[51] R. J. Donnelly, *Quantized Vortices in Helium II* (Cambridge University Press, 1991).

[52] J.-M. Duan and A. J. Leggett, Phys. Rev. Lett. **68**, 1216 (1992).

[53] Duan, Phys. Rev. B Condens. Matter **49**, 12381 (1994).

[54] G. Baym and E. Chandler, J. Low Temp. Phys. **50**, 57 (1983).

[55] T. Simula, Phys. Rev. A **97**, 023609 (2018).

[56] L. D. Landau and E. M. Lifshitz, *Mechanics* (Butterworth-Heinemann, 1976).

[57] S. Sinha and Y. Castin, Phys. Rev. Lett. **87**, 190402 (2001).

[58] S. Sinha and Y. Castin, *Laser Spectroscopy*, pp. 61–69.

[59] P. G. Saffman, *Vortex Dynamics* (Cambridge University Press, Cambridge, 1995).

[60] P. K. Newton, *The N-Vortex Problem*, Vol. 145 (Springer New York, New York, NY, 2001) arXiv:1011.1669v3 .

[61] G. B. Arfken, H. J. Weber, and F. E. Harris, in *Mathematical Methods for Physicists (Seventh Edition)*, edited by G. B. Arfken, H. J. Weber, and F. E. Harris (Academic Press, Boston, 2013) seventh edition ed., pp. 447–467.

[62] H. Goldstein, *Classical Mechanics* (Addison-Wesley, 1980).

[63] C. C. Lin, Proc. Natl. Acad. Sci. **27**, 570 (1941).

[64] C. C. Lin, Proc. Natl. Acad. Sci. **27**, 575 (1941).

[65] A. L. Fetter, Phys. Rev. **162**, 143 (1967).

[66] F. D. M. Haldane and Y.-S. Wu, Phys. Rev. Lett. **55**, 2887 (1985).

[67] J. D. Jackson, *Classical Electrodynamics*, 3rd ed. (Wiley, New York, NY, 1999).

[68] J. R. Anglin, Phys. Rev. A **65**, 063611 (2002), arXiv:cond-mat/0110389 .

[69] U. A. Khawaja, Phys. Rev. A **71**, 063611 (2005).

[70] P. Mason, N. G. Berloff, and A. L. Fetter, Phys. Rev. A **74**, 043611 (2006), arXiv:cond-mat/0605648 .

[71] A. Recati and S. Stringari, Annual Review of Condensed Matter Physics **13**, 407 (2022), https://doi.org/10.1146/annurev-conmatphys-031820-121316 .

[72] A. Farolfi, A. Zenesini, R. Cominotti, D. Trypogeorgos, A. Recati, G. Lamporesi, and G. Ferrari, Phys. Rev. A **104**, 023326 (2021), arXiv:2101.12643 .

[73] R. Cominotti, A. Berti, C. Dulin, C. Rogora, G. Lamporesi, I. Carusotto, A. Recati, A. Zenesini, and G. Ferrari, "Revealing the ferromagnetic phase transition in an extended two-component atomic superfluid," (2022).

[74] M. Abad and A. Recati, Eur. Phys. J. D **67**, 148 (2013).

[75] V. M. Pérez-García and J. J. García-Ripoll, Phys. Rev. A **62**, 033601 (2000).

[76] D. M. Jezek, P. Capuzzi, and H. M. Cataldo, Phys. Rev. A **64**, 023605 (2001).

[77] S. T. Chui, V. N. Ryzhov, and E. E. Tareyeva, Phys. Rev. A **63**, 023605 (2001).

[78] A. Gallemí, L. P. Pitaevskii, S. Stringari, and A. Recati, Phys. Rev. A **97**, 063615 (2018).

[79] A. Smerzi, S. Fantoni, S. Giovanazzi, and S. R. Shenoy, Phys. Rev. Lett. **79**, 4950 (1997).

[80] I. Marino, S. Raghavan, S. Fantoni, S. R. Shenoy, and A. Smerzi, Phys. Rev. A **60**, 487 (1999).

[81] S. Raghavan, A. Smerzi, S. Fantoni, and S. R. Shenoy, Phys. Rev. A **59**, 620 (1999).

[82] J. Bardeen and M. J. Stephen, Phys. Rev. **140**, A1197 (1965).

[83] G. Blatter, M. V. Feigel'man, V. B. Geshkenbein, A. I. Larkin, and V. M. Vinokur, Rev. Mod. Phys. **66**, 1125 (1994).

[84] A. Tonomura, H. Kasai, O. Kamimura, T. Matsuda, K. Harada, J. Shimoyama, K. Kishio, and K. Kitazawa, Nature **397**, 308 (1999).

[85] R. Fazio and H. van der Zant, Physics Reports **355**, 235 (2001).

[86] V. L. Ginzburg, ChemPhysChem **5**, 930 (2004), https://chemistry-europe.onlinelibrary.wiley.com/doi/pdf/10.1002/cphc.200400182 .

[87] D. T. Son and M. A. Stephanov, Phys. Rev. A **65**, 063621 (2002).

[88] S. S. Shamailov and J. Brand, SciPost Phys. **4**, 018 (2018), arXiv:1709.00403 .

[89] V. M. Kaurov and A. B. Kuklov, Phys. Rev. A **71**, 011601(R) (2005).

[90] V. M. Kaurov and A. B. Kuklov, Phys. Rev. A **73**, 013627 (2006).

[91] T. Tsuzuki, J. Low Temp. Phys. **4**, 441 (1971).

[92] C. Becker, S. Stellmer, P. Soltan-Panahi, S. Dörscher, M. Baumert, E.-M. Richter, J. Kronjäger, K. Bongs, and K. Sengstock, Nat. Phys. **4**, 496 (2008).

[93] J. Denschlag, J. E. Simsarian, D. L. Feder, C. W. Clark, L. A. Collins, J. Cubizolles, L. Deng, E. W. Hagley, K. Helmerson, W. P. Reinhardt, S. L. Rolston, B. I. Schneider, and W. D. Phillips, Science **287**, 97 (2000).

[94] M. Eto and M. Nitta, Phys. Rev. A **85**, 053645 (2012).

[95] C. Baals, H. Ott, J. Brand, and A. M. n. Mateo, Phys. Rev. A **98**, 053603 (2018).

[96] E. Mueller and T.-L. Ho, Phys. Rev. Lett. **88**, 1 (2002).

[97] K. Kasamatsu, M. Tsubota, and M. Ueda, Phys. Rev. Lett. **91**, 150406 (2003).

[98] A. Aftalion, P. Mason, and J. Wei, Phys. Rev. A **85**, 033614 (2012).

[99] D. S. Dantas, A. R. P. Lima, A. Chaves, C. A. S. Almeida, G. A. Farias, and M. V. Milošević, Phys. Rev. A **91**, 023630 (2015).

[100] K. Kasamatsu, M. Tsubota, and M. Ueda, International Journal of Modern Physics B **19**, 1835 (2005).

[101] Y. Masaki, T. Mizushima, and M. Nitta, Phys. Rev. B **105**, L220503 (2022).

[102] M. Kobayashi, M. Eto, and M. Nitta, Phys. Rev. Lett. **123**, 075303 (2019).

[103] K. Kasamatsu, M. Tsubota, and M. Ueda, Phys. Rev. Lett. **93**, 250406 (2004).

[104] Y. Castin and R. Dum, The European Physical Journal D - Atomic, Molecular, Optical and Plasma Physics **7**, 399 (1999).

[105] A. Abrikosov, Sov. Phys. JETP **5**, 1174 (1957).

[106] B. S. Deaver and W. M. Fairbank, Phys. Rev. Lett. **7**, 43 (1961).

[107] B. Mencia Uranga and A. Lamacraft, Physical Review A **97**, 043609 (2018), publisher: American Physical Society.

[108] W.-C. Yang, C.-Y. Xia, M. Nitta, and H.-B. Zeng, Phys. Rev. D **102**, 046012 (2020).

[109] M. Cipriani and M. Nitta, Phys. Rev. Lett. **111**, 170401 (2013).

[110] A. Aftalion and P. Mason, Phys. Rev. A **94**, 023616 (2016).

[111] C. Tsitouras, Computers and Mathematics with Applications **62**, 770 (2011).

[112] D. Thouless, *Topological Quantum Numbers In Nonrelativistic Physics* (World Scientific, 1998).

[113] N. Manton and P. Sutcliffe, *Topological Solitons* (Cambridge University Press, Cambridge, 2004).

[114] J. J. García-Ripoll, V. M. Pérez-García, and F. Sols, Phys. Rev. A **66**, 021602(R) (2002).

[115] A. Farolfi, A. Zenesini, D. Trypogeorgos, C. Mordini, A. Gallemí, A. Roy, A. Recati, G. Lamporesi, and G. Ferrari, Nat. Phys. (2021), 10.1038/s41567-021-01369-y.

[116] M. Eto, K. Ikeno, and M. Nitta, Phys. Rev. Research **2**, 033373 (2020).

[117] M. Tylutki, L. P. Pitaevskii, A. Recati, and S. Stringari, Phys. Rev. A **93**, 043623 (2016).

[118] K. Kasamatsu, M. Eto, and M. Nitta, Phys. Rev. A **93**, 013615 (2016).

[119] L. Calderaro, A. L. Fetter, P. Massignan, and P. Wittek, Phys. Rev. A **95**, 023605 (2017).

[120] W. Ketterle and M. W. Zwierlein, Riv. Nuovo Cimento **31**, 247 (2008), arXiv:0801.2500 .

[121] C. Becker, K. Sengstock, P. Schmelcher, P. G. Kevrekidis, and R. Carretero-González, New J. Phys. **15**, 113028 (2013), arXiv:1308.2994 .

[122] A. Muñoz Mateo and J. Brand, New J. Phys. **17**, 125013 (2015), arXiv:1510.01465 .

[123] J. Brand and W. P. Reinhardt, J. Phys. B At. Mol. Opt. Phys. **34**, L113 (2001).

[124] J. Brand and W. P. Reinhardt, Phys. Rev. A **65**, 043612 (2002).

[125] S. Komineas and N. Papanicolaou, Phys. Rev. A **68**, 043617 (2003).

[126] T. Yefsah, A. T. Sommer, M. J. H. Ku, L. W. Cheuk, W. Ji, W. S. Bakr, and M. W. Zwierlein, Nature **499**, 426 (2013), arXiv:1302.4736 .

[127] M. J. H. Ku, W. Ji, B. Mukherjee, E. Guardado-Sanchez, L. W. Cheuk, T. Yefsah, and M. W. Zwierlein, Phys. Rev. Lett. **113**, 065301 (2014), arXiv:1402.7052 .

[128] S. Donadello, S. Serafini, M. Tylutki, L. P. Pitaevskii, F. Dalfovo, G. Lamporesi, and G. Ferrari, Phys. Rev. Lett. **113**, 065302 (2014), arXiv:1404.4237 .

[129] L. A. Toikka and J. Brand, New J. Phys. **19**, 023029 (2017), arXiv:1608.08701 .

[130] L. Chomaz, L. Corman, T. Bienaimé, R. Desbuquois, C. Weitenberg, S. Nascimbène, J. Beugnon, and J. Dalibard, Nat. Commun. **6**, 6162 (2015), arXiv:1411.3577 .

[131] W. J. Kwon, G. Del Pace, K. Xhani, L. Galantucci, A. Muzi Falconi, M. Inguscio, F. Scazza, and G. Roati, Nature **600**, 64 (2021).

[132] J. Brand, T. J. Haigh, and U. Zülicke, Phys. Rev. A **81**, 025602 (2010), arXiv:0805.4447 .

[133] L. Pitaevskii and S. Stringari, *Bose-Einstein Condensation and Superfluidity* (Oxford University Press, 2016).

[134] A. M. Kamchatnov and L. P. Pitaevskii, Phys. Rev. Lett. **100**, 160402 (2008).

[135] A. Gallemí, L. P. Pitaevskii, S. Stringari, and A. Recati, Phys. Rev. A **100**, 023607 (2019), arXiv:1906.06237 .

[136] K. Ihara and K. Kasamatsu, Phys. Rev. A **100**, 013630 (2019), arXiv:1904.02380 .

[137] A. E. Muryshev, H. B. van Linden van den Heuvell, and G. V. Shlyapnikov, Phys. Rev. A **60**, R2665 (1999).

[138] A. S. Bradley, `VortexDistributions.jl`.

[139] See Supplemental Material at http://link.aps.org/supplemental/10.1103/PhysRevA.106.043319 for animations obtained from Gross-Pitaevskii simulations that illustrate the different trajectories of Fig. 3.3 and Fig. 3.4.

[140] N. G. Parker, N. P. Proukakis, C. F. Barenghi, and C. S. Adams, Phys. Rev. Lett. **92**, 160403 (2004).

[141] A. Richaud, V. Penna, R. Mayol, and M. Guilleumas, Phys. Rev. A **101**, 013630 (2020).

[142] A. Richaud, V. Penna, and A. L. Fetter, Phys. Rev. A **103**, 023311 (2021).

[143] A. J. Leggett, *Quantum Liquids* (Oxford University Press, Oxford, 2006).

[144] X. Yu and A. S. Bradley, Phys. Rev. Lett. **119**, 185301 (2017), arXiv:1704.05410 .

[145] S. P. Johnstone, A. J. Groszek, P. T. Starkey, C. J. Billington, T. P. Simula, and K. Helmerson, Science **364**, 1267 (2019).

[146] M. A. Caracanhas, P. Massignan, and A. L. Fetter, (2021), arXiv:2110.13560 .

[147] M. R. Matthews, B. P. Anderson, P. C. Haljan, D. S. Hall, C. E. Wieman, and E. A. Cornell, Phys. Rev. Lett. **83**, 2498 (1999).

[148] M. R. Matthews, B. P. Anderson, P. C. Haljan, D. S. Hall, M. J. Holland, J. E. Williams, C. E. Wieman, and E. A. Cornell, Phys. Rev. Lett. **83**, 3358 (1999).

[149] J. T. Mäkinen, V. V. Dmitriev, J. Nissinen, J. Rysti, G. E. Volovik, A. N. Yudin, K. Zhang, and V. B. Eltsov, Nat Commun **10**, 237 (2019).

[150] W. F. Vinen, Proc. R. Soc. Lond. A **260**, 218 (1961).

[151] D. J. Thouless, P. Ao, and Q. Niu, Phys. Rev. Lett. **76**, 3758 (1996).

[152] S. Choudhury and J. Brand, "Rotational pendulum dynamics of a vortex molecule in a channel geometry," (2022), arXiv:2207.05893 [cond-mat] .

[153] B. Opanchuk, R. Polkinghorne, O. Fialko, J. Brand, and P. D. Drummond, Ann. Phys. **525**, 866 (2013), arxiv:1305.5314 .

[154] A. J. Groszek, D. M. Paganin, K. Helmerson, and T. P. Simula, Phys. Rev. A **97**, 023617 (2018), arXiv:1708.09202 .

[155] J. Skipp, J. Laurie, and S. Nazarenko, "Hamiltonian derivation of the point vortex model from the two-dimensional nonlinear Schrödinger equation," (2022), arXiv:2208.10412 .

[156] L. Amico, M. Boshier, G. Birkl, A. Minguzzi, C. Miniatura, L.-C. Kwek, D. Aghamalyan, V. Ahufinger, D. Anderson, N. Andrei, A. S. Arnold, M. Baker, T. A. Bell, T. Bland, J. P. Brantut, D. Cassettari, W. J. Chetcuti, F. Chevy, R. Citro, S. De Palo, R. Dumke, M. Edwards, R. Folman, J. Fortagh, S. A. Gardiner, B. M. Garraway, G. Gauthier, A. Günther, T. Haug, C. Hufnagel, M. Keil, P. Ireland, M. Lebrat, W. Li, L. Longchambon, J. Mompart, O. Morsch, P. Naldesi, T. W. Neely, M. Olshanii, E. Orignac, S. Pandey, A. Pérez-Obiol, H. Perrin, L. Piroli, J. Polo, A. L. Pritchard, N. P. Proukakis, C. Rylands, H. Rubinsztein-Dunlop, F. Scazza, S. Stringari, F. Tosto, A. Trombettoni, N. Victorin, W. v. Klitzing, D. Wilkowski, K. Xhani, and A. Yakimenko, AVS Quantum Science **3**, 039201 (2021).

[157] B. Seaman, M. Krämer, D. Anderson, and M. Holland, Phys. Rev. A **75**, 023615 (2007).

[158] M. Schlosser, S. Tichelmann, J. Kruse, and G. Birkl, Quantum Information Processing **10**, 907 (2011).

[159] A. Ramanathan, K. C. Wright, S. R. Muniz, M. Zelan, W. T. Hill, C. J. Lobb, K. Helmerson, W. D. Phillips, and G. K. Campbell, Phys. Rev. Lett. **106**, 130401 (2011).

[160] C. Ryu, P. W. Blackburn, A. A. Blinova, and M. G. Boshier, Phys. Rev. Lett. **111**, 205301 (2013).

[161] S. Eckel, J. G. Lee, F. Jendrzejewski, N. Murray, C. W. Clark, C. J. Lobb, W. D. Phillips, M. Edwards, and G. K. Campbell, Nature **506**, 200 (2014).

[162] C. Ryu, E. C. Samson, and M. G. Boshier, Nature Communications **11**, 3338 (2020).

[163] T. Haug, J. Tan, M. Theng, R. Dumke, L.-C. Kwek, and L. Amico, Phys. Rev. A **97**, 013633 (2018).

[164] L. Amico, A. Osterloh, and F. Cataliotti, Phys. Rev. Lett. **95**, 063201 (2005).

[165] D. Aghamalyan, N. T. Nguyen, F. Auksztol, K. S. Gan, M. M. Valado, P. C. Condylis, L.-C. Kwek, R. Dumke, and L. Amico, New Journal of Physics **18**, 075013 (2016).

[166] L. Amico, D. Anderson, M. Boshier, J.-P. Brantut, L.-C. Kwek, A. Minguzzi, and W. von Klitzing, Rev. Mod. Phys. **94**, 041001 (2022).

[167] G. Del Pace, K. Xhani, A. M. Falconi, M. Fedrizzi, N. Grani, D. H. Rajkov, M. Inguscio, F. Scazza, W. J. Kwon, and G. Roati, "Imprinting persistent currents in tunable fermionic rings," (2022).

[168] Y. Cai, D. G. Allman, P. Sabharwal, and K. C. Wright, Phys. Rev. Lett. **128**, 150401 (2022).

[169] S. Eckel, F. Jendrzejewski, A. Kumar, C. J. Lobb, and G. K. Campbell, , 5 (2014), arXiv:1406.1095 .

[170] N. Murray, M. Krygier, M. Edwards, K. C. Wright, G. K. Campbell, and C. W. Clark, Phys. Rev. A **88**, 053615 (2013).

[171] R. Kanamoto, L. Carr, and M. Ueda, Phys. Rev. Lett. **100**, 060401 (2008).

[172] R. Kanamoto, L. D. Carr, and M. Ueda, Phys. Rev. A **79**, 063616 (2009).

[173] O. Fialko, M.-C. Delattre, J. Brand, and A. Kolovsky, Phys. Rev. Lett. **108**, 250402 (2012), arXiv:1202.5083 .

[174] C. Ryu, M. F. Andersen, P. Cladé, V. Natarajan, K. Helmerson, and W. D. Phillips, Phys. Rev. Lett. **99**, 260401 (2007).